ABSTRACT

SPACE/TIME/FREQUENCY METHODS IN ADAPTIVE RADAR

by
Christopher D. Peckham

Radar systems may be processed with various space, time and frequency techniques. Advanced radar systems are required to detect targets in the presence of jamming and clutter. This work studies the application of two types of radar systems.

It is well known that targets moving along-track within a Synthetic Aperture Radar field of view are imaged as defocused objects. The SAR stripmap mode is tuned to stationary ground targets and the mismatch between the SAR processing parameters and the target motion parameters causes the energy to spill over to adjacent image pixels, thus hindering target feature extraction and reducing the probability of detection. The problem can be remedied by generating the image using a filter matched to the actual target motion parameters, effectively focusing the SAR image on the target. For a fixed rate of motion the target velocity can be estimated from the slope of the Doppler frequency characteristic. The problem is similar to the classical problem of estimating the instantaneous frequency of a linear FM signal (chirp). The Wigner-Ville distribution, the Gabor expansion, the Short-Time Fourier transform and the Continuous Wavelet Transform are compared with respect to their performance in noisy SAR data to estimate the instantaneous Doppler frequency of range compressed SAR data. It is shown that these methods exhibit sharp signal-to-noise threshold effects.

The space-time radar problem is well suited to the application of techniques that take advantage of the low-rank property of the space-time covariance matrix. It is shown that reduced-rank methods outperform full-rank space-time adaptive processing when the space-time covariance matrix is estimated from a dataset with limited support. The utility of reduced-rank methods is demonstrated by theoretical analysis, simulations and analysis of real data. It is shown that reduced-rank processing has two effects on the performance: increased statistical stability which tends to improve performance, and introduction of a bias which lowers the signal-to-noise ratio. A method for evaluating the theoretical conditioned SNR for fixed reduced-rank transforms is also presented.

SPACE/TIME/FREQUENCY METHODS IN ADAPTIVE RADAR

by
Christopher D. Peckham

A Dissertation
Submitted to the Faculty of
New Jersey Institute of Technology
in Partial Fulfillment of the Requirements for the Degree of
Doctor of Philosophy

Department of Electrical and Computer Engineering

January 2000

APPROVAL PAGE

Space/Time/Frequency Methods in Adaptive Radar

Christopher D. Peckham

Dr. Alexander M. Haimovich, Dissertation Advisor — Date
Associate Professor of Electrical Engineering, NJIT

Dr. Yeheskel Bar-Ness, Committee Member — Date
Distinguished Professor of Electrical Engineering
and Director of Center for Communications and Signal Processing, NJIT

Dr. Joseph Frank, Committee Member — Date
Associate Professor of Electrical Engineering, NJIT

Dr. Hongya Ge, Committee Member — Date
Assistant Professor of Electrical and Computer Engineering, NJIT

Dr. Kenneth Abend, Committee Member — Date
Director, Advanced Signal Processing Laboratory, GORCA Technologies, Inc.

BIOGRAPHICAL SKETCH

Author: Christopher D. Peckham

Degree: Doctor of Philosophy in Electrical Engineering

Undergraduate and Graduate Education:

- Doctor of Philosophy in Electrical Engineering,
  New Jersey Institute of Technology, Newark, NJ, 2000
- Master of Science in Electrical Engineering,
  New Jersey Institute of Technology, Newark, NJ, 1988
- Bachelor of Science in Electrical Engineering,
  New Jersey Institute of Technology, Newark, NJ, 1987

Major: Electrical Engineering

Presentations and Publications:

A.M. Haimovich, C. Peckham, T. Ayoub, J.S. Goldstein, and I.S. Reed, "Reduced-Rank STAP Performance Analysis", Accepted for publication in *IEEE Transactions of AES*, April 2000.

A.M. Haimovich, C. Peckham, T. Ayoub, J.S. Goldstein, and I.S. Reed, "Performance Analysis of Reduced-Rank STAP", *1997 National Radar Conference.*

A. Haimovich, C. Peckham, and J. Teti, "SAR Imagery of Moving Targets - Application of Time-Frequency Distributions for Estimating Motion Parameters", *SPIE's International Symposium on Optical Engineering in Aerospace Sensing*, Orlando, FL, USA, April 4-8, 1994, SPIE Proceedings Volume 2238, pp. 238-247.

Y. Bar-Ness and C. Peckham, "Word based data compression schemes", *Proceedings of the IEEE International Symposium on Circuits and Systems*, Portland, OR, USA, May 8-11 1989 v 1, (1989), p 300-303.

To Allison, Conor and Ceara

ACKNOWLEDGMENT

I would like to begin by thanking my advisor, Professor Alex Haimovich, for his assistance and support throughout this process. He pushed me when it was needed and made me do what was necessary to move the process forward. I throughly enjoyed the time we had together during my studies and learned a great deal from him on many subjects along the way.

I would also like to thank my committee members for their assistance with this work. Dr. Bar-Ness offered his support and questions. He made a difference to me during my undergraduate studies and helped again during this process. I appreciate Dr. Joseph Frank serving on the committee. He was always able to bring something new to a subject during my graduate studies and brought some good questions to the table related to this work. Rounding out the committee, I would like to thank Dr. Hongya Ge and Dr. Kenneth Abend for their professionalism and support. Each of them offered comments that improved the work as well as being patient with me during the finish.

There were many students that were with me at the Center for Communication and Signal Processing Research over the years. Out of them all, I would like to thank Tareq Ayoub for his assistance with my work and being there when I needed someone to bounce ideas around with.

I would also like to recognize the following people: John Andrews for being himself, Louise Newton Heimbach for always keeping the dream, Brian White for listening to me and giving advice when he could, and Alice Ziemba for showing me what I could do many years ago.

Finally, I would like to thank my wife, Allison. She put up with more than others may have tolerated. To her, I would like to say, "Thank you for helping me fulfill this dream".

TABLE OF CONTENTS

Chapter Page

LIST OF FIGURES

Figure **Page**

CHAPTER 1

INTRODUCTION

Various space, time, and frequency techniques may be used to process signals originating from radar systems. These techniques are utilized in advanced radar systems that are capable of detecting targets in environments containing jamming and clutter. Clutter and jamming affect radar systems in various ways. Ground clutter observed by an airborne platform may be extended in both angle and range. Platform motion causes the ground clutter to be spread in Doppler frequency. Jamming signals are localized in angle and spread over all Doppler frequency. To perform interference cancellation, multidimensional filtering over the spatial and temporal domains is required. Uncertain knowledge of the clutter and jamming environment requires the use of systems that perform data-adaptive processing.

Time-frequency distributions are mappings of information contained in a time series into functions of time and frequency. TFDs have been proven to be powerful tools for signal analysis and processing. In Synthetic Aperture Radar (SAR) systems, the SAR returns may be processed with different time-frequency distributions to analyze specific characteristics of targets within the radar return. The doppler frequency in SAR is not a fixed quantity but it is linear in time. TFDs may be used where localization of this information is needed. SAR systems may be used in applications requiring high resolution imaging.

Space-time adaptive processing (STAP) refers to the simultaneous processing of the spatial samples from an array antenna and the temporal samples provided by the echos from multiple pulses of a radar coherent processing interval (CPI). In STAP, signals are varying in space and doppler but the doppler is fixed over the processing interval. In the case of STAP, reduced rank techniques may be applied that take advantage of the low-rank property of the space-time covariance matrix. STAP is applicable for target tracking and detection.

1.1 SAR Processing using Time-frequency Distributions

Synthetic Aperture Radar (SAR) systems operating in stripmap mode are designed to produce two-dimensional, high resolution images of the earth's surface. This high resolution is obtained by utilizing the relative motion between the radar and the observed scene. The knowledge of the platform motion allows the synthesis of a long antenna, along the flight direction, and the resulting high spatial resolution. The echoes corresponding to successive transmitted pulses exhibit a phase shift varying with the time as a function of the relative motion between the radar and each backscattering element. Due to the motion of the radar platform, each point on the ground reflects an echo having a Doppler shift proportional to the radar velocity vector along the line of sight. Points at different distances are separated in time, by transmitting a chirp signal and then applying a range compression. Points at the same distance, but observed from different angles, exhibit different Doppler shifts.

Targets moving along-track (in parallel with the SAR platform) appear as a defocused object superimposed on the ground map. The defocused image is caused by the mismatch between the SAR processing parameters and the signals returned from the moving target. To achieve high resolution in the azimuth dimension, the SAR collects and integrates samples of signals received from the same range. For a fixed rate of relative motion, and for a target at a specified range and azimuth location, the phase of the SAR return is a quadratic function of time. The phase rate of change (the Doppler frequency) is then a linear function of time, and the Doppler rate is constant. SAR processing is tuned to the Doppler rate calculated for geostationary imaging. The blurring of a moving target can then be corrected by carrying out the SAR processing using the actual Doppler rate associated with the target. In this work we study a number of techniques for extracting the target motion parameters from the SAR data. Those parameters may then be subsequently used to adjust the processing to focus on the moving object.

The signal received from a target moving over a stationary background can be modeled as samples of a chirp signal embedded in noise. Therefore the problem of estimating the motion parameters is equivalent to the estimation of a chirp signal in a noisy environment. Time-frequency Distributions (TFD) are mappings of information contained in a time series into functions of time and frequency. TFD's have been proven powerful tools for analyzing signals with time varying properties [1] [2]. In particular, TFD's can be applied to the estimation of the parameters of the linear FM signal (chirp). Various authors have used TFD for estimating the instantaneous-frequency (IF) of a signal in noisy environments.

Boashash et. al. compare the performance of a number of algorithms used to determine the IF [3]. White estimated the IF of a noisy signal using TFD techniques [4]. Lovell compares the performance of TFD's in the Cohen's class with other IF estimation techniques such as the zero crossing estimator and an estimator based on linear regression in the signal phase [5]. Boashash showed [6] that the Cross Wigner-Ville distribution (XWVD) method provides the best performance in terms of the SNR threshold which meets the Cramér-Rao bound. Harris and Salem compared the Wigner-Ville distribution (WVD) to various FM discriminators [7]. The Wigner-Ville distribution has also been applied to the analysis of SAR data for the purpose of extracting the motion parameters of a moving target [8, 9, 10]. The Short-Time Fourier transform (STFT) and the Gabor expansion are of special interest being linear and thus not exhibiting cross-terms when multiple time-varying signals are analyzed. Auslander et. al. compared the performance of the Gabor expansion and Short-Time Fourier transform in the presence of noise [11]. Morlet's wavelet [12, 13] is based on a Gaussian and is an extension of Gabor's basic idea for a more efficient representation of seismic data [13]. This wavelet has also been used to process SAR signals [14].

1.2 Space-time Adaptive Processing

Space-time adaptive processing (STAP) radar performance has been for some time a topic of considerable interest to the radar community. The need for adaptive methods arises in practice when statistical properties of the interference are not known and need to be inferred from the observed data. STAP is a system that linearly combines the spatial samples from the elements of an antenna array and the temporal samples that are provided by the successive pulses of a multiple-pulse waveform. An array beamformer and target Doppler filter are combined to create a STAP weight vector. In the ideal case, STAP provides a coherent gain on target while suppressing clutter and jamming by forming angle and Doppler response nulls. The weight vector is dynamically determined based on the data received by the system. Since a weight vector is optimized for a specific angle and Doppler, STAP systems may compute multiple weight vectors to cover the target angles and Doppler frequencies of interest.

A primary difficulty in STAP is the dimension of the adaptive weight vector that can become large. As this dimension becomes larger, the required sample support for STAP detection also needs to increase. In optimum filter theory, the interference covariance is assumed known. This is not directly applicable to practical problems, but it is the start from which adaptive filtering theory is developed. The optimal Neyman-Pearson detector for a known signal vector in colored Gaussian noise with a known covariance matrix is linear, i.e., it is constructed from a linear combination of the inputs to the space-time array. In practice, the interference+noise covariance matrix is typically not known. A well-known solution to that is the sample matrix inversion (SMI) method, that substitutes an estimate for the true noise covariance matrix expression in the linear detector [15]. It is also well-known that if the sample support consists of a population of independent, identically distributed vectors with a multivariate Gaussian distribution, the number of samples required to achieve performance within 3 dB of the optimal, is approximately $K \approx 2N$, where N is the dimension of the vectors. The main drawback of the SMI detector is that its sample support K is proportional to the array degrees of freedom N. Recent publications have shown the advantages of various forms of reduced-rank processing over the full-rank SMI [16, 17, 18].

A taxonomy of reduced-rank methods is shown in Figure 1.1. Two main architectures are noted: the reduced-rank minimum variance beamformer (RR-MVB), and the reduced-rank generalized sidelobe canceler (RR-GSC). A third method, loaded SMI (indicated by a dashed line), refers to adding a constant term to the diagonal of the covariance matrix to improve its numerical conditioning. LSMI behaves as a reduced-rank method [19, 20]. The RR-MVB architecture is shown in Figure 1.2. Given a rank reducing transformation $\mathbf{T}$, adaptation can take place in the subspace spanned by the principal components of the transform (interference subspace methods) [18], or in the complementary subspace (noise subspace methods) [16, 17]. The transforms are either fixed (such as discrete Fourier transform - DFT, or discrete cosine transform - DCT) or data dependent (Karhunen-Loeve transform - KLT). The RR-GSC architecture is shown in Figure 1.3. The rank-reducing transformation is applied in the branch used for estimating the interference component. Another class of RR-GSC methods are based on the cross-spectral metric (CSM) [21, 22].

It is interesting to note that reduced-rank methods are generally evaluated according to the error they produce with respect to full-rank adaptive processing. When the true covariance matrix is known, reduced-rank processing is suboptimal. However, our interest in those methods stems from the fact that in limited dataset regimens reduced-rank methods actually *outperform* full-rank adaptive

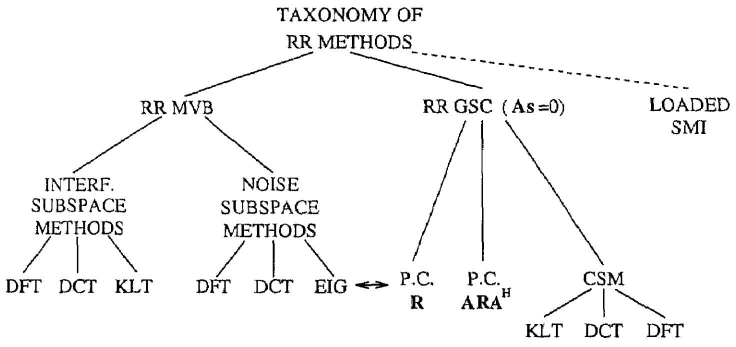

Figure 1.1 A taxonomy of reduced-rank methods

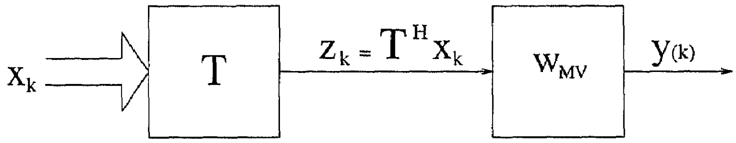

Figure 1.2 Reduced-rank MVB

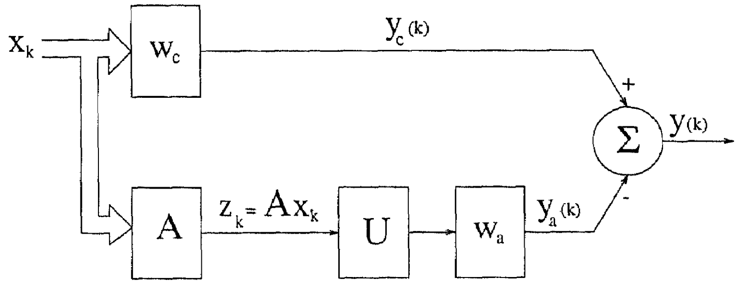

Figure 1.3 Reduced-rank GSC

processing. This is explained by the presence, in addition to thermal noise effects, of errors resulting from the estimation process. Reduced-rank processing suppresses estimation errors at the cost of a bias in the SNR. The net effect, however, is a significant performance improvement for cases when the interference may be modeled as low-rank. Reduced-rank methods are clearly important for STAP radar, where a large number of degrees of freedom may be available. For a uniform array and for fixed PRF, the space-time clutter covariance matrix is essentially low-rank due to the inherent oversampling nature of the STAP architecture. Hence, the space-time radar problem is well suited to the application of techniques that take advantage of the low-rank property.

This work is organized as follows: Chapter 2 introduces time-frequency analysis, including the Fourier transform, the short-time Fourier transform, the Gabor expansion, the Wigner-Ville transform, and the Continuous Wavelet transform. These time-frequency analysis techniques are then applied to the problem of estimating SAR target parameters. The space-time adaptive processing signal environment is introduced in Chapter 3. Reduced rank processing of STAP systems is presented in Chapter 4 with numerical results of simulated and real data presented and compared in Chapter 5. Finally, conclusions are presented in Chapter 6.

CHAPTER 2

TIME-FREQUENCY TECHNIQUES USED TO ESTIMATE SAR TARGET PARAMETERS

Signals may be characterized over a time-frequency plane by the use of time-frequency signal representations. The temporal localization of a signal's spectral components may be found through the time-frequency signal representations combination of time-domain and frequency-domain analyses.

A signal received in a SAR system from a target moving over a stationary background may be modeled as samples of a chirp signal embedded in noise. The problem of estimating the motion parameters of this moving target is equivalent to the estimation of a chirp signal in a noisy environment. Time-frequency distributions are mappings of information contained in a time series into functions of time and frequency and have been proven as useful tools for analyzing signals with time-varying properties. TFDs can be applied to the estimation of the parameters of a linear FM signal and therefore applied to the previously mentioned problem of estimating motion parameter estimation.

In this chapter, synthetic aperture radar and the time-frequency signal representations that are used in the analysis are introduced. Several introductory papers on time-frequency analysis are available for reference including Cohen [1], Hlawatcsh and Boudreaux-Bartels [23], and Boashash [24]. This chapter also contains the application of four specific TF analysis techniques: the Short-Time Fourier transform, the Gabor expansion, the Continuous Wavelet transform and the Wigner-Ville distribution, to the estimation of the relative along-track velocity between the SAR platform and a moving target.

2.1 An Overview of Synthetic Aperture Radar

Synthetic aperture radar (SAR) is an airborne/spaceborne radar mapping technique that generates high resolution maps of surface terrain and target areas. The first demonstration of SAR mapping was performed in 1953 by a group from the University of Illinois when they mapped a section of Key West, Florida. A few of the many overview references on the subject of SAR are Brown [25], Kirk [26], and Munson [27]. Fine azimuth resolution may be obtained by using a small radar antenna, storing returns received over time, and integrating the returns so as to synthesize the equivalent of a long antenna array. SAR may be used to obtain fine resolution in both the slant and cross ranges. Slant range refers to the range in the radar's line of sight. Resolution in this range is typically obtained by coding the transmitted pulse with an FM chirp. Cross range is the resolution transverse to the radar's line of sight and resolution in this range is obtained by coherently integrating echo energy reflected from the area illuminated by the radar. Synthetic aperture refers to the distance that the radar travels during the time that reflectivity data is collected from a point to be resolved which remains illuminated by the radar beam. The length of the synthetic aperture of a side-looking SAR is the ground-track distance over which coherent integration occurs. In SAR, ideal processing produces constant cross-range resolution verses range. A side-looking SAR configuration is shown in Figure 2.1.

Echo energy from each range-resolved scatterer in the mapping area is made to arrive in phase at the output of the radar processor to produce the narrow beamwidth associated with the synthetically generated long aperture. This is achieved by correcting for all moving of the radar platform that deviates from straight line motion. Focused SAR, instead of unfocused SAR, has the quadratic phase error of the radar return corrected after the signal integration.

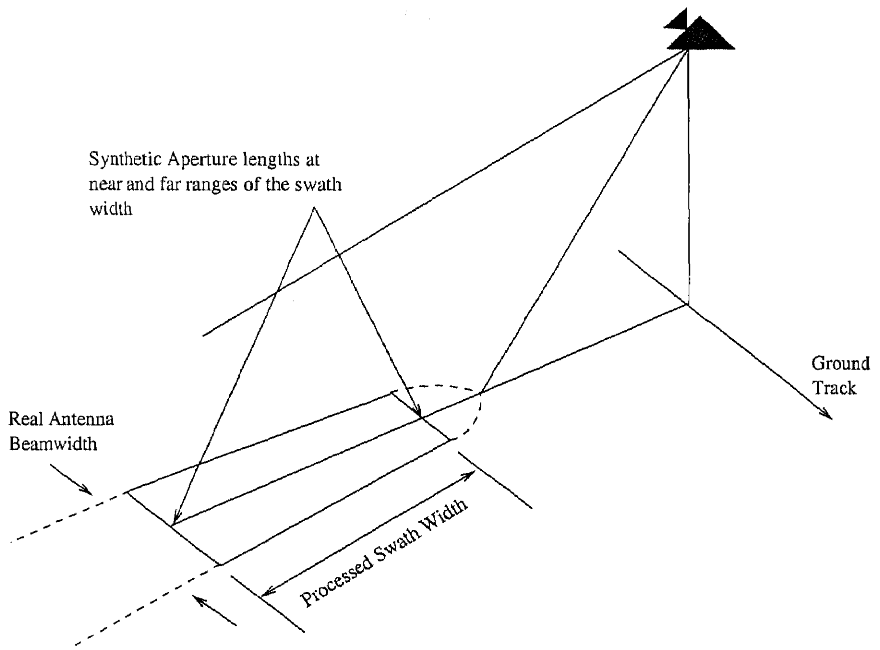

Figure 2.1 Side-Looking SAR

Fundamental characteristics of side-looking SAR may be explained in terms of equirange and equi-Doppler lines on the earth's surface to be mapped by the moving radar platform. Equirange lines on the earth's surface are the intersections with the earth's surface of successive concentric spheres centers at the radar where points on these spheres are equidistant from the radar. Equi-Doppler lines on the earth's surface are produced by intersections with the earth's surface of coaxial cones, that are concentric about the radar's flight line as the axis and the radar position as the apex of the cones. Points on the cones appear at constant velocity relative to the radar.

The radar is able to view the portion of the range-Doppler coordinate system which is illuminated by the real antenna beam. The echo power distribution as a function of range delay and Doppler is the SAR image for that area.

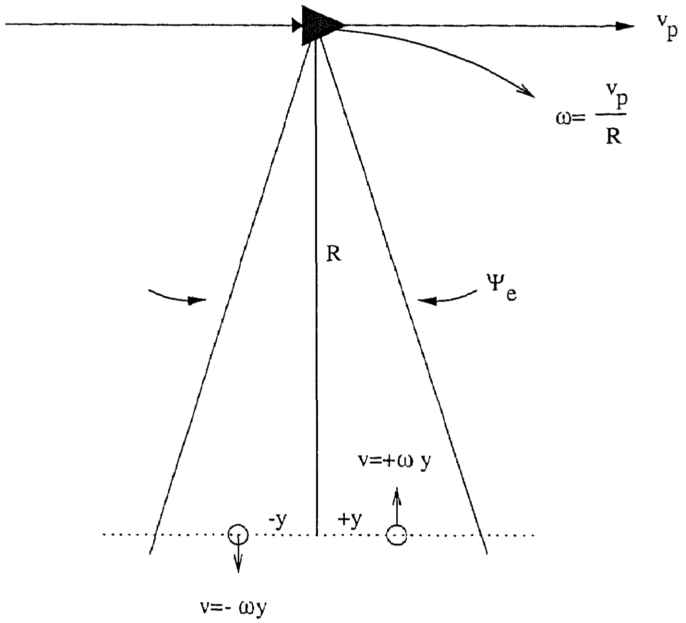

Figure 2.2 SAR cross-range Doppler

2.2 Doppler

To explain the SAR concept from the point of view of differential Doppler signals, the signals produced by scatters separated in cross range relative to the radar are examined as shown in Figure 2.2 at the instant the platform is directly beamed on boresite to the center of two point targets. These targets are both at range R which is located in cross range $-y$ and $+y$ from the radar. The instantaneous velocity of the radar past the two targets, for small real beams, will produce an echo signal containing a pair of instantaneous Doppler offset frequencies $-(2f/c)\omega y$ and $+(2f/c)\omega y$. This is for a radar center frequency f, with ω being the instantaneous angular velocity of the aircraft relative to the centroid of the two targets.

The cross-range resolution, with a uniform gain over an angle region of the real beam[28], is

$$\begin{aligned}\Delta r_c &= \frac{c}{2\omega T f} \\ &= \frac{1}{2}\frac{\lambda}{\omega T}. \end{aligned} \tag{2.1}$$

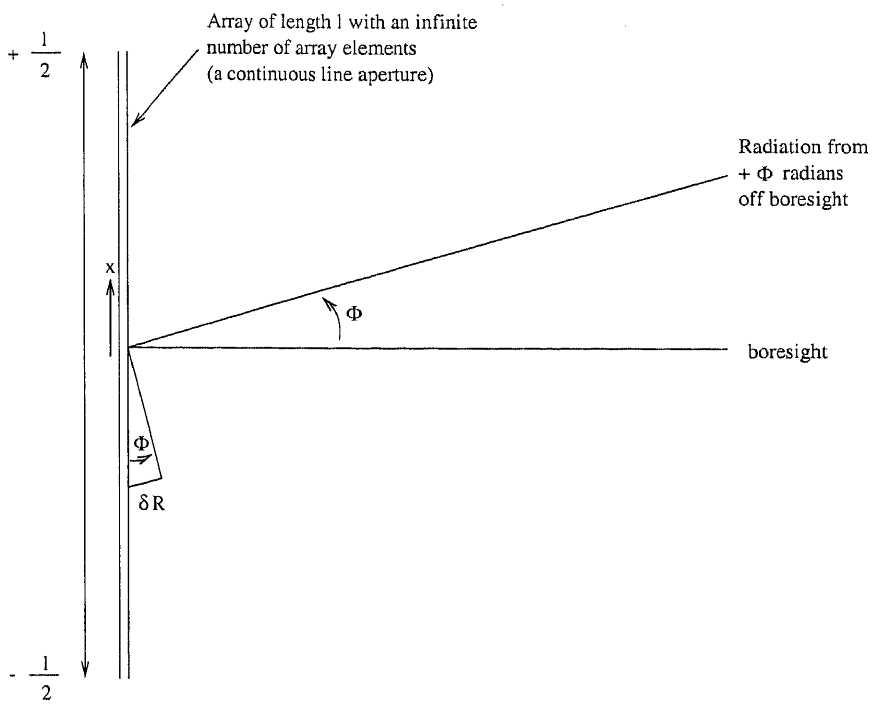

Figure 2.3 Real Aperture Line Antenna

For coherent integration over a beamsegment Ψ of constant gain,

$$\Delta r_c = \frac{1}{2}\frac{\lambda}{\Psi}. \tag{2.2}$$

Resolution is of interest for total beam integration of a uniformly weighted antenna. For total beam integration during the beam dwell time of a real antenna with an equivalent rectangular beamwidth Ψ_e, $\omega T = \Psi_e$.

A line antenna of length l is shown in Figure 2.3. This line represents an antenna that continuously integrates incident radiated energy as if it were an infinite number of array elements spaced infinitesimally close to another. Radiation from the boresight direction to the line antenna will arrive at the same time, if the source is from an infinite range. This will be taken as zero phase. For radiation from off-boresight angles, the arrival phase is a function of the distance along the antenna.

Through the expression for the one-way antenna response, it can be shown that the expression for the equivalent rectangular beamwidth becomes $\Psi_e = \lambda/l$ which results in the expression for the cross-range resolution reducing to

$$\Delta r_c = \frac{1}{2}\frac{\lambda}{\Psi_e} = \frac{l}{2}. \tag{2.3}$$

The resolution provided by the total beam integration for a uniformly weighted antenna is the same as that provided by integration over the antenna's equivalent rectangular beamwidth.

The expression for cross-range SAR resolution is based on the response produced by coherent integration during the real beam dwell time of the reflected signals from point targets. Coherent integration of the signal received along the resulting synthetic aperture produce the fine cross-range resolution associated with a large aperture. From the Doppler standpoint, coherent integration of the Doppler shifted signal from each of the pair of point targets seen by the SAR produced fine Doppler resolution which is directly related to cross-range resolution. Azimuth compression is achieved by performing coherent integration. This may be done by correlating the azimuthal signal data collected along known range verses azimuth trajectories to a suitable azimuthal reference.

2.2.1 Data Collection

As the SAR platform using chirp-pulse compression travels above and alongside of the area to be mapped, chirp pulses are transmitted at some pulse repetition frequency (PRF). The process of collecting SAR data obtained from a chirp-pulse compress radar is shown in Figure 2.4(a). The time interval between pulses is made sufficiently long to prevent ambiguous range responses over the effective illuminated range. A slightly different area is illuminated by each transmitted pulse. Each time a pulse is transmitted, the echo signal is sampled at some range sample spacing over some portion of the illuminated range extent and referred to as range swath.

The collected data comprise a set of reflectivity measurements in two dimensions. The dimensions of the data format is referred to as slant range and cross range. A data record will extend in slant range over the range swath and continuously in cross range along the flight path over which the data are collected as shown in Figure 2.4(b). Before processing, the data set does not resemble a map or image and echos from individual point targets are dispersed in both range and azimuth. Data collected from the slant-range and cross-range space are processed to achieve range and azimuth compression.

2.3 Why are Time-frequency Representations Needed ?

A one-to-one relation exists between a signal in the time domain, $s(t)$, and the spectrum in the frequency domain, $S(f)$. This relation is shown using the Fourier transform. For a one-dimensional signal, $s(t)$, the Fourier transform is given by

$$S(f) = \mathcal{F}\left[s\right](\omega) = \int_{-\infty}^{\infty} s(t)e^{-j2\pi ft}dt. \tag{2.4}$$

The inverse Fourier transform is

$$s(t) = \mathcal{F}^{-1}\left[S\right](t) = \int_{-\infty}^{\infty} S(f)e^{j2\pi ft}df. \tag{2.5}$$

The Fourier transform of $s(t) = sin(2\pi ft)$ is shown in Figure 2.5.

While the Fourier transform allows a signal to be transformed back and forth between the time and frequency domains, it does not allow for a combination of the two domains. The time localization of the spectral components is contained in the phase of the spectrum but it may not be easy to interpret.

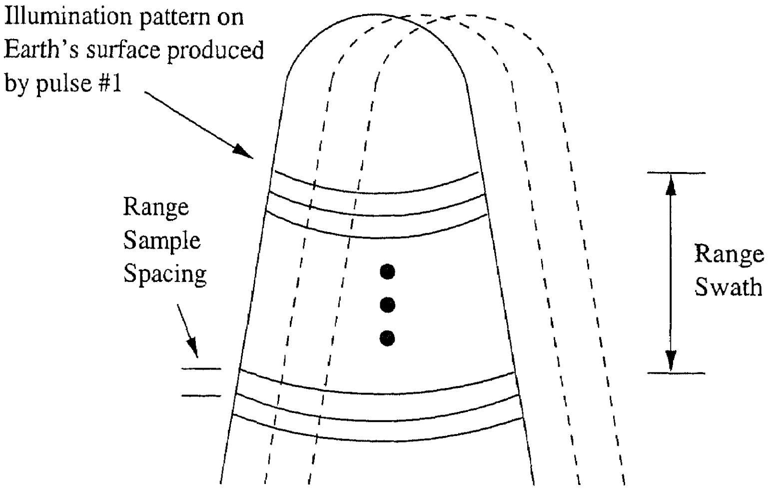

(a) SAR data collection

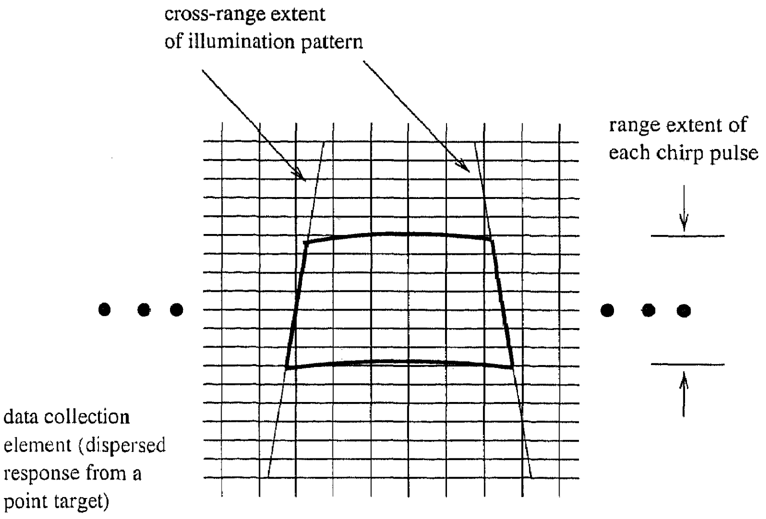

(b) SAR data record

Figure 2.4 SAR data collection

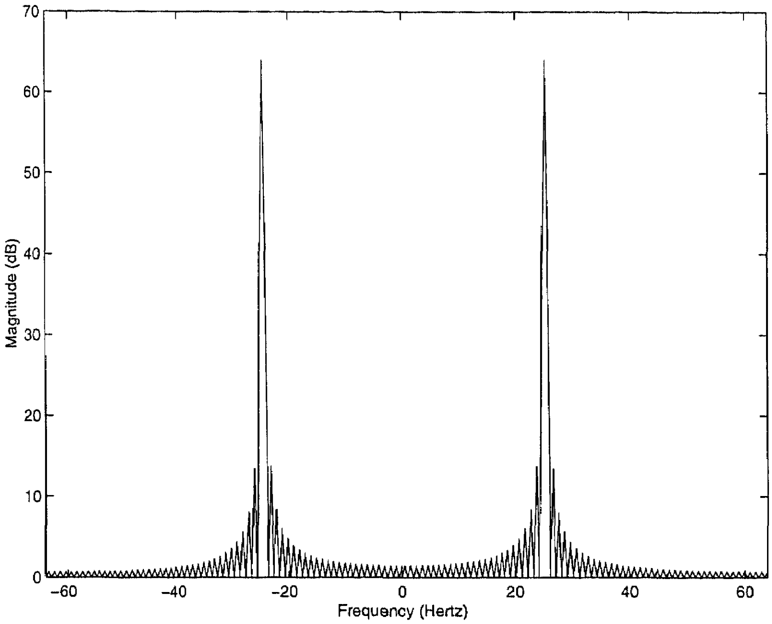

Figure 2.5 Magnitude of the Fourier transform of a sine wave with a frequency of 20 Hz

A complex-valued frequency-shift-keyed signal, as in Figure 2.6, is an example of a signal which displays time localization of spectral components. This figure shows only a single frequency is present at any instance of time. This frequency may be obtained as the derivative of the instantaneous phase, $arg\{s(t)\}$, which is defined as the instantaneous frequency (IF) [29],

$$f_s(t) \triangleq \frac{1}{2\pi}\frac{d}{dt}arg\{s(t)\}. \tag{2.6}$$

The group delay (GD) is defined as

$$t_s(f) \triangleq -\frac{1}{2\pi}\frac{d}{df}arg\{S(f)\} \tag{2.7}$$

where $arg\{S(f)\}$ is the phase spectrum.

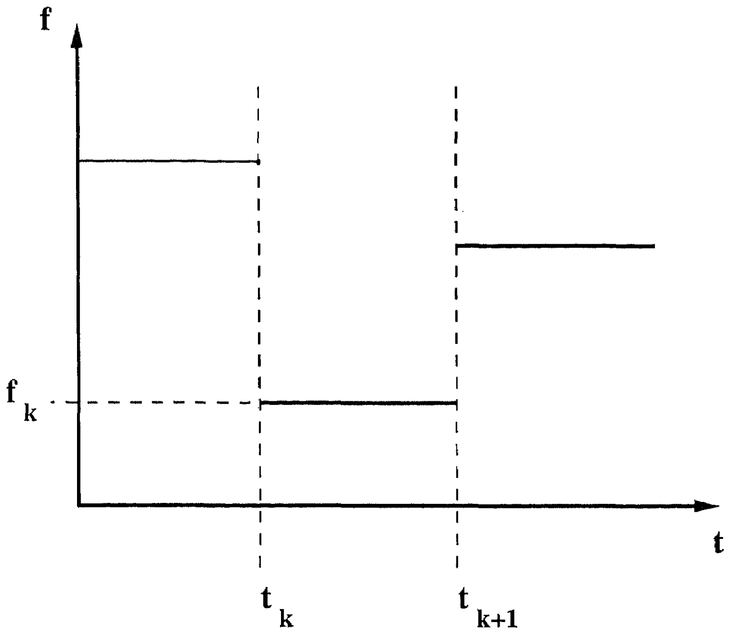

Figure 2.6 Time-frequency description of a frequency-shift keyed signal, $x(t) = e^{j2\pi f_k t}, t_k < t < t_{k+1}$. Within each time interval $[t_k, t_{k+1}]$, only a single frequency f_k is present

The time localization of the spectral components are described by the instantaneous frequency and the group delay for a group of signals. The instantaneous frequency represents the frequency as a function of time, $f = f_s(t)$ and assumes there exists a single frequency component at each time t. This assumption does not apply in the case of the signal $s(t) = e^{j2\pi f_1 t} + e^{j2\pi f_2 t}$, containing two frequency components (f_1 and f_2) at all times. For the group delay, the assumption is that a given frequency is concentrated around a single instance of time.

If the signal can be described by a *surface* spanning the time-frequency plane instead of a curve on this plane, the restrictions associated with the instantaneous frequency and the group delay can be minimized. This concept of a surface spanning the plane corresponds to a joint function $T_s(t, f)$ of time and frequency and is know as the time-frequency representation of the signal.

2.3.1 Short-Time Fourier Transform

The short-time Fourier transform (STFT) has played a large role in the history of digital signal processing [30, 31, 32]. It is defined as

$$\mathcal{S}(t,f) = \int_{-\infty}^{\infty} s(\tau) g^*(\tau - t) e^{-\jmath 2\pi f \tau} d\tau, \tag{2.8}$$

where $s(t)$ is the signal being analyzed and $g(t)$ is a time-shifted windowing function. The squared magnitude of the STFT is known as the spectrogram. A simple interpretation of the STFT is a "sliding-window Fourier transform". The analysis of the frequency content of s at time t_0 may be found by sliding the window function, $g(t)$, across the signal until it is centered at t_0 and then taking the Fourier transform of the signal-window product. Each constant-time slice, $\mathcal{S}(t,f)$, of the STFT represents the frequency content of the signal around time t_0. Many functions have been used successfully as STFT windowing functions: Gaussian, Hamming, Hanning, and square/rectangular functions. The computation of the time slice at time t_0 is shown in Figure 2.7. The spectrogram of $s(t) = sin(2\pi f t)$ using a hamming window is shown in Figure 2.8.

The STFT can also be expressed in the terms of the Fourier transform of the signal and windowing functions in the form

$$\mathcal{S}(t,f) = e^{-\jmath 2\pi f t} \int_{-\infty}^{\infty} S(\Omega) G^*(f - \Omega) e^{\jmath 2\pi \Omega t} d\Omega. \tag{2.9}$$

The STFT of the multicomponent signal

$$s(t) = \sum_{i=1}^{3} e^{-\alpha(t-T_i)^2 + \jmath 2\pi f_i t} \tag{2.10}$$

computed using a hamming window is shown in Figure 2.9. As is shown, the three signal components are centered at the points (T_1, f_1), (T_2, f_2), and (T_3, f_3).

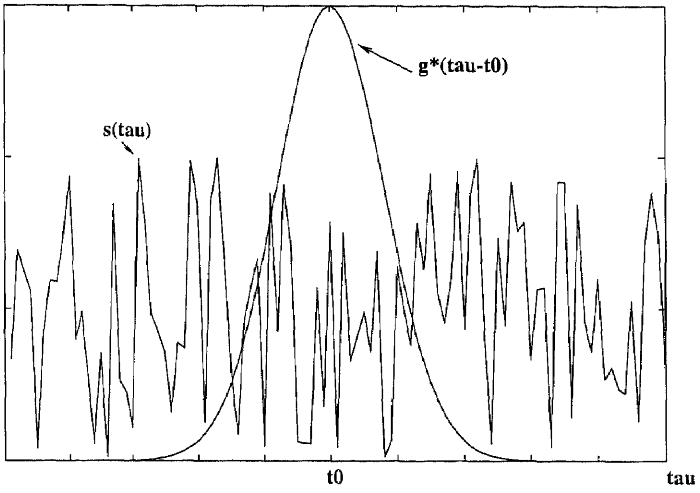

Figure 2.7 Computation of the short-time Fourier transform (STFT). To estimate the frequency content of the signal s around time t_0, the low-pass window g is centered at t_0 and the Fourier transform of $s(\tau)g^*(\tau - t_0)$ is calculated

2.3.1.1 Time-frequency Resolution: The performance of the STFT is affected by the choice of the window and the signal concentration. The fundamental tradeoff between time and frequency resolution may be understood by reviewing Equations 2.8 and 2.9.

Each constant-time slice of the STFT indicates the frequency content of the portion of the signal that lies within the window function at the selected time. A narrow window g may be used to increase the time resolution of the STFT. However, as g narrows in time, the corresponding frequency window G widens, reducing the frequency resolution. This demonstrates that it is impossible to have 'perfect' time and frequency resolution simultaneously and is referred to as the time-frequency uncertainty principle[33].

This principle also illustrates that it may be useful to use different windowing functions for different applications. Narrow time windows are typically used when

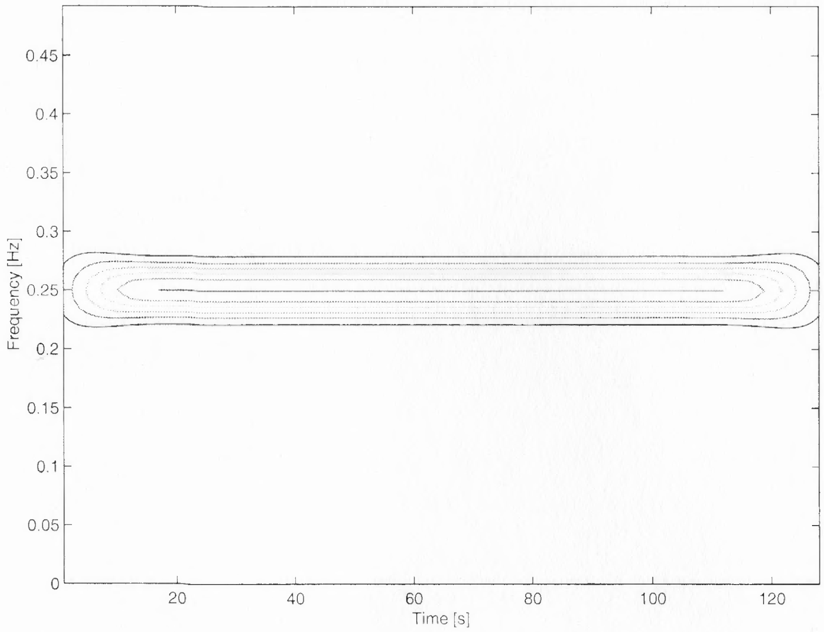

(a) Contour plot

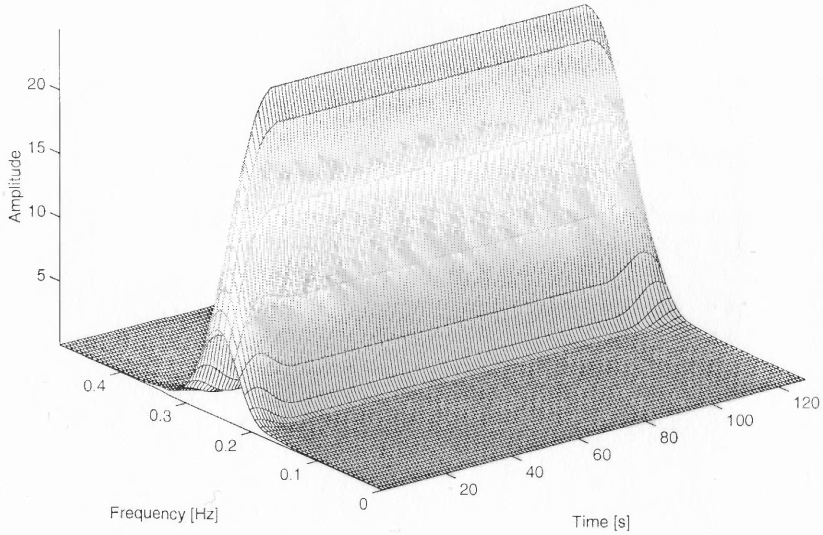

(b) Mesh plot

Figure 2.8 STFT of a sine wave

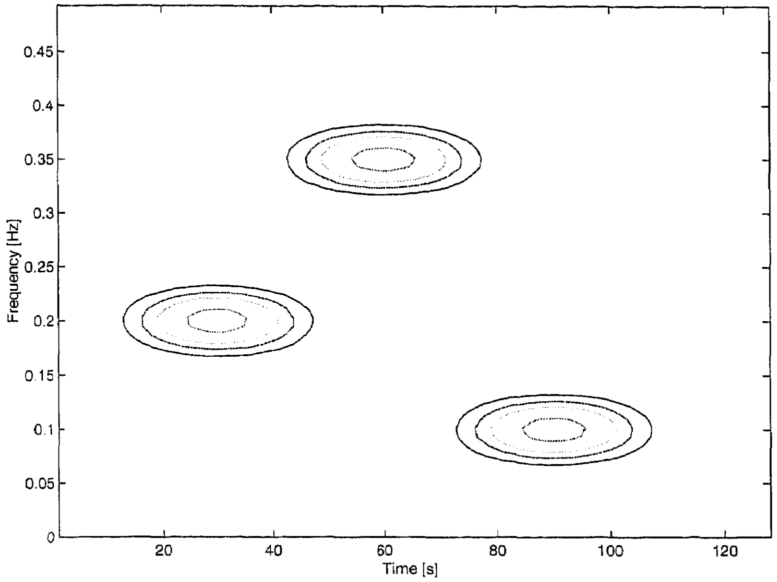

Figure 2.9 Spectrogram of a multicomponent signal (Equation 2.10) using a hamming window

the time signal is changing rapidly. Conversely, when the signal is more slowly varying and accurate frequency content estimates are required, wide windows may be employed.

The effect of window length on the performance of the STFT is shown in Figure 2.10. The signal in Equation 2.10 is analyzed as in Figure 2.9 but with a narrower window in Figure 2.10a and a wider window in Figure 2.10c.

The Short-Time Fourier transform of the analytic function $z(t)$ is defined [34]:

$$S_z(t,f) = \int z(\tau)h^*(t-\tau)\exp^{-\jmath 2\pi f t}\, d\tau \tag{2.11}$$

Gabor defined the analytic signal as a means of obtaining a unique complex signal from a real-valued signal, $s(t)$. The analytic signal is defined as [33],

$$z(t) = s(t) + \jmath\mathcal{H}\left[s(t)\right], \tag{2.12}$$

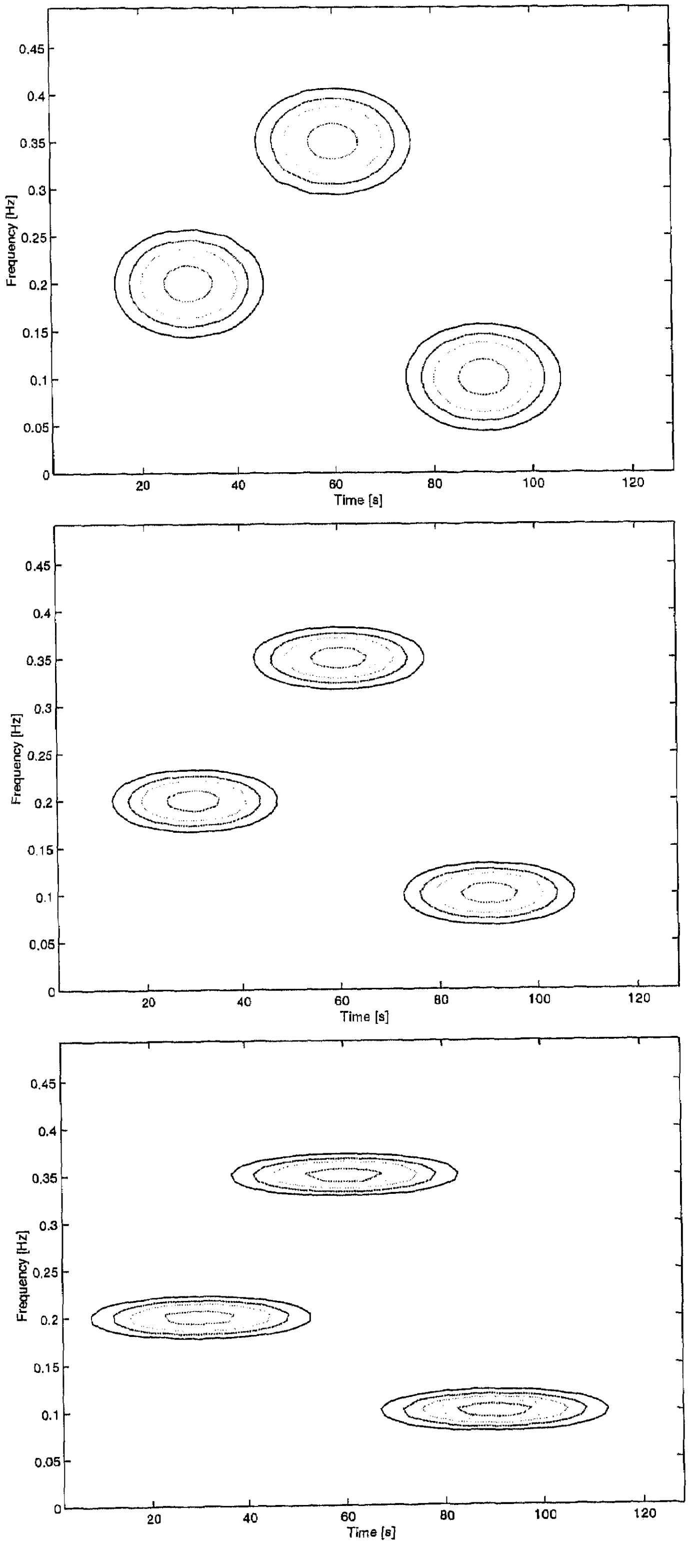

Figure 2.10 Tradeoffs of various STFT windows

where $\mathcal{H}$ is the Hilbert transform. For signal analysis, it is convenient to work with a complex signal. When a complex signal is needed when only a real signal is available, the analytic signal may be used.

2.3.1.2 Discrete Form of the STFT: For practical application of the STFT, a discrete form of Equation 2.8 is needed. Samples of the STFT at equidistant time-frequency grid points (nT, kF) where $T > 0$ and $F > 0$ are the sampling periods for the time and frequency variables are taken, resulting in

$$\mathcal{S}(nT, kF) = \int_{-\infty}^{\infty} s(\tau) g^*(\tau - nT) e^{-jk2\pi F\tau} d\tau. \tag{2.13}$$

The time function in Equation 2.13, $s(t)$, may also be sampled. The discrete version of the STFT is then,

$$\mathcal{S}(nT, kF) = \sum_{m} s(m) g^*(mT - nT) e^{-jk2\pi Fm/M}, \tag{2.14}$$

where $g(m)$ is a sampled window function of finite length M.

2.3.2 Gabor Expansion

The signal $s(t)$ may also be represented as a superposition of time-frequency-shifted versions of an elementary signal $\gamma(t)$,

$$s(t) = \int_{-\infty}^{\infty} \int_{-\infty}^{\infty} T_x(t', f') \left[\gamma(t - t') e^{j2\pi f' t}\right] dt' df'. \tag{2.15}$$

In this form, $s(t)$ has been expanded into the basis functions $\gamma_{t', f'} = \gamma(t - t') e^{j2\pi f' t}$. When $\gamma(t)$ is centered around $t = 0$ and $f = 0$, the basis signal is centered around the time-frequency point (t', f'). Therefore, the function $T_x(t', f')$ in Equation 2.15 will show how the 'neighborhood' around the time-frequency point (t', f') contributes to $s(t)$. The coefficient function $T_x(t', f')$ may be chosen as the STFT,

$$T_x(t', f') = \mathcal{S}(t, f) = \int_{-\infty}^{\infty} s(\tau) g^*(\tau - t) e^{-j2\pi f\tau} d\tau, \tag{2.16}$$

provided that the window $g^*(t)$ satisfies $\int \gamma(t) g^*(t) dt = 1$.

$s(t)$ may be represented as a combination of Equation 2.16 and Equation 2.15,

$$s(t) = \int_{t'} \int_{\omega'} S(t', f')\gamma(t - t')e^{j2\pi f' t} dt' df'. \tag{2.17}$$

This equation may be viewed as an expansion of $s(t)$ into time-frequency shifted versions $g_{mn}(t)$ of an elementary function $g(t)$,

$$s(t) = \sum_m \sum_n c_{mn} \tilde{g}(t - mT)e^{2jnFt} \tag{2.18}$$

where $\tilde{g}(t)$ is the dual frame generating function [12]. The coefficients c_{mn} are given by

$$c_{mn} = \frac{1}{\pi^{1/4}} \int_{-\infty}^{\infty} s(t)e^{-\frac{(t-nT)^2}{2}} e^{-jmFt} dt \tag{2.19}$$

and represent the sampled complex spectrogram of $s(t)$. The squared magnitude of the complex spectrogram is the waveform's physical spectrum. This discrete time signal expansion is known as the Gabor expansion[33, 35]. The functions $g_{mn}(t)$ are known as the Gabor logons and the coefficients c_{mn} are known as the Gabor coefficients. Gabor originally used time-frequency-shifted Gaussian functions as the logons due to their concentration in time and frequency[33].

The basis signals $g_{mn}(t)$ may be constructed so that they are localized and concentrated with respect to both time and frequency. If they are, the expansion coefficients c_{mn} indicate the signal's time-frequency content around the time-frequency location (nT, mF). Since the logon basis signals $g_{mn}(t)$ are all derived from the elementary function $g(t)$ through simple time-frequency shifts, they can be easily generated.

The Gabor transform of $s(t) = sin(2\pi ft)$ is shown in Figure 2.11 and the Gabor transform of a multicomponent signal, as represented by Equation 2.10, is shown in Figure 2.12. The frequency resolution is dependent on the particular basis signals that are used in the transform.

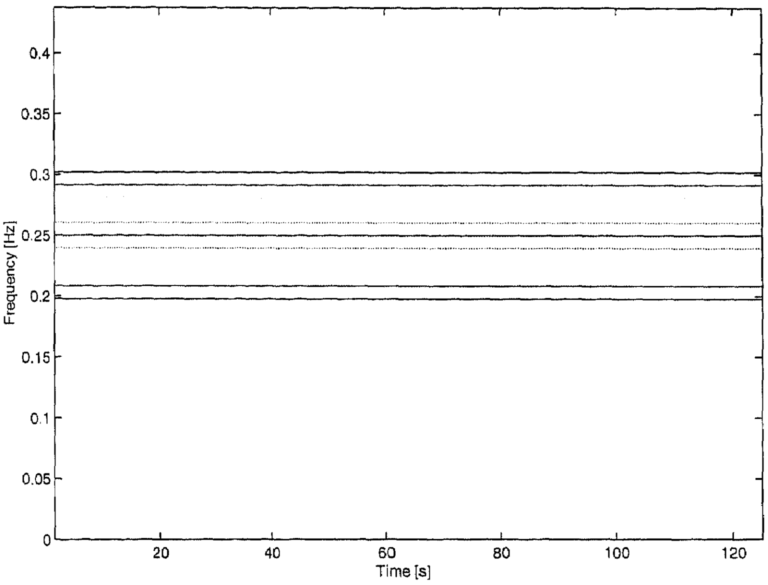

(a) Contour plot

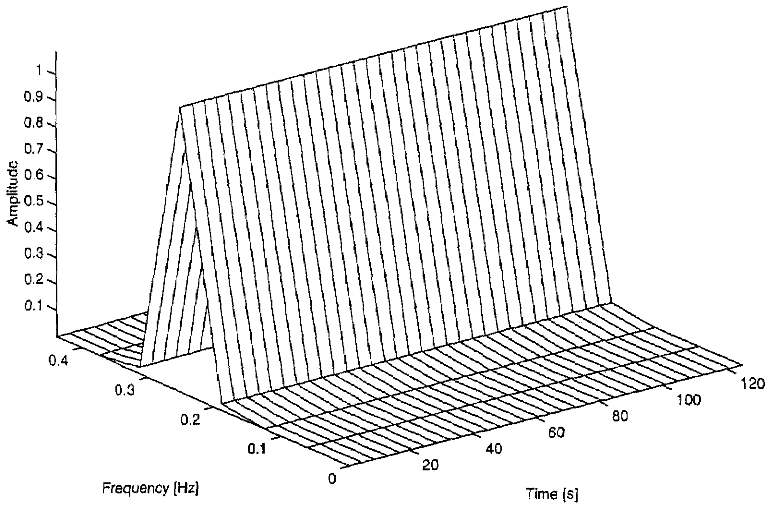

(b) Mesh plot

Figure 2.11 Gabor Transform of a sine wave

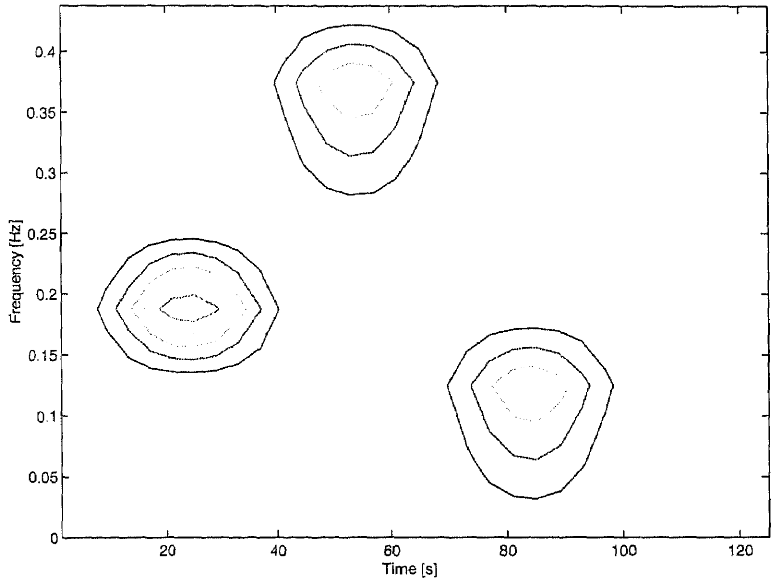

Figure 2.12 Gabor transform of a multicomponent signal

In the context of the Gabor expansion, there are two important issues relating to the Gabor basis, $g_{mn}(t)$: completeness and linear independence [12, 36]. The completeness of the Gabor basis guarantees that any finite-energy signal may be represented by a linear combination of a set of Gabor basis functions given in the Gabor expansion (2.18). A necessary condition for completeness of the Gabor basis is $TF < 1$; this condition is a bound on the density of the "time-frequency sampling grid". In the case of "critical sampling", where $TF = 1$, the number of Gabor coefficients equals the number of signal samples (assuming a band-limited signal sampled with minimum sampling rate) meaning the Gabor coefficients $G_x(n, m)$ do not contain any redundancy. Redundancy in the coefficients may be introduced by oversampling ($TF < 1$) to some degree. This is recommended so that the coefficients have some numerical stability, at the cost of the Gabor basis signals not being linearly independent.

2.3.3 Continuous Wavelet Transform

In the case of the STFT, once a window is chosen for the analysis, the time-frequency resolution is fixed over the entire time-frequency plane. If the resolution is allowed to vary within the time-frequency plan, a multi-resolution analysis will result. The Continuous Wavelet Transform (CWT) is a transform where all impulse responses of a filter bank are defined as scaled versions of the same prototype $h(t)$

$$h_a(t) = \frac{1}{\sqrt{\mid a \mid}} h(\frac{t}{a}), \tag{2.20}$$

where a is a scale factor (the constant $1/\sqrt{\mid a \mid}$ is used for energy normalization). The CWT is defined as

$$CWT_x(\tau, a) = \frac{1}{\sqrt{\mid a \mid}} \int x(t) h^*(\frac{t-\tau}{a}) dt. \tag{2.21}$$

Since the basic wavelet, $h(t)$ is used for all filter impulse responses, wavelet analysis is self-similar at all scales.

To relate this transform to the STFT, the basic wavelet $h(t)$ could be chosen as a modulated window [37]

$$h(t) = g(t) e^{j2\pi f_0 t}. \tag{2.22}$$

The frequency response of wavelet analysis filters in Equation 2.21 satisfy the equation

$$a = \frac{f_0}{f}. \tag{2.23}$$

$h(t)$ may be any band-pass function that meet certain criteria [12].

2.3.3.1 Scale and Resolution: The local frequency $f = af_0$ is associated with the scaling of the Wavelet Transform. This local frequency, that depends on the basic wavelet is related to time-scalings. It is not linked as it was in the case of the STFT to frequency modulation. The filter bank responses are dilated as scale increases. Therefore, large scale corresponds to contracted signals while small scale corresponds to dilated signals.

When a function $f(t)$ is scaled:

$$f(t) \rightarrow f(at), \text{ where } a > 0, \tag{2.24}$$

then it is contracted if $a > 1$ and expanded if $a < 1$. The CWT may be written as

$$CWT_x(\tau, a) = \frac{1}{\sqrt{a}} \int x(t) h^*(\frac{t-\tau}{a}) dt \tag{2.25}$$

or, by a change of variable, as

$$CWT_x(\tau, a) = \sqrt{a} \int x(at) h^*(t - \frac{\tau}{a}) dt \tag{2.26}$$

Equation 2.25 shows that as the scale increases, the filter impulse response $h(\frac{t-\tau}{a})$ becomes spread out in time therefore, only responds to long-time behavior. Equation 2.26 indicates that as the scale grows, an increasingly contracted version of the signal is seen through a constant length filter. The scale factor a has the same interpretation of the scale in maps; Large scales mean global views and small scales mean detailed views.

Figure 2.13 shows a representation of the tile concentration of the STFT and WT. The related concept of resolution is linked to the signal's frequency content. For example, low-pass filtering a signal keeps its scale, but reduces its resolution. Scale changes of continuous time signals do not alter their resolution since the scale change can be reversed.

2.3.3.2 Wavelet Analysis: The CWT may also be introduced as defining wavelets as basis functions. The basis function has already been shown as an inner product of the form

$$CWT_x(\tau, a) = \int x(t) h_{a,\tau}(t) dt \tag{2.27}$$

which measures the similarity between the signal and the basis functions

$$h_{a,\tau} = \frac{1}{\sqrt{a}} h(\frac{t-\tau}{a}) \tag{2.28}$$

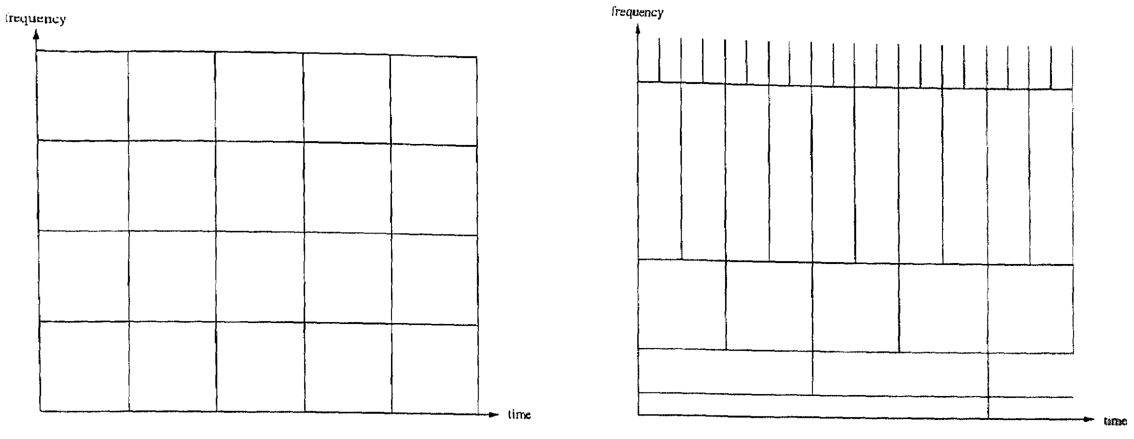

(a) Time-frequency plane for STFT

(b) Time-frequency plane for WT

Figure 2.13 Time-Frequency resolution of the STFT and WT of a given basis function

called wavelets. The wavelet analysis results in a set of wavelet coefficients which indicate how close the signal is to a particular basis function. Any general signal may be represented as a decomposition into wavelets. The analysis is done by computing the inner products, and the synthesis consists of summing all of the orthogonal projections of the signal onto the wavelets,

$$x(t) = c \int \int_{a>0} CWT(\tau, a) h_{a,\tau}(t) \frac{da d\tau}{a^2} \tag{2.29}$$

where c is a constant that depends on $h(t)$. Equation 2.29 is more complicated unless the assumptions that the signal and wavelets are either real-valued or complex analytic so that only positive dilations $a > 0$ need to be taken into account.

$h_{a,\tau}(t)$ are not orthogonal since they are defined for continuously varying a and τ, and are therefore very redundant. However, the reconstruction formula (Equation 2.29) is satisfied whenever $h(t)$ is of finite energy and band pass limited. If $h(t)$ is assumed sufficiently regular, then the reconstruction condition is $\int h(t)d(t) = 0$. The reconstruction only takes place in the sense of the signal's energy. The convergence of Equation 2.29 is related to the numerical robustness of the reconstruction [12].

2.3.3.3 Scalograms: The spectrogram was defined in section 2.3.1 as the square modulus of the STFT, and is a common tool in signal analysis. The spectrogram provides a distribution of the energy of the signal in the time-frequency plane. A similar distribution can be defined in the case of the wavelet transform. Since the CWT behaves like an orthonormal basis decomposition, it can be shown that it is isometric [37]. Therefore,

$$\int\int \mid CWT(\tau, a) \mid^2 \frac{d\tau da}{a^2} = E_x \tag{2.30}$$

where $E_x = \int \mid x(t) \mid^2 dt$ is the energy of the signal $x(t)$. In this manner, the scalogram is defined as the squared modulus of the CWT.

The scalogram of $s(t) = sin(2\pi f t)$ is shown in Figure 2.14 and the scalogram of the multicomponent signal of Equation 2.10 is shown in Figure 2.15.

In Figure 2.16, some differences between the scalogram and spectrogram are illustrated. In Figure 2.16(a), a Dirac pulse is analyzed around $t = t_0$, the CWT shows that the signal's behavior is localized around t_0 for small scales. In the case of STFT shown in Figure 2.16(b), the corresponding region is as large as the extent of the analysis window over all frequencies. Since the time-scale analysis of the CWT is logarithmic in frequency, the area of influence in the case of the CWT for a pure frequency f_0 in the signals increases with f_0, as shown in Figure 2.16(c). Figure 2.16(d) displays how the area remains constant in the case of a spectrogram.

2.3.3.4 Discrete Form: The basis functions (wavelets) act as an orthonormal basis for wavelet analysis. If the basis function, $h(t)$, is chosen correctly, then a discrete form of wavelet analysis may be used. The theory of wavelet frames [12] provides a framework that allows for choices in sample redundancy and sampling

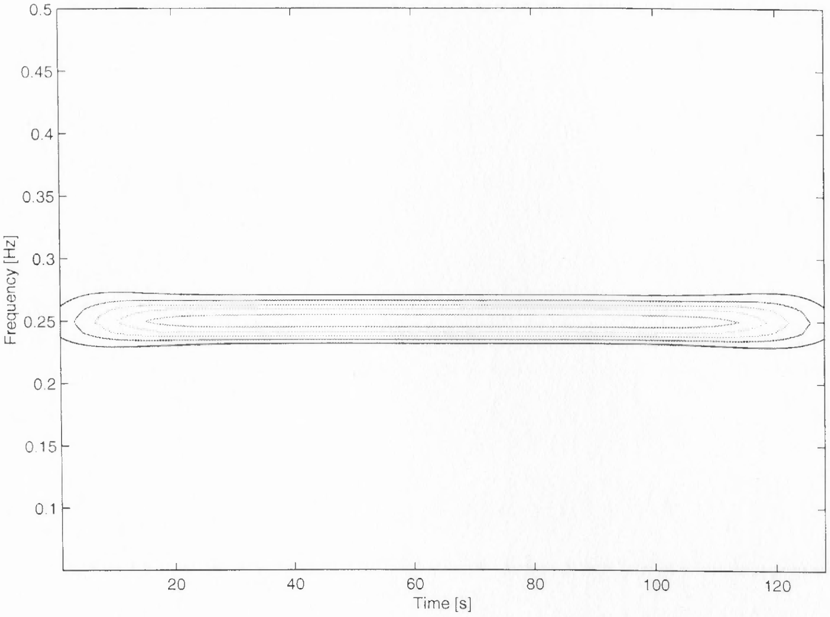

(a) Contour plot

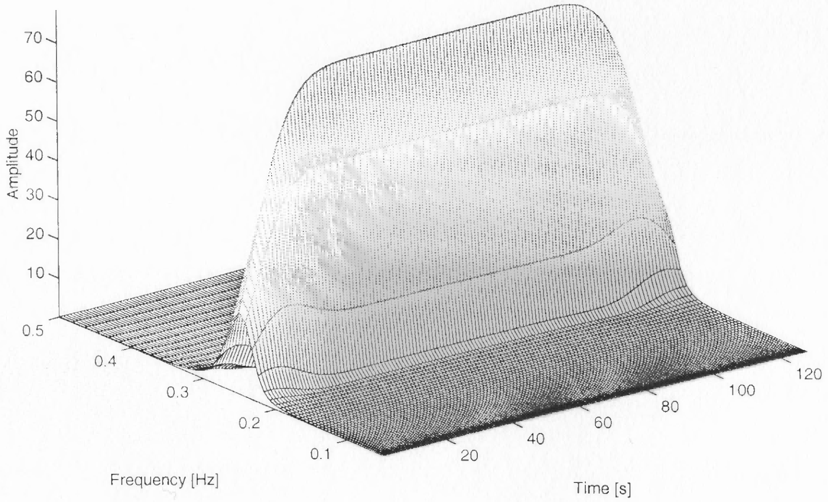

(b) Mesh plot

Figure 2.14 Scalogram of a sine wave

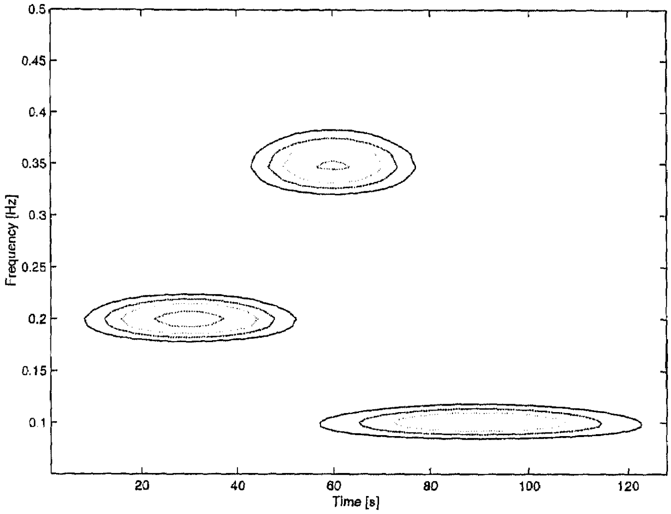

Figure 2.15 Scalogram of a multicomponent signal

density. Discrete wavelet transforms are essentially subband coders and subband coders have been used in speech and image compression, wavelets may be used in these applications easily. The field of discrete time wavelets (filterbanks, multiresolution pyramids[38], and subband coding[39]) are beyond the scope of this work.

2.3.4 Wigner-Ville Distribution

The STFT and Gabor Transform are both linear time-frequency representations. They are defined as linear representations because they satisfy the superposition or linearity principle,

$$s(t) = c_1 x_1(t) + c_2 x_2(t) \quad \rightarrow \quad T_x(t,\omega) = c_1 T_{x_1}(t,\omega) + c_2 T_{x_2}(t,\omega).$$

In any application involving multicomponent signals, linearity is a desirable property.

As has been shown in Figure 2.10, the STFT has a poor tradeoff between localization and time-frequency resolution. These limitations have caused researchers to look for other time-frequency representations. Several of the resulting time-frequency

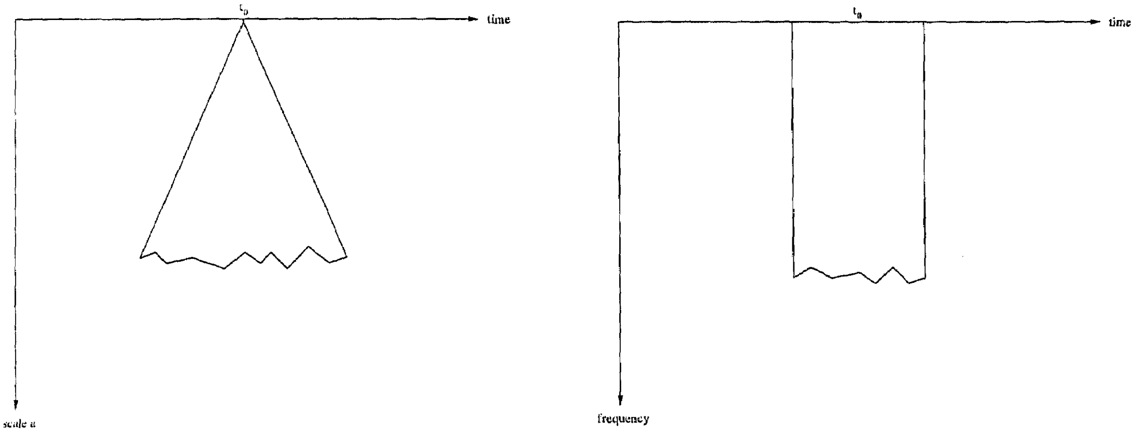

(a) Dirac pulse for CWT

(b) Dirac pulse for STFT

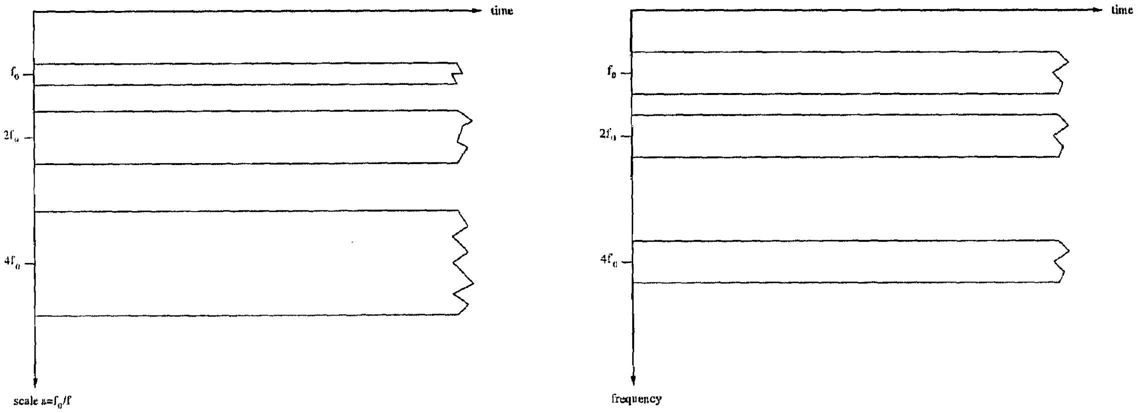

(c) Three sinusoids of $f_0, 2f_0, 4f_0$ for CWT

(d) Three sinusoids of $f_0, 2f_0, 4f_0$ for STFT

Figure 2.16 Regions of influence comparison of CWT and STFT representations are bilinear (quadratic) in the signal transformation. The Wigner-Ville distribution (WVD) was the first proposed bilinear Time-Frequency Distribution (TFD) [2]. The WVD of a signal $s(t)$ is given by:

$$\begin{aligned} W(t,f) &= \int_{-\infty}^{\infty} s(t+\frac{\tau}{2})s^*(t-\frac{\tau}{2})e^{-j2\pi f\tau}d\tau \\ &= \int_{-\infty}^{\infty} S^*(f+\frac{F}{2})S(f-\frac{F}{2})e^{-j2\pi Ft}dF \\ &= 2\int_{-\infty}^{+\infty} s(t+\tau)s^*(t-\tau)e^{-j4\pi f\tau}d\tau \end{aligned} \tag{2.31}$$

The WVD of $s(t) = sin(2\pi ft)$ is shown in Figure 2.17. As shown in this example, the frequency response of the sample signal is not smooth.

It may be shown that the various transforms are related to one another. The STFT can be expressed in terms of the WVD with the expression [23]

$$\mathcal{S}_x(t,f) = \int_{t'}\int_{f'} W_g(t'-t,f'-f)W_x(t',f')dt'df' \tag{2.32}$$

where W_g is the WVD of the STFT analysis window. The Gabor expansion and the WVD are related through the physical spectrum [40] given by

$$\mid c_{mn} \mid^2 = \int_{-\infty}^{\infty}\int_{-\infty}^{\infty} W_s(t,f)W_g\left(t-nT, f-\frac{mF}{2\pi}\right)dtdf \tag{2.33}$$

where $g(t) = \pi^{-1/4}e^{-t^2/2}$.

The scalogram may be written using Cohen's class for bilinear time-frequency energy distributions [41, 42] as

$$\mid T_z(t,a) \mid^2 = \int_{-\infty}^{\infty}\int_{-\infty}^{\infty} W_z(\tau,v)W_h(\frac{\tau-t}{a}, av)d\tau dv \tag{2.34}$$

where W_z is the WVD of the analyzed signal, $z(t)$ and W_h is the WVD of the basic wavelet with $(\frac{\tau-t}{a}, av)$ as time and frequency.

2.3.4.1 Cross-components: The WVD possesses a number of important mathematical properties that are detailed in [2, 43]. The WVD has limitations when using it as a practical time-frequency analysis technique due to the presence of nonlinear

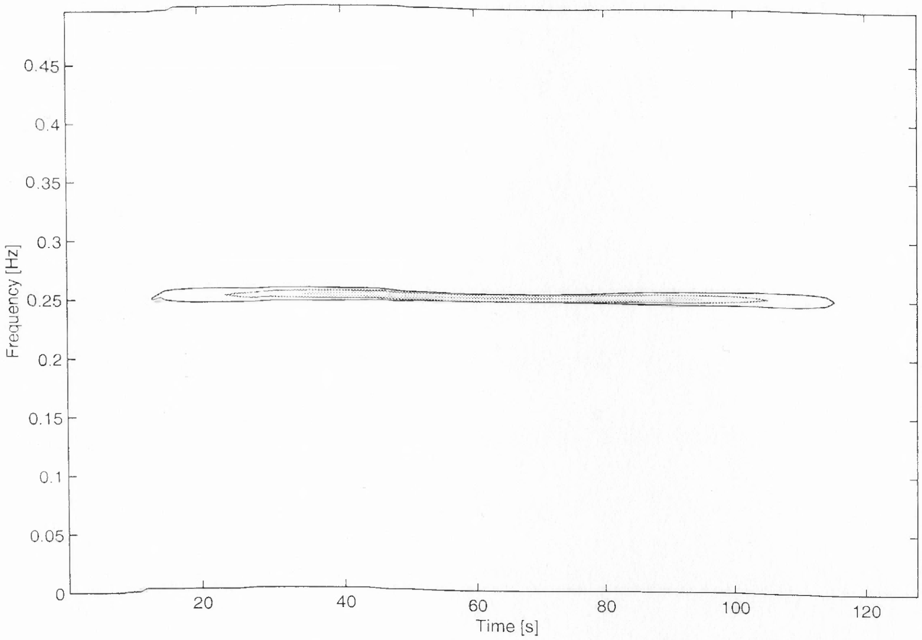

(a) Contour plot

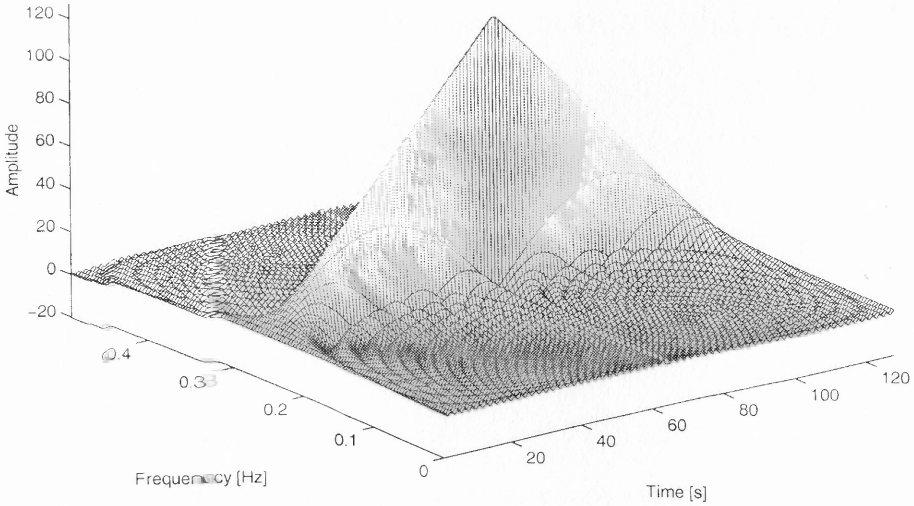

(b) Mesh plot

Figure 2.17 WVD transform of a sine wave artifacts called cross-components. The cross-Wigner distribution of two signals, s_1 and s_2 is

$$W_{s_1,s_2}(t,f) = \int_{-\infty}^{\infty} s_1(t+\frac{\tau}{2})s_2^*(t-\frac{\tau}{2})e^{-\jmath 2\pi f\tau}d\tau. \tag{2.35}$$

The Wigner-Ville distribution of a two-component signal, $s(t) = s_1(t) + s_2(t)$, is

$$W_{s,s} = W_{s_1,s_1}(t,f) + W_{s_2,s_2}(t,f) + \Re\left[W_{s_1,s_2}(t,f)\right]. \tag{2.36}$$

The Wigner distribution of the sum of two signals is not the sum of the Wigner distributions of each signal. For $W_{s,s}$, the first two terms are the auto-components of the Wigner distribution of s_1 and s_2. The last term is the cross-component and is made up of two overlapping components, W_{s_1,s_2} and W_{s_2,s_1}. The cross-component is located midway between the two auto-components on the time-frequency plane and oscillates with a spatial frequency that is inversely proportional to their separation [23].

In a multicomponent signal, one cross-component will appear between each pair of auto-components. The number of cross-components increases quadratically as the number of components in the signal increases. A n-component signal has

$$\begin{pmatrix} n \\ 2 \end{pmatrix} = \frac{n(n-1)}{2}$$

cross-components. These make the WVD of multicomponent signals difficult to interpret and enhance noise.

In Figure 2.18, the WVD of the signal of Equation 2.10 is shown with the three cross-components.

2.3.4.2 Discrete form of the Wigner Distribution: The discrete Wigner distribution (DWD) with a discrete frequency variable is defined for a discrete time signal by

$$W(n,k) = 2 \sum_{m=-(N-1)/2}^{(N-1)/2} z(n+m)z^*(n-m)e^{-\jmath 4\pi mk/N} \tag{2.37}$$

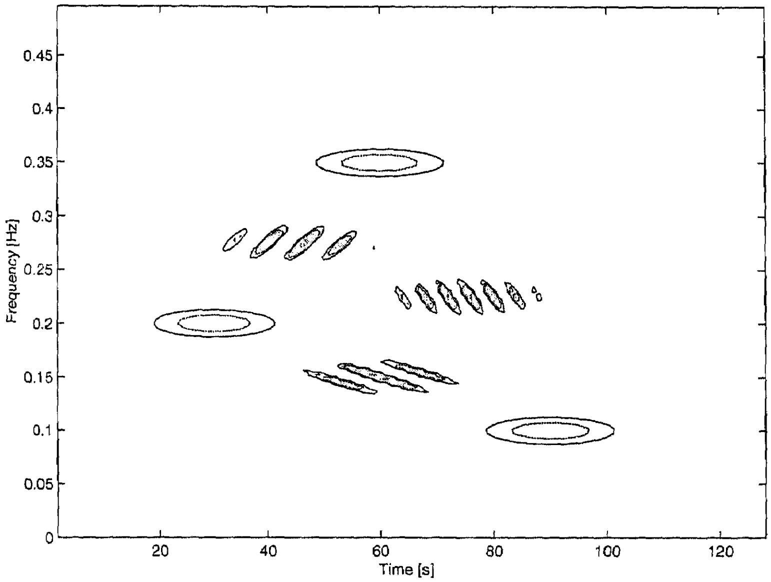

Figure 2.18 Example of WVD cross terms

where the time signal is of length N', band-limited to f_m, $N = N'$ for N' odd and $N = N' + 1$ for N' even; $0 \leq n \leq N'$, $0 \leq k \leq N$, $-(N-1)/2 \leq m \leq (N-1)/2$; and n, k, and m are the discrete variables corresponding to the continuous variables t, f, and τ.

The discrete-time values may be converted to the corresponding continuous-time values using the transformations:

$$f = \frac{f_s k}{2N'}, \quad t = \frac{n}{f_s'}, \text{ and } \tau = \frac{m}{f_s'} \tag{2.38}$$

where f_s is the sampling frequency which must be at least $2f_m$ to satisfy the Nyquist criterion where f_m is the maximum frequency of the signal. Notice that Equation 2.37 may be viewed as a slightly modified Discrete Fourier transform.

2.4 Time-Frequency Analysis of Linear FM

This section describes the estimation of the instantaneous frequency using the four previously introduced TF analysis techniques; the Short-Time Fourier transform, the Gabor expansion, the Continuous Wavelet transform and the Wigner-Ville distribution. Analytic expressions for the output of each method to a given linear FM signal are developed and it is shown how the chirp rate can be extracted using each technique. The performance in the presence of additive white Gaussian noise is compared with the Cramér-Rao bound analytically for the WVD and by simulations for all four techniques.

2.4.1 The Wigner-Ville Distribution

With an input signal of a continuous chirp, $z(t) = e^{j\frac{\mu}{2}t^2}$, the WVD is given by

$$W_z(t,f) = \int_{-\infty}^{\infty} e^{j\mu(t+\tau/2)^2/2} e^{-j\mu(t-\tau/2)^2/2} e^{-j2\pi f\tau} d\tau = \delta\left(f - \frac{\mu t}{2\pi}\right) \tag{2.39}$$

using Equation 2.32 explicitly. For the discrete finite time duration waveform $z(n) = e^{j\frac{\mu}{2}n^2T_r^2}$, the WVD is given by

$$\begin{aligned} W_z(n,m) &= \sum_{k=-N/2}^{N/2} e^{j\frac{\mu}{2}(n+k)^2T_r^2} e^{-j\frac{\mu}{2}(n-k)^2T_r^2} e^{-j4\pi\frac{mk}{N}} \\ &= \sum_{k=-N/2}^{N/2} e^{j4\frac{\mu}{2}nkT_r^2} e^{-j4\pi\frac{mk}{N}}. \end{aligned} \tag{2.40}$$

The magnitude squared of the WVD is then given by

$$\mid W_z(n,m) \mid^2 = \left| \frac{\sin(2N(\frac{\mu}{2}nT_r^2 - \frac{\pi m}{N}))}{\sin(2(\frac{\mu}{2}nT_r^2 - \frac{\pi m}{N}))} \right|^2 \tag{2.41}$$

where we used the identity $\left|\sum_{n=-N/2}^{N/2} e^{jn\alpha}\right| = \sin\left(\frac{N}{2}\alpha\right) / \sin\left(\frac{1}{2}\alpha\right)$. The WVD (2.41) converges to the well known limiting form Equation 2.39.

Figure 2.19(a) shows the WVD of a linear FM signal with a chirp rate of 0.00117 Hz/sec. The window size of the WVD is 64 points. A 3-D mesh plot of this signal is shown in Figure 2.19(b). The chirp may be seen clearly in these figures.

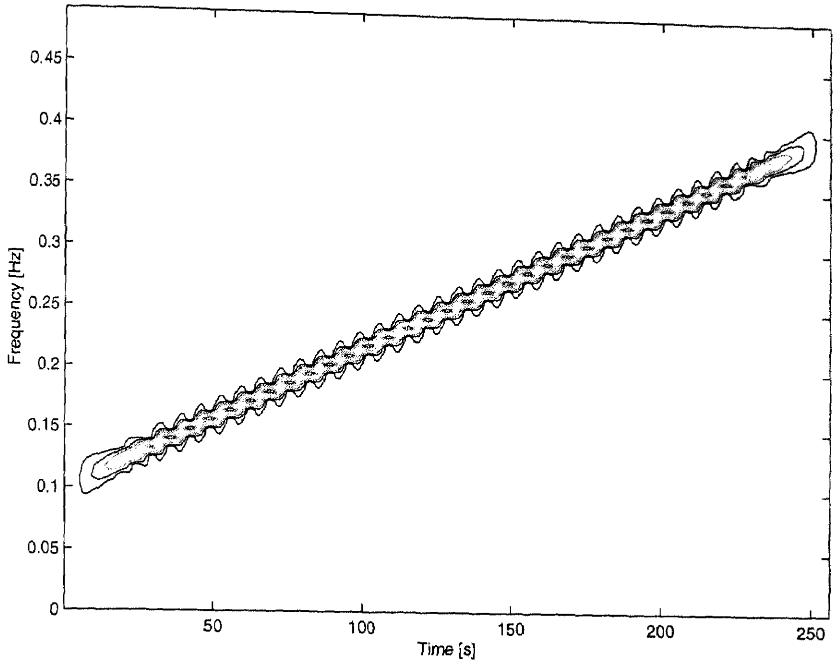

(a) Contour plot of the WVD of a linear FM signal

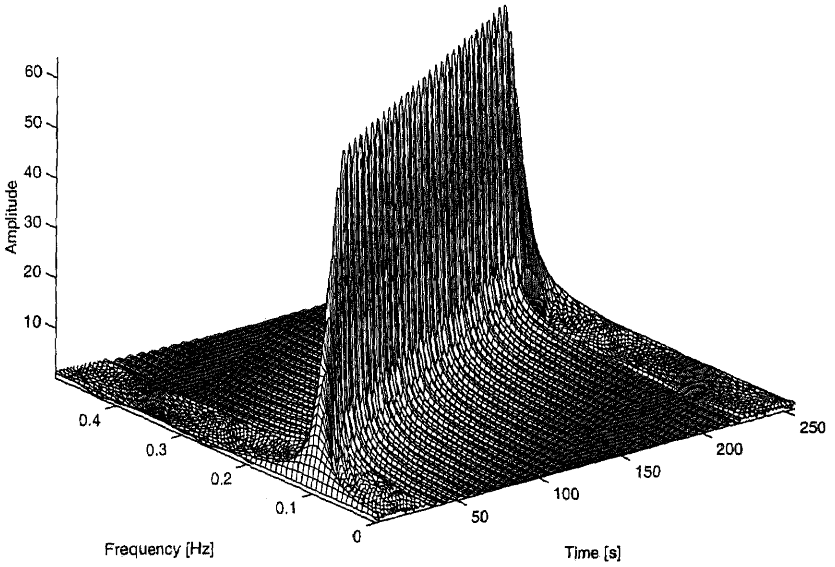

(b) 3-D mesh plot of the WVD of a linear FM signal

Figure 2.19 WVD of a linear FM signal

2.4.2 The Short Time Fourier Transform

The Short Time Fourier transform of a continuous chirp signal $z(t) = e^{\jmath\frac{\mu}{2}t^2}$, and for a Gaussian analyzing window $h(t) = (\pi\sigma_h^2)^{-(1/4)}\ e^{-(t^2/2\sigma_h^2)}$, has been calculated as [44]:

$$S_z(\tau,\omega) = k_1 \exp\left[-k_2(\tau - \frac{\omega}{\mu})^2\right] \cdot \exp\left\{\jmath\left[k_3(\tau - \frac{\omega}{\mu})^2 - \frac{\omega^2}{2\mu}\right]\right\} \tag{2.42}$$

where

$$\begin{aligned} k_1 &= (\pi\sigma_h^2)^{-(1/4)}\sigma_h\sqrt{\frac{(\jmath k_2 - k_3)}{\pi\mu(k_2^2 - k_3^2)}} \\ k_2 &= \frac{\sigma_h^2}{2(\sigma_h^4 + \frac{1}{\mu^2})} \\ k_3 &= \frac{\frac{1}{\mu}}{2(\sigma_h^2 + \frac{1}{\mu^2})}. \end{aligned}$$

The spectrogram, or the magnitude squared of the STFT, of a chirp is then given by:

$$\mid S_z(t,\omega) \mid^2 = \mid k_1 \mid^2 \exp\left[-2 \mid k_2 \mid (\tau - \frac{\omega}{\mu})^2\right]. \tag{2.43}$$

It should be noted that Equation 2.42 is centered along the line $\omega = \mu\tau$ representing the linear time dependency of the instantaneous frequency of the chirp signal.

Figure 2.20(a) shows the spectrogram of a linear FM signal with a chirp rate of 0.00117 Hz/sec. The hamming window size of the STFT is 64 points. A 3-D mesh plot of this signal is shown in Figure 2.20(b). As in the case of the WVD, the chirp may be seen clearly in these figures.

2.4.3 The Gabor Expression

Using Equation 2.19 the Gabor expansion of the linear FM waveform $z(t) = e^{\jmath\frac{\mu}{2}t^2}$ results in the sampled spectrum

$$\mid c_{mn} \mid^2 = \sqrt{\frac{4\pi}{1+\mu^2}} e^{\frac{(mF-\mu nT)^2}{(1+\mu^2)}}. \tag{2.44}$$

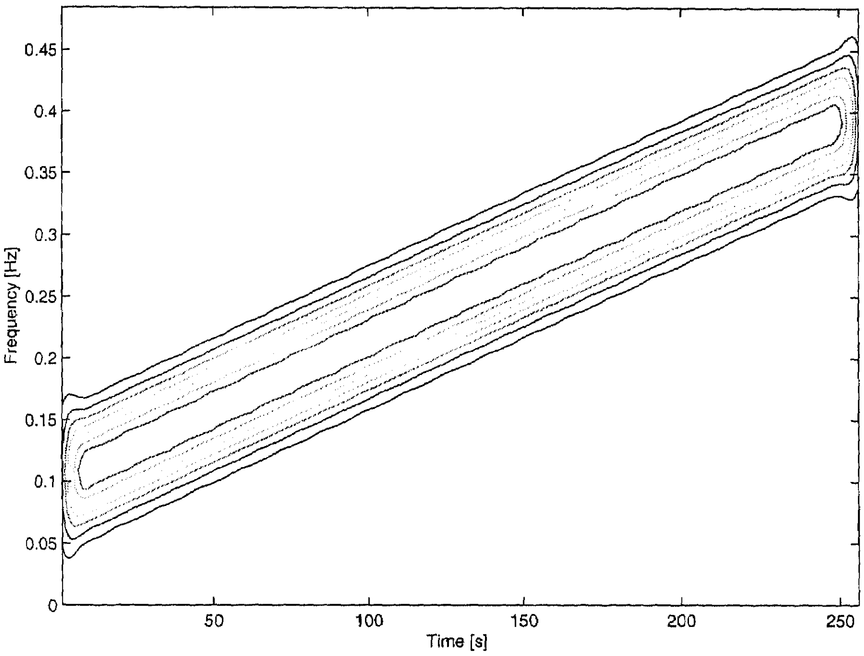

(a) Contour plot of the STFT of a linear FM signal

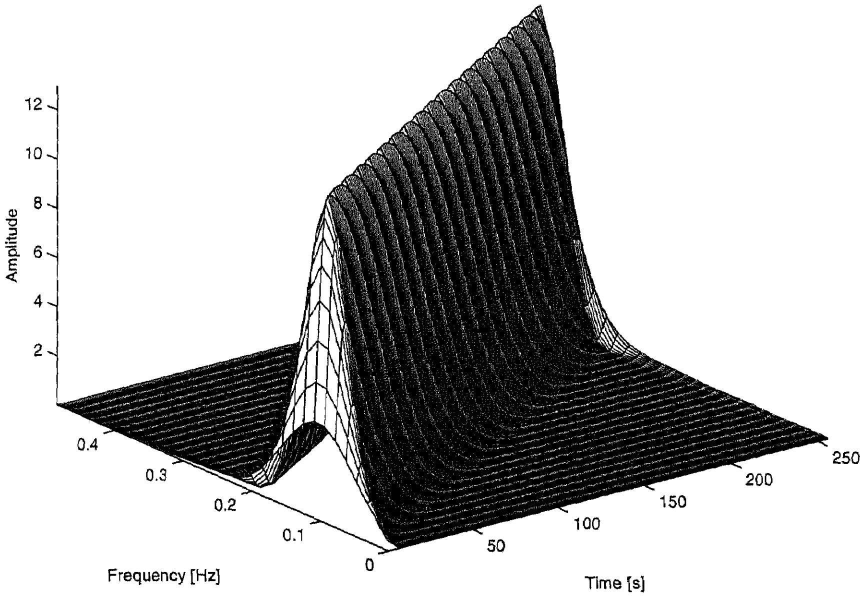

(b) 3-D mesh plot of the STFT of a linear FM signal

Figure 2.20 STFT of a linear FM signal

It is very clear from Equations 2.39 and 2.44 that the spectrum of $z(t)$ is concentrated along the line $2\pi f = \mu t$ and equivalently $mF = \mu nT$. The concentration represents the instantaneous frequency. The sampled spectrum given by Equation 2.44 can also be computed from the weighted WVD using Equation 2.33:

$$| c_{mn} |^2 = 2\int_{-\infty}^{\infty}\int_{-\infty}^{\infty} \delta\left(f - \frac{\mu t}{2\pi}\right) e^{-(t-nT)^2-(2\pi f-mF)^2} dt df. \tag{2.45}$$

The Gabor expansion of a linear FM signal with a chirp rate of 0.00117 Hz/sec is shown in Figure 2.21(a). The time-frequency plane is represented by a rectangular grid of size 32x16 with the signal oversampled by a factor of 4. The 3-D mesh plot of this signal is shown in Figure 2.21(b). The chirp is clearly displayed in these figures by the Gabor expansion. The artifact to the right of the time scale is a result of the parameters used in the transform.

2.4.4 The Continuous Wavelet Transform

Using Equations 2.34 and 2.39, the scalogram of the linear FM waveform $z(t) = e^{j\frac{\mu}{2}t^2}$ is shown to be

$$| T_z(t, a) |^2 = \int_{-\infty}^{\infty}\int_{-\infty}^{\infty} \delta(v - \frac{\mu\tau}{2\pi}) W_h(\frac{\tau - t}{a}, av) f\tau dv. \tag{2.46}$$

As in the case of the other TF techniques, the instantaneous frequency of the linear FM waveform is represented in this equation.

The scalogram of a linear FM signal with a chirp rate of 0.00117 Hz/sec is shown in Figure 2.22(a). The scalogram was analyzed with a window of 32 points at the coarsest scale. The 3-D mesh plot of this signal is shown in Figure 2.22(b). As in the other cases, the chirp may be seen in these figures.

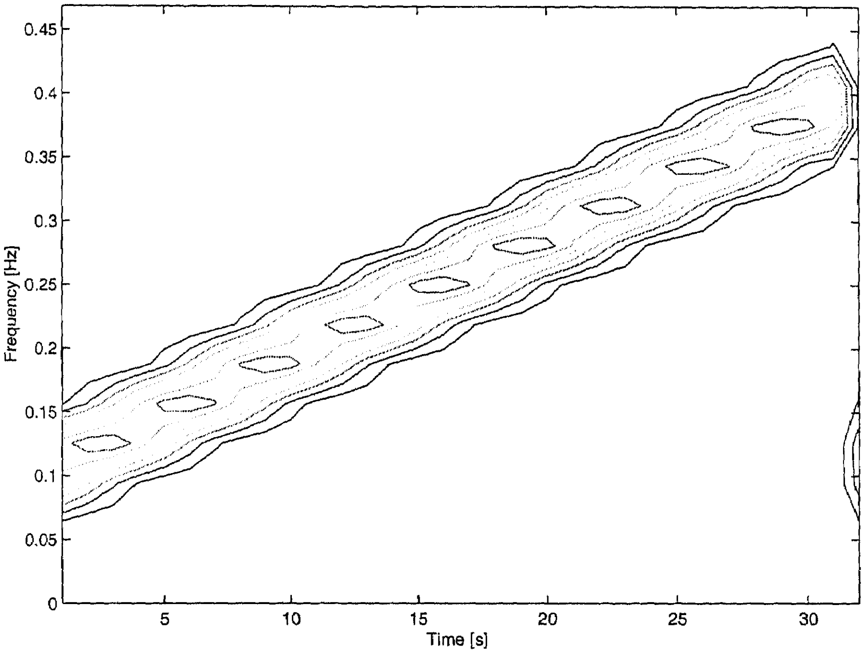

(a) Contour plot of the Gabor expansion of a linear FM signal

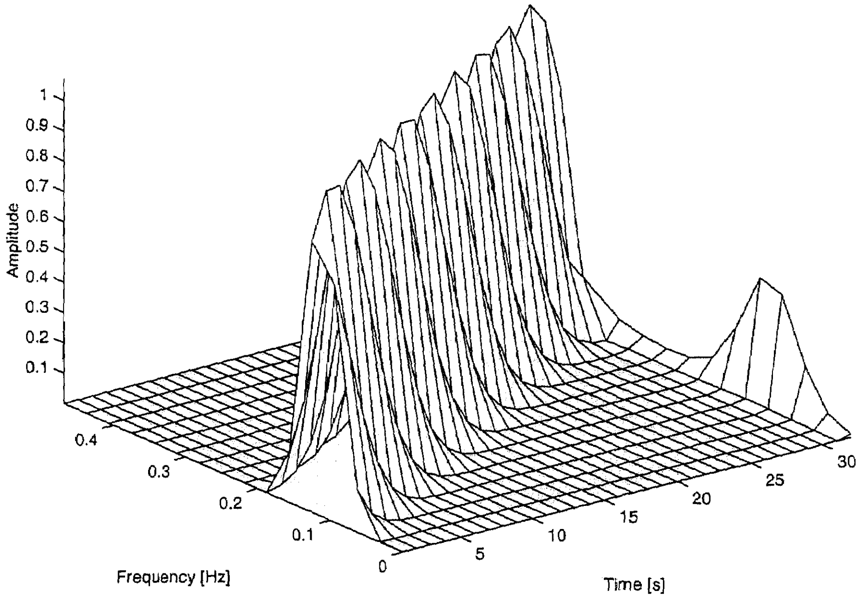

(b) 3-D mesh plot of the Gabor expansion of a linear FM signal

Figure 2.21 Gabor expansion of a linear FM signal

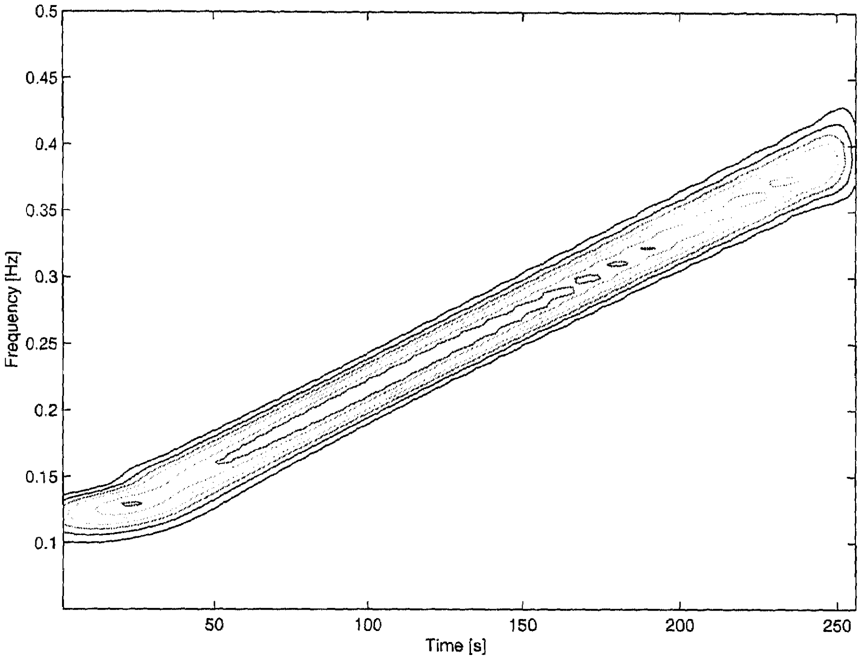

(a) Contour plot of the scalogram of a linear FM signal

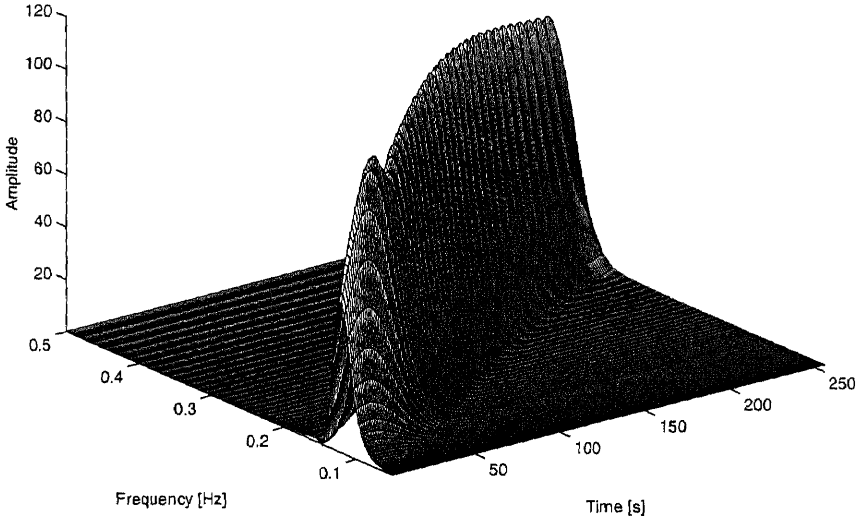

(b) 3-D mesh plot of the scalogram of a linear FM signal

Figure 2.22 Scalogram of a linear FM signal

2.5 Time-Frequency Analysis in Noise

The discrete chirp signal in the presence of additive noise is given by:

$$z(n) = Ae^{j\phi(n)} + v(n) \tag{2.47}$$

where $\phi(n) = \frac{\mu}{2}n^2T_r^2$ is the chirp phase, and $v(n)$ are independent samples of a complex white Gaussian noise process with zero mean and variance σ^2. The input SNR is given by SNR $= A^2/\sigma^2$. From (2.40), the WVD kernel can be written as:

$$\begin{aligned} z(n+k)z^*(n-k) &= A^2e^{j[\phi(n+k)-\phi(n-k)]} + Ae^{j\phi(n+k)}v^*(n-k) + \\ &\quad Ae^{-j\phi(n+k)}v(n+k) + v(n+k)v^*(n-k). \end{aligned} \tag{2.48}$$

In the expression above, the noise component is $v_1 = Ae^{j\phi(n+k)}v^*(n-k) + Ae^{-j\phi(n+k)}v(n+k) + v(n+k)v^*(n-k)$. The resultant noise power in the kernel is given by:

$$\begin{aligned} P_v &= E\left[|v_1|^2\right] \\ &= 2A^2\sigma^2 + \sigma^4. \end{aligned}$$

There are only $N/2$ independent samples in the kernel (since it is conjugate symmetric), so the variance of the noise at the output of the WVD is scaled by a factor of $N/2$ rather than N. Therefore, the SNR of the WVD output is:

$$\text{SNR}_{\text{WVD}} = \frac{A^4(N/2)}{2A^2\sigma^2 + \sigma^4}. \tag{2.49}$$

Note that the input SNR is given by NA^2/σ^2. Equation 2.49 can be used to compute a bound on the chirp estimation error. The performance of the WVD is compared against the Cramér-Rao bound (CRB) on the IF estimation variance for a a complex single tone in additive white Gaussian noise. The CRB is achieved by the Discrete Fourier transform (DFT) of the single tone signal and is given by [45]:

$$\text{var}_{\text{CR}}(\hat{f}) = \frac{12}{(2\pi)^2T_r^2(\text{SNR})(N^2-1)} \tag{2.50}$$

where for the DFT, the output SNR is N times the input SNR: SNR $= NA^2/\sigma^2$. The bound on the performance of the WVD is found by substituting the SNR from Equation 2.49 in Equation 2.50. Furthermore, when compared to the DFT, the WVD has its frequency scaled by a factor of 2 (see the term $e^{-j4\pi\frac{mk}{N}}$ of Equation 2.40). This leads to a reduction by a factor of 4 in the variance of the frequency estimate. Therefore, the variance of the WVD for a chirp signal is:

$$\mathrm{var}_{\mathrm{WVD}}(\hat{f}) = \frac{12(2A^2\sigma_n^2 + \sigma_n^4)}{(2\pi)^2 T_r^2 (2A^4 N)(N^2-1)}. \tag{2.51}$$

At high input SNR ($A^2 \gg \sigma^2$), this equation reduces to:

$$\mathrm{var}_{\mathrm{WVD}}(\hat{f}) = \frac{12\sigma^2}{(2\pi)^2 T_r^2 A^2 N(N^2-1)} \tag{2.52}$$

which is the same as Equation 2.50. Since this equation is the variance of the maximum-likelihood estimate of the frequency of a stationary sinusoid in white Gaussian noise [45], it can be said that the WVD is an optimal estimator of the IF for chirp signals at high SNR.

2.6 Application of TF Analysis to IF Estimation

The estimate of the instantaneous frequency is provided by the peak of the WVD as a function of time [6]. For the WVD the peak is found from Equation 2.41 and occurs when:

$$\frac{\mu}{2} n T_r^2 = \frac{\pi m}{N}. \tag{2.53}$$

It is evident from this relation that there is a linear relationship between the time and frequency coordinates (n and m, respectively). The slope of this line is given by:

$$\begin{aligned} S_o &= \frac{m}{n} \\ &= \frac{\frac{\mu}{2} N T_r^2}{\pi}. \end{aligned} \tag{2.54}$$

Consequently, when the slope S_o is measured from the WVD, the chirp rate can be found from the relation:

$$\mu = \frac{2\pi S_o}{NT_r^2}. \tag{2.55}$$

As can be seen from Equations 2.42 and 2.44, both the STFT and the Gabor expansion reach maxima along the line $\omega = \mu\tau$. Using the frequency and time discretizations $\omega = 2\pi m \ / \ NT_r$ and $\tau = nT_r$, and the slope S_o measured from the STFT and Gabor expansion respectively, the chirp rate μ can be calculated using Equation 2.55.

The instantaneous frequency of a simulated linear-FM signal (chirp) was estimated by each of the TF analysis techniques considered. For each method, the input signal was a linear FM signal of 256 points sampled at 1000 Hz. The chirp rate was 8.84 Hz/sec. The SNR of the input signal was varied from 15 dB to -15 dB in 1 dB steps and 250 trials were averaged for each SNR level. The data was analyzed as follows: for the WVD a K=64 point square window, for the STFT a 64 point hamming window, for the Gabor expansion, a $32x16$ TF grid that was oversampled by 4, and the scalogram (CWT) was analyzed with a window of 32 points at the coarsest scale. For each transform, and in order to minimize frequency quantization errors, the peak response at each time sample was found from an interpolation along the frequency axis. After the peaks for each time sample were determined the chirp rate was found from the least-squares linear fit through these maxima. The error between this line and the actual IF of the input was found and is plotted for each TF analysis technique in Figure 2.23. The CRB for $N = 64$ is plotted on the figure also. It can be seen that the WVD approaches this bound at high SNR. The STFT is closer to the bound than the Gabor expansion and the scalogram. All methods exhibit a threshold. This figure confirms the optimality of the WVD [7] and the relative advantages of the STFT over the Gabor expansion [11].

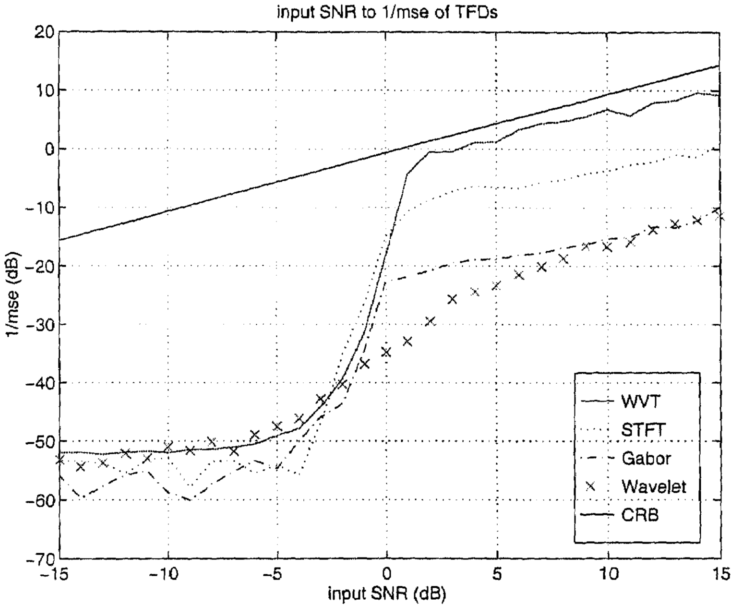

Figure 2.23 Input SNR vs 1/mse of CRB, WVD, STFT, Gabor expansion, and CWT

2.7 Estimation of Target Parameters

In this section we apply the TF analysis techniques to the SAR data for the purpose of extracting the target motion parameters. The SAR data was provided by the Naval Air Warfare Center, Warminster PA and was collected using their P-3 SAR system at X-band. The data consisted of a boat target of opportunity moving in parallel with the SAR platform within an open ocean background. The data was processed using each of the TFD techniques and the boat speed was estimated for each case. However, the absolute accuracy of the estimates could not be assessed since the true boat velocity was not available. The SAR data has been analyzed after range compression, but prior to azimuth compression. The SAR signal phase returned from a single point target is given by the functional relation:

$$\Psi(t) = \frac{\kappa}{R_o}(v_{px} - v_{tx})^2 t^2. \tag{2.56}$$

where:

$\Psi(t)$ = Doppler phase shift due to relative motion between platform and target

κ = $2\pi/\lambda$is the wavenumber

R_o = range to target

v_{px} = SAR platform velocity

v_{tx} = target along-track (azimuth) velocity

If the derivative of $\Psi(t)$ is taken with respect to t we obtain a relation between the rate of change of the phase (angular frequency) and the SAR-target relative velocity.

$$\Omega(t) = \frac{2\kappa}{R_o}(v_{px} - v_{tx})^2 t. \tag{2.57}$$

If the SAR pulse repetition interval is T_r, then $t = nT_r$. From Equation 2.57, it can be seen that the relation between frequency and time is linear. The slope of the frequency curve is given by:

$$\frac{\Delta\Omega}{\Delta n} = \frac{2\kappa}{R_o}(v_{px} - v_{tx})^2 T_r. \tag{2.58}$$

The relative velocity $v_x = v_{px} - v_{tx}$ can then be found from the relation:

$$v_x = \sqrt{\frac{(\Delta\Omega/\Delta n)R_o}{2\kappa T_r}} \tag{2.59}$$

where $(\Delta\Omega/\Delta n)$ can be computed from relation: $\frac{\Delta\Omega}{\Delta n} = 2\pi\frac{\Delta m}{NT_r\Delta n} = \frac{2\pi S_o}{NT_r}$. The slope S_o is determined from the outputs of each of the transforms. Finally, the relation between the slope of the time-frequency characteristic at the output of each TF analysis technique and the relative velocity is given by:

$$\begin{aligned} v_x &= \sqrt{\frac{\pi S_o R_o}{\kappa N T_r^2}} && (2.60) \\ &= \sqrt{\frac{\lambda S_o R_o}{2 N T_r^2}}. && (2.61) \end{aligned}$$

The relative velocity of the boat was estimated from the SAR data using each transform and Equation 2.61. The SNR was coarsely estimated from the SAR data to be ≈ 15.4 *dB*. In the case of the WVD, the window was set to K=64 points. The target's relative velocity was estimated to be 7.1 meters/sec. The contour plot for the output of the WVD is shown in Figure 2.24. In the case of the STFT, a 64 point hamming window was utilized. The target's relative velocity was estimated to be 7.2 meters/sec. The contour plot for the output in the case of the STFT is shown in Figure 2.25. For the case of the Gabor expansion, the target's relative velocity was estimated to be 6.5 meters/sec using a $32x16$ TF grid oversampled by 4. The contour plot for the output in the case of the Gabor expansion is shown in Figure 2.26. Finally, for the case of the scalogram (CWT), the target's relative was estimated to be 7.4 meters/sec. The contour plot for the scalogram is shown in Figure 2.27. As can be seen from the estimated relative velocities, the numerical results from the four techniques are very similar, however, the representation of the data is not. In our scenario, the contour plot of the WVD provides the representation with the most sharply defined chirp characteristic. This is partially due to the particular window size that was used in the transforms and the specific transformed signal. The chirp characteristics of the moving target for the STFT, the Gabor expansion, and the scalogram are not as obvious but are also apparent. In our simulations, a gaussian function was used with the CWT. If a chirp had been used in some form with the CWT as a basis function, the results for the CWT may have improved.

2.7.1 Another Chirp in the Signal

A second chirp was added to the SAR signal containing the moving target at a signal level that was 5 *dB* higher that the original signal. This level was calculated by comparing the energy contained in the added signal and the original SAR image. After transforming the combination of this new signal into a TF representation, a mask was created that nulled the areas of the transform domain above a certain level for each particular transform. The relative velocity of the remaining chirp was

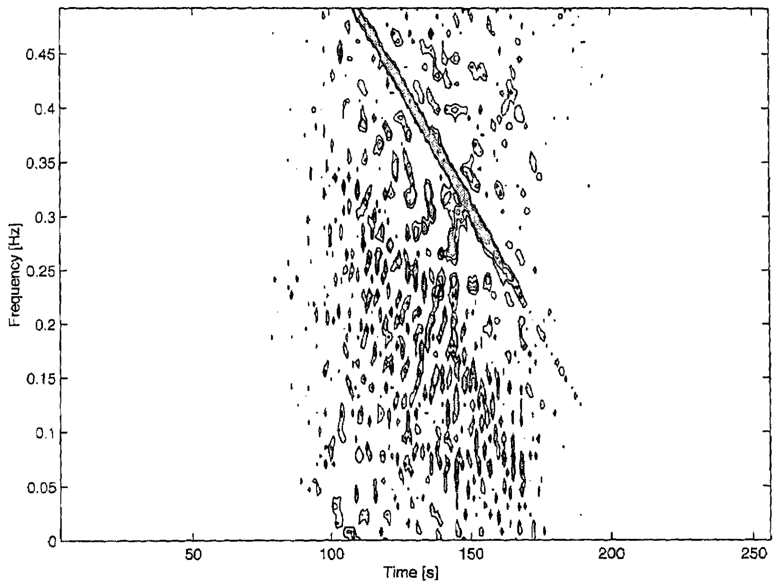

(a) Contour plot

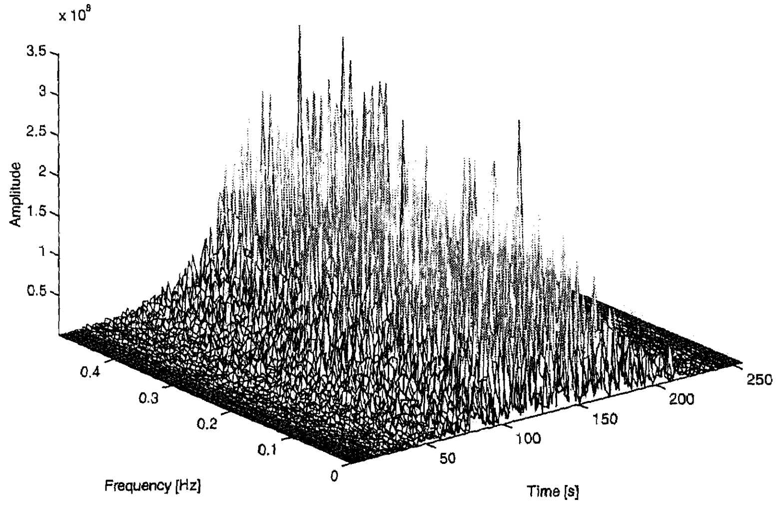

(b) Mesh plot

Figure 2.24 SAR image processed using the WVD

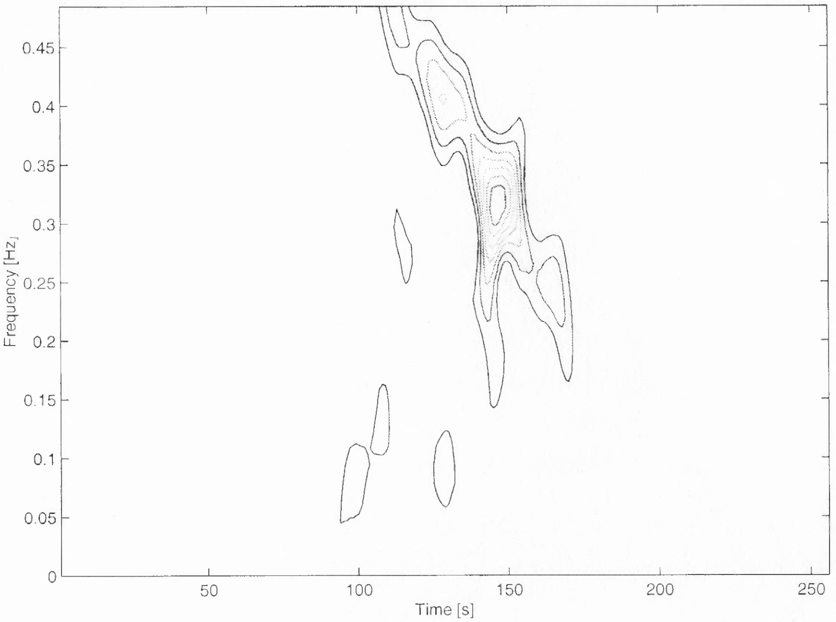

(a) Contour plot

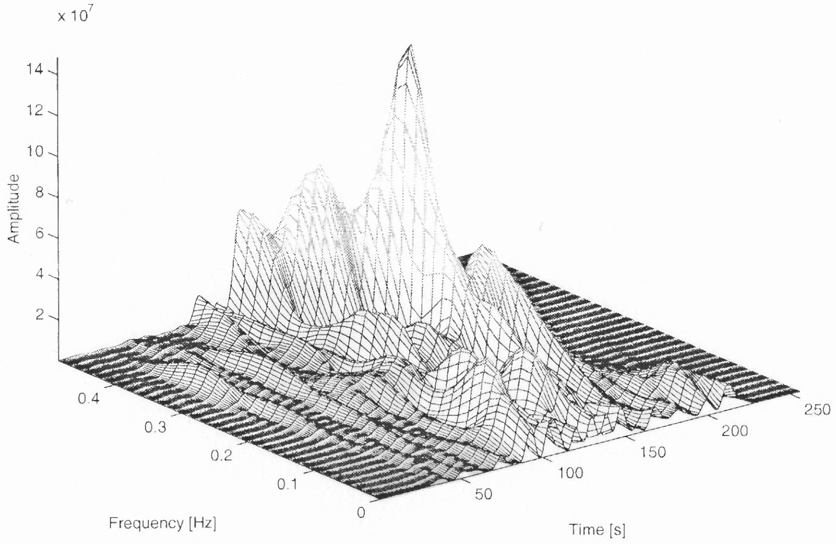

(b) Mesh plot

Figure 2.25 SAR image processed using the STFT

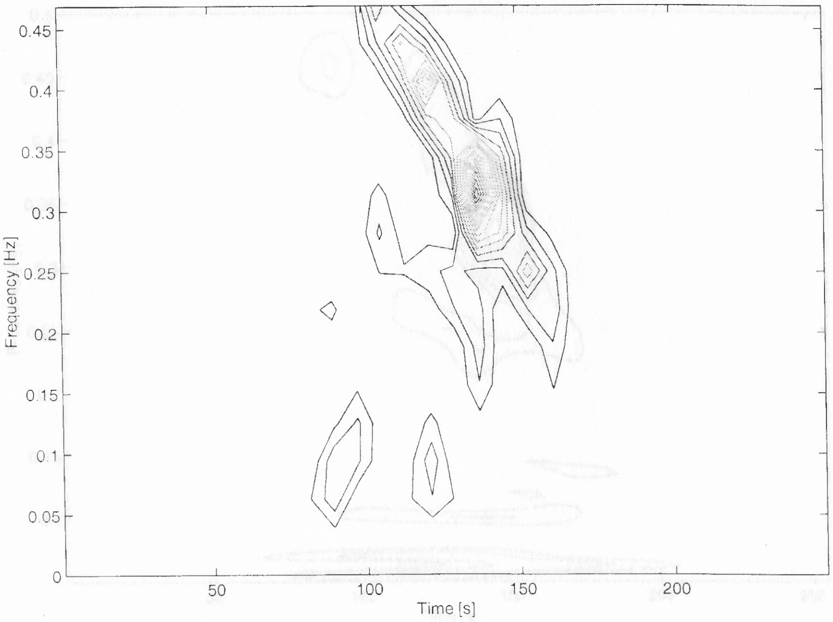

(a) Contour plot

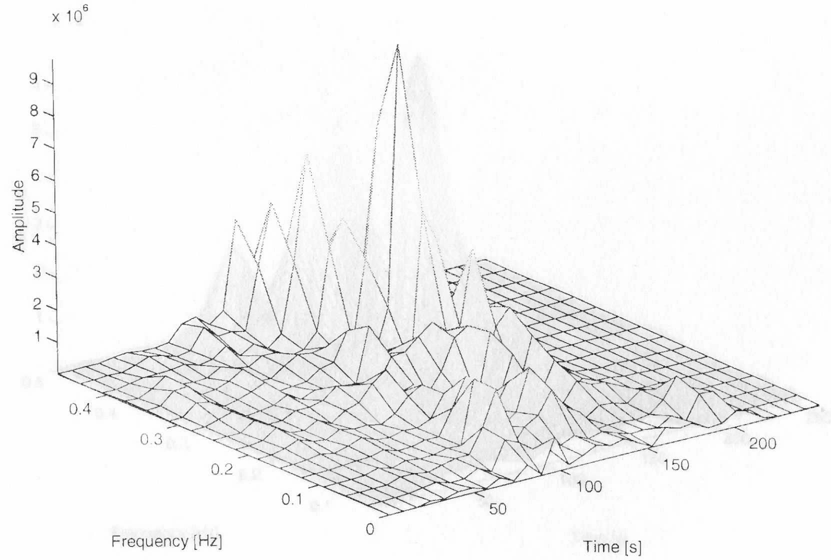

(b) Mesh plot

Figure 2.26 SAR image processed using the Gabor expansion

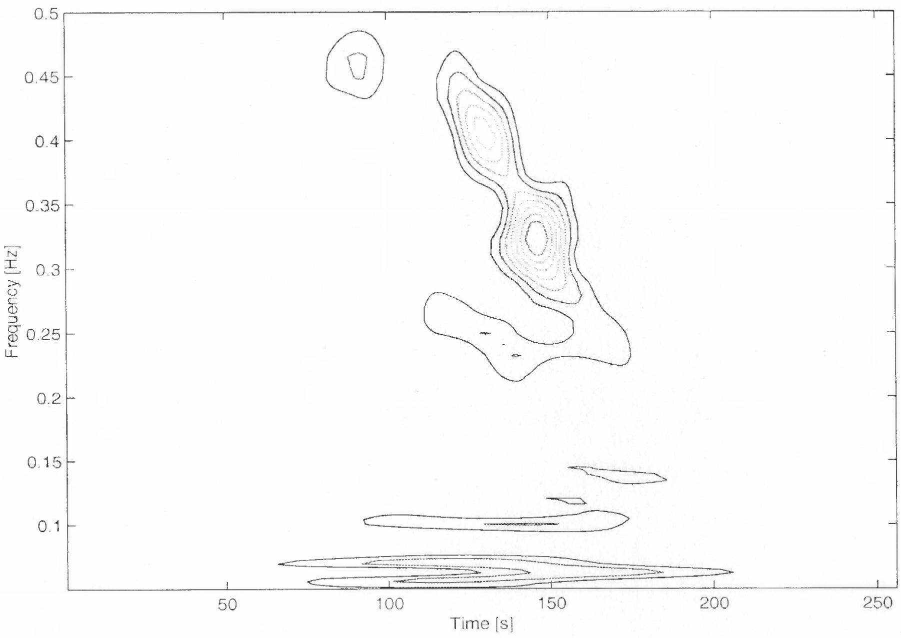

(a) Contour plot

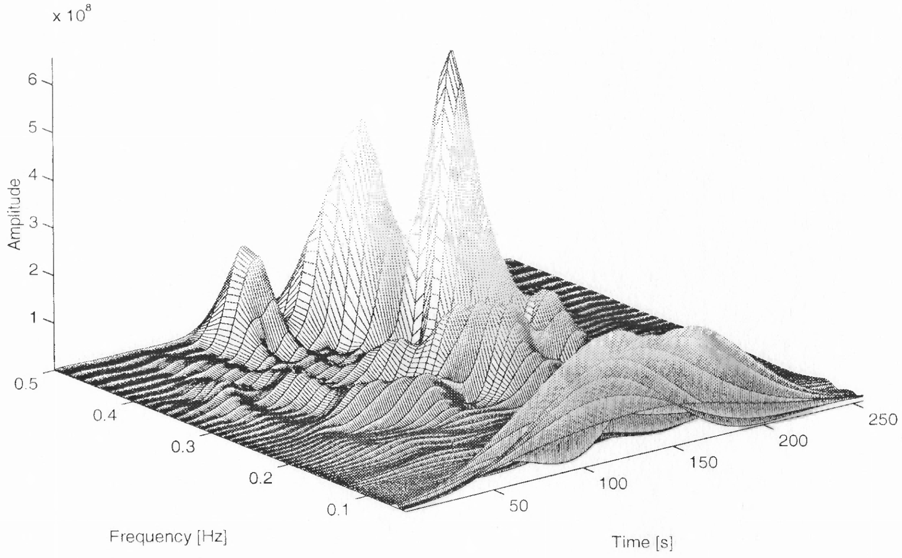

(b) Mesh plot

Figure 2.27 SAR image processed using the scalogram calculated in each case. In this scenario, the remaining signal was related to the moving target, or the original boat target. The masking technique is dependent on the various levels of the chirp signals and will not work in all scenarios. The transform window sizes are the same as in the examples of the previous section.

For the case of the WVD, the original target's relative velocity was not estimated due to the cross-terms found in the WVD. A contour plot for the output of the WVD is shown in Figure 2.28 and the cross-terms are clearly visible and do not allow the technique used to estimate the target parameters. For the case of the STFT, the target's relative velocity was estimated to be 7.2 meters/sec. The contour plot for the output in the case of the STFT is shown in Figure 2.29. In the case of the Gabor expansion, the target's relative velocity was estimated to be 6.5 meters/sec. The contour plot for the output in the case of the Gabor expansion is shown in Figure 2.30. Finally, for the case of the scalogram (CWT), the target's relative was estimated to be 5.2 meters/sec. The contour plot for the scalogram is shown in Figure 2.31.

As can be seen from the resulting estimated relative velocities, the numerical results from the successful techniques are similar to the examples previously discussed. This scenario demonstrates the property of linear transformation for the various time-frequency transformations used in this work.

In the SAR processing, various time-frequency analysis techniques have been used to analyze the track and determine the velocity of a moving target. Each of the techniques examined exhibited a sharp threshold effect in the input SNR required to estimate the instantaneous frequency (IF) of a simulated linear FM signal. The optimality of the Wigner-Ville distribution for the determination of the IF of a signal was verified by comparing the results of the simulation to the Cramer-Rao bound on the estimation of the IF. If the TF representation contains signal elements that do not allow certain types of processing, a 'mask' may successfully used to block certain

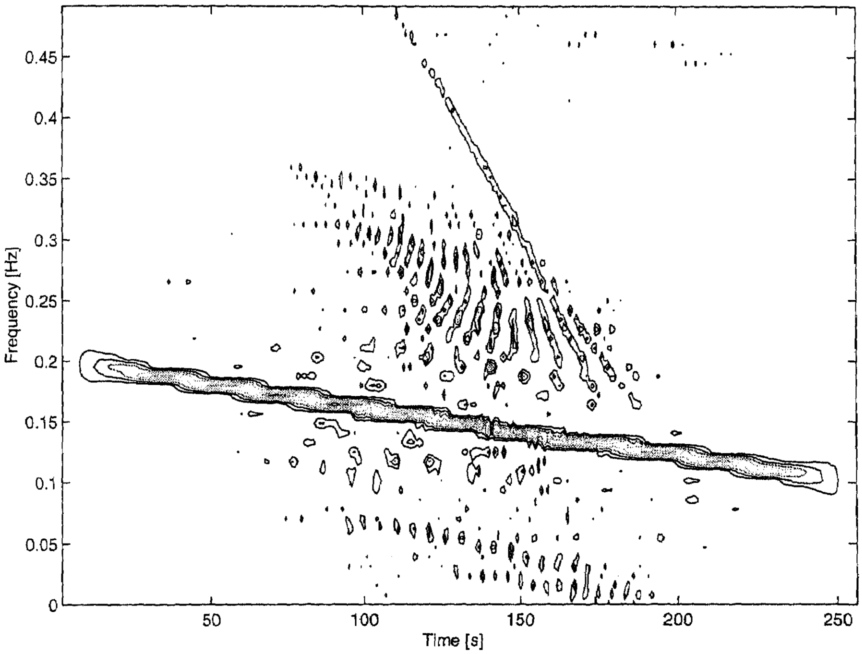

Figure 2.28 SAR with 2 moving targets processed using WVD

signal elements from the TF plane and allow the desired processing. With each TF processing technique, the relative velocity mismatch introduced by the motion of a single moving target (a boat) was less than 6% of the SAR platform velocity.

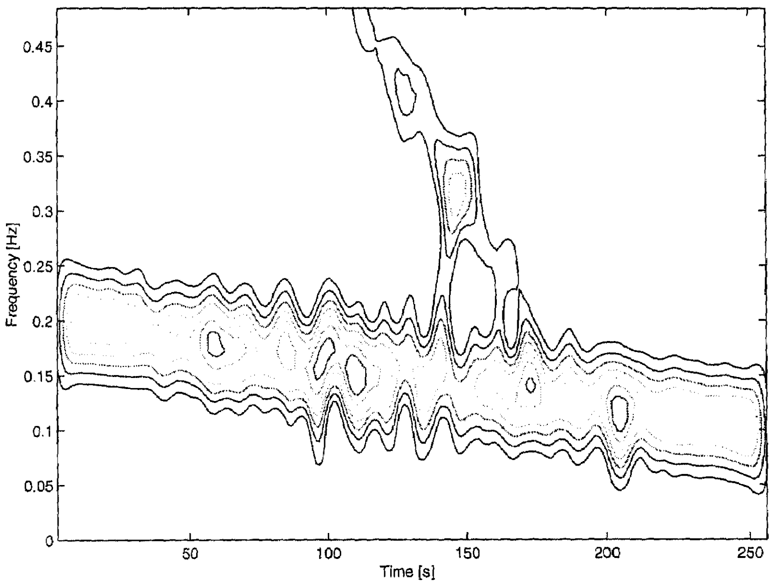

(a) Moving target with synthetic target added

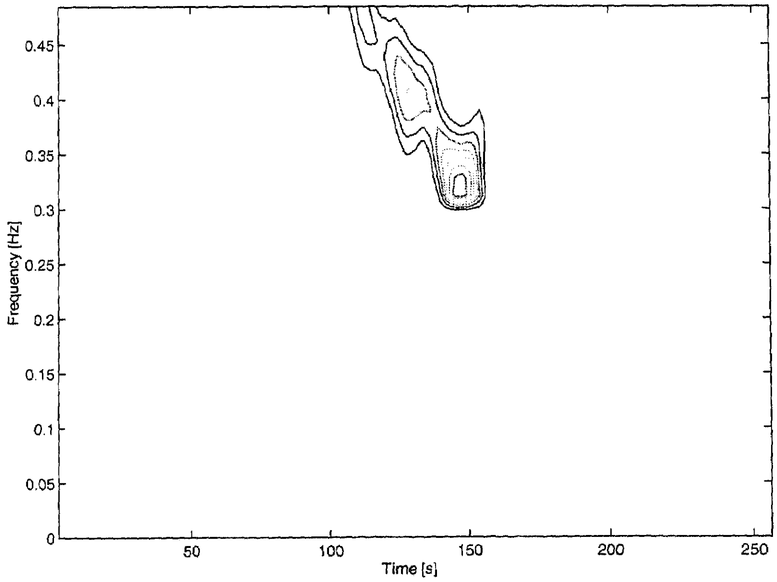

(b) Synthetic target removed

Figure 2.29 SAR with 2 moving targets processed using STFT

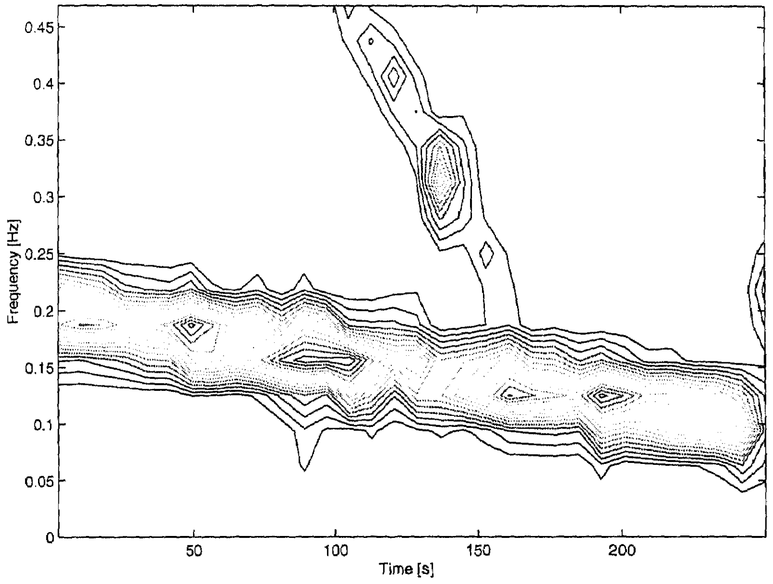

(a) Moving target with synthetic target added

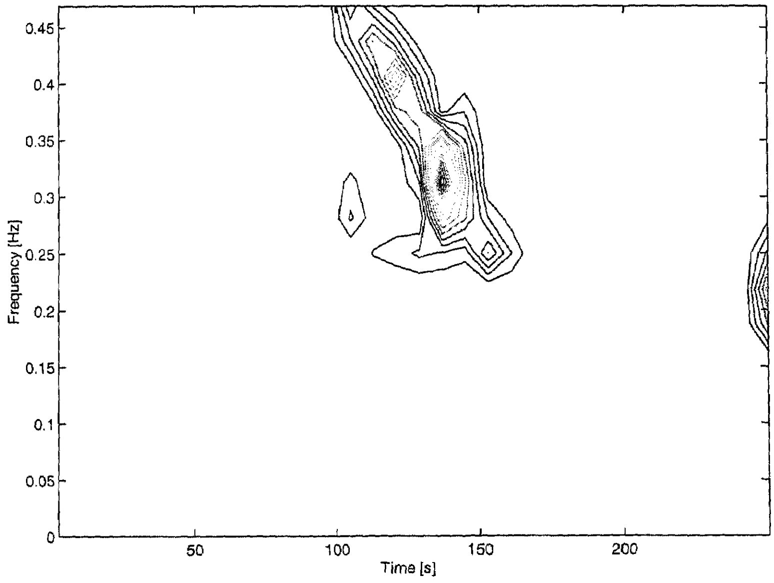

(b) Synthetic target removed

Figure 2.30 SAR with 2 moving targets processed using Gabor transform

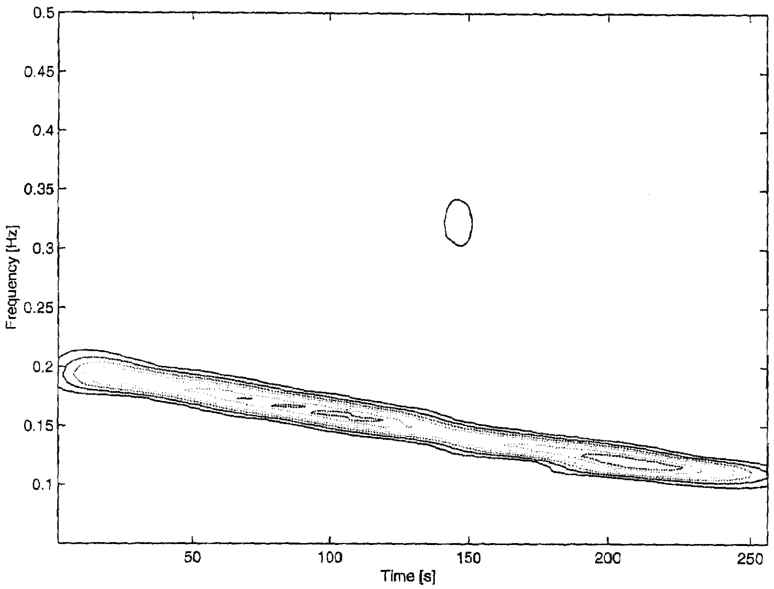

(a) Moving target with synthetic target added

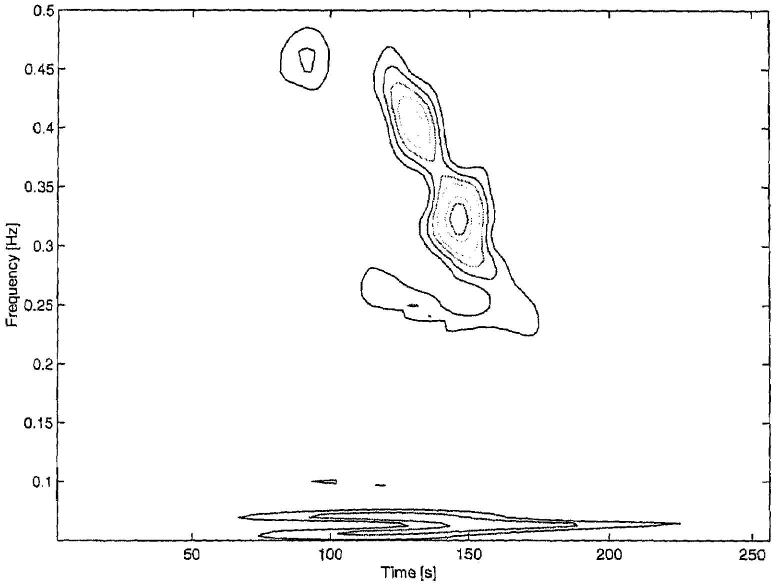

(b) Synthetic target removed

Figure 2.31 SAR with 2 moving targets processed using CWT

CHAPTER 3

SPACE-TIME ADAPTIVE PROCESSING SIGNAL ENVIRONMENT

This chapter serves as a brief review of related work. It also presents the definitions and mathematical model of the signals used throughout the remainder of the chapters. The Sample Matrix Inversion (SMI), Generalized sidelobe canceler (GSC), Eigencanceler, and fixed transforms are all introduced. Target cancellation occurs when the target signal is present during training, when the estimation of the noise covariance matrix occurs and also when there are calibration errors. Concepts related to this topic are also introduced.

3.1 Signal Model

Consider a space-time array with ν antennas uniformly spaced and a transmission of a coherent burst of κ pulses at a constant pulse repetition frequency (PRF). The time over which κ returns are collected is referred to as the coherent pulse interval (CPI) (Figure 3.1). Data is collected from a 3D data cube which consists of the antenna elements, pulses of the CPI, and range returns as shown in Figure 3.2. The determination as to whether a target is present at a range of interest is the goal of the signal processing. To that end, an $N = \nu \times \kappa$ snapshot consisting of the 2D data slice at the range of interest, is processed to yield a decision statistic, which subsequently is compared to a threshold. Processing is carried out in the N dimensional signal space resulting from stacking the snapshot column-wise. Radar detection is a binary hypothesis problem, where hypothesis $\mathbf{H}_0$ corresponds to target absence and $\mathbf{H}_1$ corresponds to target presence. Under hypothesis $\mathbf{H}_0$, the $N \times 1$ received vector $\mathbf{x}$ consists only of clutter $\mathbf{c}$ and noise $\mathbf{v}$ contributions:

$$\mathbf{x} = \mathbf{c} + \mathbf{v}, \tag{3.1}$$

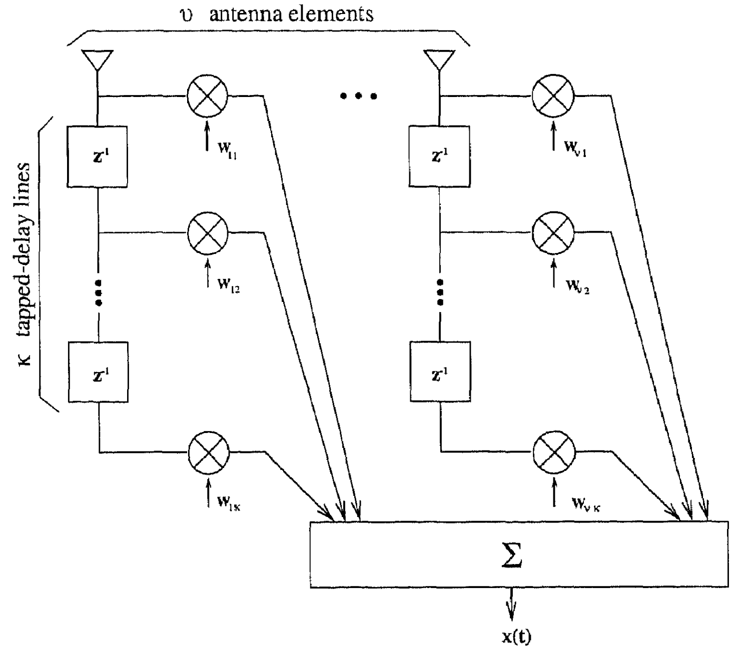

Figure 3.1 Space-time adaptive array architecture

where $\mathbf{x}$ is assumed a zero-mean, circularly symmetric Gaussian random vector with covariance matrix $\mathbf{R}$. The clutter and noise are assumed to be independent.

Under hypothesis $\mathbf{H}_1$, $\mathbf{x}$ is given by

$$\mathbf{x} = a\mathbf{s} + \mathbf{c} + \mathbf{v}, \tag{3.2}$$

where a is complex scalar representing the target signal amplitude and phase, and $\mathbf{s}$ is the target vector. The target power is denoted σ_s^2 .

The colored noise (the aggregate of noise+interference+clutter) covariance matrix $\mathbf{R} = E\left[(\mathbf{c}+\mathbf{v})(\mathbf{c}+\mathbf{v})^H\right]$, where the superscript denotes transpose and complex conjugate, is usually not known, hence an estimate is used instead. The estimate is derived from range cells in the vicinity of the tested range cell and is termed *secondary data*. The secondary data consists of clutter returns and, possibly, other interferences, such as jammers. The presence of narrowband jammers does not alter the signal model as presented, thus attention is restricted only to clutter

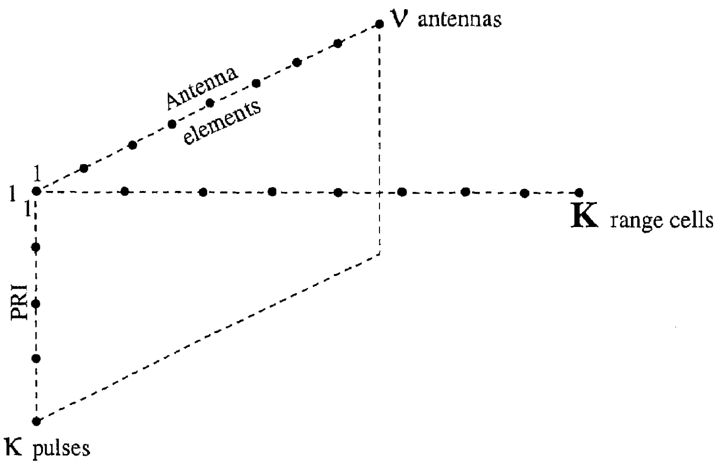

Figure 3.2 Space-time adaptive array datacube

signals. The assumption is that the secondary data $\mathbf{x}_k$, $k = 1, \ldots, K$, has the same statistical properties as the tested cell under hypothesis model $\mathbf{H}_0$.

The vector $\mathbf{x}_k$ is made up of N samples of the complex envelope of the received signal form a specific range gate k for $k = 1, \cdots, K$. Considering returns from all possible K range gates, the vector $\mathbf{x}_k$ makes up one 'slice' in the $\nu \times \kappa \times K$ data cube shown in Figure 3.2.

The basic airborne radar geometry is shown in Figure 3.3. Here, the assumptions are that the spatial channels are co-linear, identical, omni-directional and equally spaced with spacing $d = \lambda/2$. The components of $\mathbf{x}_k$ due to a clutter point source is written as

$$x_{st} = e^{2\pi(s-1)u} e^{2\pi(t-1)\mu} \qquad s = 1, \cdots, \nu, \quad t = 1, \cdots, \kappa \tag{3.3}$$

where u is the point source spatial frequency and μ is the normalized Doppler frequencies. These are given by

$$\begin{aligned} u &= \frac{d}{\lambda} sin\phi \; cos\theta \\ \nu &= \frac{2V}{\lambda} \mathrm{PRF} \; sin\phi \; cos\theta \end{aligned} \tag{3.4}$$

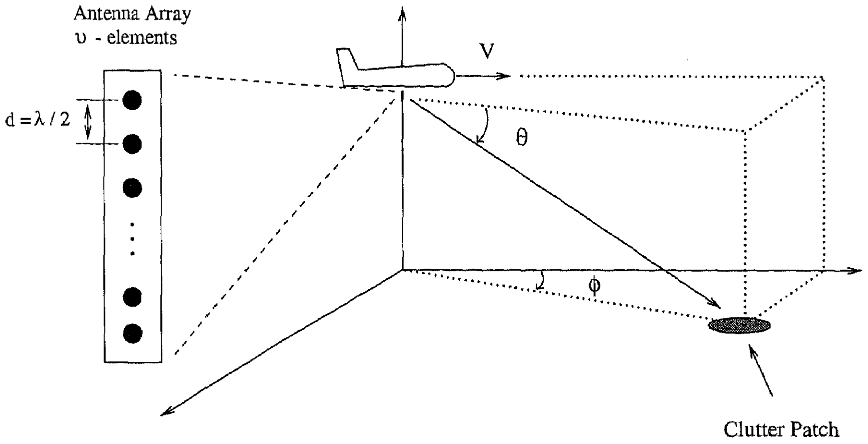

Figure 3.3 Airborne radar basic geometry

where d is the spacing between the antenna elements, ϕ is the point source azimuth angle, θ is the point source elevation angle, and V is relative speed of the point source as seen by the airborne radar.

The desired signal component of vector $\mathbf{x}_k$, under the same conditions, may be written

$$\mathbf{s} = \mathbf{s}_s \otimes \mathbf{s}_t \tag{3.5}$$

where $\otimes$ is the Kronecker product, $\mathbf{s}_s$ is a $\nu \times 1$ normalized spatial steering vector, and $\mathbf{s}_t$ is a $\kappa \times 1$ normalized temporal steering vector. The two vectors $\mathbf{s}_s$ and $\mathbf{s}_t$ are given by

$$\mathbf{s}_s = \begin{bmatrix} 1 \\ e^{j2\pi u_t} \\ \vdots \\ e^{j2\pi(\nu-1)u_t} \end{bmatrix} \tag{3.6}$$

and

$$\mathbf{s}_t = \begin{bmatrix} 1 \\ e^{j2\pi\mu_t} \\ \vdots \\ e^{j2\pi(\kappa-1)\mu t} \end{bmatrix} \tag{3.7}$$

where u_t and μ_t are the target's presumed spatial and normalized Doppler frequencies.

Since the colored noise true covariance matrix is usually not known a priori, a maximum likelihood estimate is obtained from a secondary data set from neighboring range cells around the cell under test. This estimate is referred to as the sample covariance matrix and is given as:

$$\widehat{\mathbf{R}} = \frac{1}{K}\sum_{k=1}^{K} \mathbf{x}_k \mathbf{x}_k^H . \tag{3.8}$$

This sample covariance matrix needs to be continually updated since the base environment may be considered stationary for only short periods of time.

The correlation matrix $\widehat{\mathbf{R}}$ can be decomposed into eigenvalues and eigenvectors using the spectral theorem,

$$\widehat{\mathbf{R}} = \sum_{l=1}^{L} \lambda_l \mathbf{q}_l \mathbf{q}_l^H , \tag{3.9}$$

where λ_l and $\mathbf{q}_l$ are the l^{th} eigenvalue and eigenvector, respectively. Eigenvalues are sorted from largest to smallest: $\lambda_1 > \lambda_2 > \cdots > \lambda_{L-1} > \lambda_L$. The inverse of the correlation matrix can be expresses in terms of the eigen-decomposition,

$$\widehat{\mathbf{R}}^{-1} = \sum_{l=1}^{L} \lambda_l^{-1} \mathbf{q}_l \mathbf{q}_l^H . \tag{3.10}$$

The eigenvectors are orthonormal,

$$\mathbf{q}_l^H \mathbf{q}_n = \begin{cases} 1 & l = n \\ 0 & l \neq n, \end{cases} \tag{3.11}$$

and form a complete set that spans an L-dimensional space:

$$\sum_{l=1}^{L} \mathbf{q}_l \mathbf{q}_l^H = \mathbf{I}. \tag{3.12}$$

The signal free covariance matrix is comprised of the interference and the noise contributions. If the covariance matrix is characterized by $r < L$ large eigenvalues then the r associated eigenvectors span the interference subspace. The matrix representation of the interference subspace is obtained by using the first r eigenvectors corresponding to the largest eigenvalues. The matrix representation of the noise subspace is formed using the remaining $L - r$ eigenvector. The two matrices are formed as follows:

$$\widehat{\mathbf{Q}}_r = \begin{bmatrix} \mathbf{q}_1 & \mathbf{q}_2 & \cdots & \mathbf{q}_r \end{bmatrix}, \qquad \text{and} \qquad \widehat{\mathbf{Q}}_v = \begin{bmatrix} \mathbf{q}_{r+1} & \mathbf{q}_{r+2} & \cdots & \mathbf{q}_L \end{bmatrix}. \quad (3.13)$$

The interference eigenvalues are used to form an $r \times r$ matrix, $\widehat{\mathbf{\Lambda}}_r$, and the noise eigenvalues are used to form an $(L - r) \times (L - r)$ matrix, $\widehat{\mathbf{\Lambda}}_v$, as follows:

$$\widehat{\mathbf{\Lambda}}_r = \begin{bmatrix} \lambda_1 & 0 & \cdots & 0 \\ 0 & \lambda_2 & \cdots & 0 \\ \vdots & \vdots & \ddots & \vdots \\ 0 & 0 & \cdots & \lambda_r \end{bmatrix} \qquad \text{and} \qquad \widehat{\mathbf{\Lambda}}_v = \begin{bmatrix} \lambda_{r+1} & 0 & \cdots & 0 \\ 0 & \lambda_{r+2} & \cdots & 0 \\ \vdots & \vdots & \ddots & \vdots \\ 0 & 0 & \cdots & \lambda_L \end{bmatrix}. \quad (3.14)$$

Using $\widehat{\mathbf{Q}}_r$, $\widehat{\mathbf{Q}}_v$, $\widehat{\mathbf{\Lambda}}_r$, and $\widehat{\mathbf{\Lambda}}_v$, the desired signal free $\widehat{\mathbf{R}}$ may be expressed

$$\widehat{\mathbf{R}} = \widehat{\mathbf{Q}}_r \widehat{\mathbf{\Lambda}}_r \widehat{\mathbf{Q}}_r^H + \widehat{\mathbf{Q}}_v \widehat{\mathbf{\Lambda}}_v \widehat{\mathbf{Q}}_v^H, \quad (3.15)$$

Equation 3.8 is an estimate of the true covariance matrix $\mathbf{R}$. For low rank interference, $\mathbf{R}$ can be decomposed into interference and white noise contributions as follows

$$\mathbf{R} = \mathbf{Q}_r \mathbf{\Lambda}_r \mathbf{Q}_r^H + \sigma^2 \mathbf{Q}_v \mathbf{Q}_v^H \quad (3.16)$$

where the diagonal of the $r \times r$ matrix $\mathbf{\Lambda}_r = \text{diag}\left(\lambda_1, \ldots, \lambda_r\right)$, $\lambda_1 \geq \lambda_2 \geq \ldots \geq \lambda_r$, consists of the r principal (largest) eigenvalues of $\mathbf{R}$, the columns of $\mathbf{Q}_r$ are the corresponding eigenvectors, σ^2 is the variance of the white noise, and the columns of $\mathbf{Q}_v$ are the remaining eigenvectors of $\mathbf{R}$. The actual value of r is scenario dependent, but it is upper bounded by $r \leq \nu + \kappa - 1$, for equidistant sampling in space and time and for a perfectly calibrated array [17]. The spectral decomposition of $\mathbf{R}$ in Equation 3.16 suggests a decomposition for the estimate $\widehat{\mathbf{R}}$ similar to Equation 3.15. The noise eigenvalues of the true covariance matrix in Equation 3.16 are all the same and given by the noise power σ_v^2. However, the noise eigenvalues obtained by decomposing the covariance matrix estimate $\widehat{\mathbf{R}}$ in Equation 3.15 are going to be spread over a range of power which depending on the sample support size used to estimate the covariance matrix. Noise exists at all frequencies and hence, an infinite number of degrees of freedom is needed to fully estimate the noise subspace. As the sample support size K increases, $\widehat{\mathbf{R}}$ approaches the true covariance matrix $\mathbf{R}$ and the noise eigenvalues in $\widehat{\Lambda}_v$ all converge towards the noise power σ^2.

3.2 Beamforming Techniques

A brief review of previous and related work in the field of adaptive processing of radar will now be presented.

3.2.1 Non-Adaptive Beamformer

The non-adaptive beamformer uses the weight vector

$$\mathbf{w}_{non} = \mathbf{s}, \tag{3.17}$$

where s is the presumed steering vector for the target. For a given angle and velocity, s has the form of Equation 3.6 or Equation 3.7. Amplitude tapering windowing functions maybe used on the steering vector to lower the sidelobes. When this is done, the width of the mainlobe is increased. The non-adaptive beamformer maximizes the beamformer's output signal-to-noise ratio in the absence of interferences.

3.2.2 Optimum Signal Processing

Brennan and Reed[46] with Mallet [15][47], developed the theory for optimum adaptive arrays which maximizes the probability of detection. It was shown that the optimal detector for a signal in Gaussian noise is achieved by using a Wiener filter when the covariance matrix of the signal is known a priori. The weights of this filter are given by

$$\mathbf{w} = k\mathbf{R}^{-1}\mathbf{s} \tag{3.18}$$

where k is a gain constant and $\mathbf{R}$ is the colored noise true covariance matrix. The Wiener filter can be interpreted as a cascade of a whitening filter for the interference, followed by a matched filter. This solution requires the knowledge of the true covariance matrix $\mathbf{R}$.

3.2.3 Sample Matrix Inversion

In practice, the true covariance matrix of the interference $\mathbf{R}$ is unknown a priori and needs to be estimated from a limited set of the secondary data (noise and interference) as given in Equation 3.8.

Substituting $\widehat{\mathbf{R}}$ for the true covariance matrix, $\mathbf{R}$, in Equation 3.18 yields the following solution

$$\mathbf{w} = k\widehat{\mathbf{R}}^{-1}\mathbf{s}. \tag{3.19}$$

The covariance matrix used for this solution has been estimated from a finite number of secondary samples. Therefore, this solution for the weights is not optimal.

The conditioned signal-to-colored noise ratio (CSNR) is defined as the ratio of the actual signal-to-colored noise ratio (SNR) to the optimal SNR. The optimal SNR results when the covariance is known. Colored noise refers to the white noise and interference. If $K \approx 2N$ snapshots are used to estimate $\widehat{\mathbf{R}}$ in Equation 3.8, Reed et al.[15] showed that this solution in Equation 3.19 achieves a CSNR at the output of the array with a mean of 0.5. A 3 dB loss with respect to the optimal SNR is a CSNR with a mean of 0.5. The CSNR is a random variable bounded between 0 and 1 because the covariance matrix is estimated using Equation 3.8 and the resulting signal-to-noise ratio is a random variable.

3.2.4 Generalized Sidelobe Canceller (GSC)

The Generalized sidelobe canceller (GSC) is a general form of a linearly constrained adaptive beamforming algorithm[48]. It adapts to minimize mean square error (MSE)

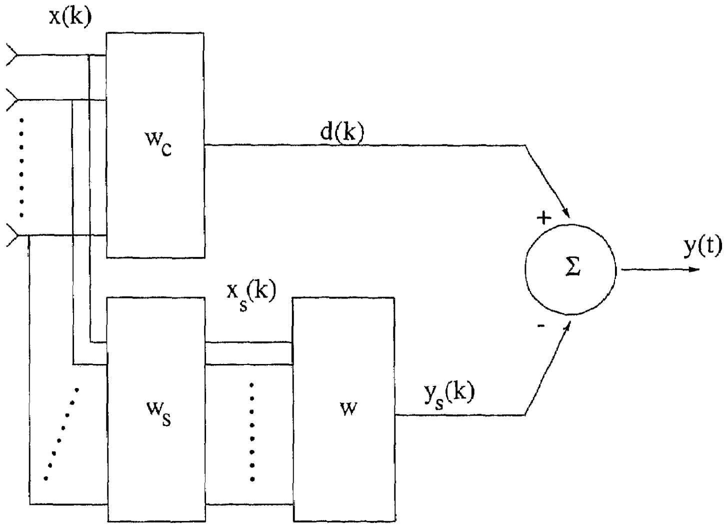

Figure 3.4 Full-rank GSC processor

in a system while implementing a look direction constant gain constraint[49]. The GSC is implemented by partitioning the received signal with filters $\mathbf{w}_c$ and $\mathbf{W}_s$ as shown in Figure 3.4. This $Kx1$ beamforming filter takes the form

$$\mathbf{w}_c = (1/K)\mathbf{1}, \tag{3.20}$$

where $\mathbf{1}$ is a vector whose elements are all 1. The desired signal is blocked from the adaptive processor by $\mathbf{W}_s$, the $N \times K$ signal blocking matrix, with $N < K$. The full row rank matrix $\mathbf{W}_s$ is made up of rows $\mathbf{a}_i$ where $\mathbf{a}_i\mathbf{1} = 0$ for $i = 1, 2, \cdots, K$.

The $K \times 1$ dimensional received signal vector at time k is represented by $\mathbf{x}(k)$. The input $K \times K$ covariance matrix is denoted by $\mathbf{R}_x = E[\mathbf{x}(k)\mathbf{x}^H(k)]$. The N dimensional noise subspace is given by,

$$\mathbf{x}_s(k) = \mathbf{W}_s\mathbf{x}(k). \tag{3.21}$$

The scalar beamformed output is

$$d(k) = \mathbf{w}_c^H\mathbf{x}(k). \tag{3.22}$$

The scalar beamformed noise estimator is

$$y_s(k) = \mathbf{w}^H \mathbf{x}_s(k) \tag{3.23}$$

where $\mathbf{w}$ is the N dimensional weight vector. The array output is

$$y(k) = (\mathbf{w}_c^H - \mathbf{w}^H \mathbf{W}_s)\mathbf{w}(k). \tag{3.24}$$

3.2.5 Eigencanceler

The sample covariance matrix may be decomposed into two orthogonal subspaces denoting the interference subspace, $\widehat{\mathbf{Q}}_r$, and the noise subspace, $\widehat{\mathbf{Q}}_v$. This is shown in Equation 3.15. The eigencanceler selects its weight vector to lie in the noise subspace as this space is orthogonal to the interference subspace. It is shown in [17] that the weight vector is written as

$$\begin{aligned} \mathbf{w} &= k\left(\mathbf{I} - \widehat{\mathbf{Q}}_r \widehat{\mathbf{Q}}_r^H\right)\mathbf{s} \\ &= k\widehat{\mathbf{Q}}_v \widehat{\mathbf{Q}}_v^H \mathbf{s} \end{aligned} \tag{3.25}$$

where k is a complex constant and $\mathbf{I}$ is the identity matrix of dimension N.

Using the Eigencanceler to select the weight vector produces higher values of the signal-to-noise ratio compared to the SMI. The Eigencanceler requires only $K \approx 2r$ samples to obtain the sample covariance matrix and achieve a signal-to-noise ratio within 3 dB of the optimal.

3.2.6 Fixed Transforms

A technique based on a fixed transformation is also used with maximum-likelihood adaptive nulling[15]. The basis of this technique is 'Two-Step Nulling' by Marshall [50]. In this technique, the steering vector and sample covariance matrix are transformed to a new domain using a fixed transform $\mathbf{T}$,

$$\hat{\mathbf{x}} = \mathbf{T}^H \mathbf{x},$$

$$\begin{aligned} \hat{\mathbf{s}} &= \mathbf{T}^H\mathbf{s}, \\ \hat{\mathbf{R}} &= \mathbf{T}^H\mathbf{R}, \end{aligned} \tag{3.26}$$

where $\mathbf{x}$ is the data vector, $\mathbf{s}$ is the steering vector, and $\mathbf{R}$ is the covariance matrix.

To use the technique with a fixed transform such as the discrete Fourier transform (from Equation 2.4) or the discrete Cosine transform (Appendix A), the K terms in the transform are selected based on the amount of 'energy' associated with each index. This is done by computing a 2-dimensional stacked transform (Appendix B) $\mathbf{S}_T$ and calculating the N terms

$$\mid \mathbf{S}_T(n)'\widehat{\mathbf{R}}\mathbf{S}_T(n) \mid . \tag{3.27}$$

The columns of $\mathbf{S}_T$ terms associated with the largest K results of this calculations are defined as $\mathbf{T}_2$. Finally, the transform matrix $\mathbf{T}$ is defined as

$$\mathbf{T} = [\mathbf{s}\mathbf{T}_2]. \tag{3.28}$$

The inclusion of $\mathbf{s}$ within the transform matrix constrains the system so that $\mathbf{T}^H\mathbf{s} \neq 0$.

3.3 Target Cancellation

Target cancellation occurs when the target signal is present during training, when the estimation of the noise covariance matrix occurs and also when there are calibration errors. In the case of the steering vector being mismatched to the signal vector, the array cancels the target as it is interpreted as an interference. If the true covariance matrix is know, the signal cancellation may be isolated from the noise covariance matrix estimation effects. This case may be shown to be true when the weight vector is applied to the data it was derived from.

The correlation matrix of a N element spatial processor with a single interferer and a single target is

$$\widehat{\mathbf{R}} = \sigma_d^2\mathbf{s}_d\mathbf{s}_d^H + \sigma_i^2\mathbf{s}_i\mathbf{s}_i^H + \sigma_n^2/N\mathbf{I}, \tag{3.29}$$

where σ_d^2, σ_d^2, σ_n^2 are the desired signal, interference, and noise power and $\mathbf{s}_d$ and $\mathbf{s}_i$ are the desired signal and interference vector, respectively. The normalized presumed steering vector is in the form

$$\mathbf{s}_m = \sqrt{1/N}\begin{bmatrix}1 & e^{\jmath 2\pi\psi_m} & \cdots & e^{\jmath 2\pi(N-1)\psi_m}\end{bmatrix}^T, \tag{3.30}$$

where ψ_m is the normalized spatial frequency, related to the presumed target angle, θ_m, by $\psi_m = d\sin\theta_m/\lambda$ where λ is the wavelength of the transmitted signal and d is the distance between antenna elements. The normalized desired signal vector is in the form

$$\mathbf{s}_d = \frac{1}{\mid \mathbf{c} \mid}\begin{bmatrix}c_0 & c_1 e^{\jmath 2\pi\psi_d} & \cdots c_{N-1} e^{\jmath 2\pi(N-1)\psi_d}\end{bmatrix}^T \tag{3.31}$$

and

$$\mathbf{c} = \begin{bmatrix}c_0 & c_1 & \cdots & c_{N-1}\end{bmatrix}^T \tag{3.32}$$

where $\mathbf{c}$ is a complex random variable with Gaussian distributed magnitude and phase. The calibration error is modeled by the vector $\mathbf{c}$. The magnitude and phase have small variances in the case of good calibration. The mean of the amplitude is $\sqrt{1/N}$ and the mean of the phase errors is zero. The pointing error is the difference between the true angle and the presumed angle, $\theta_m - \theta_d$. With no calibration or pointing errors, the desired signal vector will equal the presumed steering vector. The interference signal goes through the same channels as the desired signal, so the normalized interference vector may be written as

$$\mathbf{s}_i = \frac{1}{\mid \mathbf{c} \mid}\begin{bmatrix}c_0 & c_1 e^{\jmath 2\pi\psi_i} & \cdots & c_{N-1} e^{\jmath 2\pi(N-1)\psi_i}\end{bmatrix}^T, \tag{3.33}$$

where ψ_i is the normalized spatial frequency of the interference. The array gain, defined as the ratio of the SNIR at the output of the beamformer to the SNR at the input may be used to compare the performance of adaptive beamformers. The array gain, as a function of the weight vector, is

$$G_w = \frac{\mid \mathbf{w}^H \mathbf{s}_d \mid^2}{INR\mathbf{w}^H \mathbf{s}_i \mathbf{s}_i^H \mathbf{w} + 1/N\mathbf{w}^H \mathbf{w}} \tag{3.34}$$

where $INR = \sigma_i^2/\sigma_n^2$.

The effects of array imperfections may be examined by plotting the array gain (Equation 3.34) as a function of the pointing error related to the SNR and the standard deviation of the phase errors. Details of the analysis for the SMI and eigencanceler may be found in [51, 52]. For the spatial case when the interference vector is orthogonal to the target, $\mathbf{s}_i^H\mathbf{s}_d = 0$ and only the pointing error is considered, $(\mathbf{c}_i = \sqrt{1/N})$, the array gain for the SMI is given by

$$G_{smi} = \frac{|\rho_1|^2 (1-\gamma_s)^2}{1-\gamma_s(2-\gamma_s)\,|\rho_1|^2 - \gamma_i(2-\gamma_i)\,|\rho_2|^2} \tag{3.35}$$

where $\rho_1 = \mathbf{s}_m^H\mathbf{s}_d, \rho_2 = \mathbf{s}_m^H\mathbf{s}_i, \gamma_s = SNR/(1+SNR)$, and $\gamma_i = INR/(1+INR)$ and $0 \le \gamma_s, \gamma_i \le 1$. G_{smi} degrades as SNR increases. For the eigencanceler, the array gain is

$$G_{eig} = \frac{|\rho_1|^2}{1-|\rho_2|^2} \tag{3.36}$$

From Equations 3.35 and 3.36 it can be seen that $G_{smi} \le G_{eig}$ with equality for $\gamma_s = 0$ and $\gamma_i = 1$. Therefore, the eigencanceler is less affected by pointing errors that the SMI method.

The array gain (Equation 3.34) may be expressed for the reduced rank methods based on fixed transforms (Equation 3.26).

$$G_{fixed} = \frac{|\hat{\mathbf{w}}^H\hat{\mathbf{s}}_d|^2}{INR\hat{\mathbf{w}}^H\hat{\mathbf{s}}_i\hat{\mathbf{s}}_i^H\hat{\mathbf{w}} + 1/N\hat{\mathbf{w}}^H\hat{\mathbf{w}}} \tag{3.37}$$

where $\hat{\mathbf{w}} = \hat{\mathbf{R}}^{-1}\hat{\mathbf{s}}$, the weight vector in the transform domain.

CHAPTER 4

REDUCED-RANK PROCESSING

The signal model presented in the previous chapter suggests that STAP could benefit from the application of reduced-rank (RR) methods. Such methods incur a loss in the SNR, but their main advantage lies in their statistical stability. In this chapter, the term SNR is defined as the signal-to-noise and interference ratio. First considered are RR methods with known covariance matrix, subsequently RR performance with unknown covariance is analyzed. The analysis is carried out in the frameworks of the minimum variance beamformer (MVB) and the generalized sidelobe canceller (GSC) processors. Calibration errors are known to affect the performance of adaptive arrays. A method of studying these errors is also presented.

4.1 Reduced-Rank Processing with Known Covariance

A diagram of the reduced-rank MVB is shown in Figure 4.1. The full-rank MVB weight vector is obtained as a solution to the optimization problem:

$$\min \ \mathbf{w}^H\mathbf{R}\mathbf{w} \qquad \text{subject to} \qquad \mathbf{s}^H\mathbf{w} = 1, \tag{4.1}$$

where $\mathbf{R} = E\left[\mathbf{x}_k\mathbf{x}_k^H\right]$, $\mathbf{x}_k$ are snapshots of the secondary data, and $\mathbf{s}$ is the steering vector. With RR-MVB, the vector $\mathbf{x}_k$ is pre-processed by a full column rank $N \times r$ matrix transformation $\mathbf{T}$. The RR data is then the $r \times 1$ vector $\mathbf{z}_k = \mathbf{T}^H\mathbf{x}_k$, the RR covariance matrix is $\mathbf{T}^H\mathbf{R}\mathbf{T}$, and the RR steering vector is $\mathbf{t} = \mathbf{T}^H\mathbf{s}$. The RR-MVB weight vector is given by

$$\mathbf{w} = k\left(\mathbf{T}^H\mathbf{R}\mathbf{T}\right)^{-1}\mathbf{T}^H\mathbf{s}, \tag{4.2}$$

where k is a scalar chosen to satisfy the unit gain constraint in the direction of the desired signal. Notice that the value of k does not affect the output signal-to-interference plus noise ratio (SINR). The output SINR may be written as

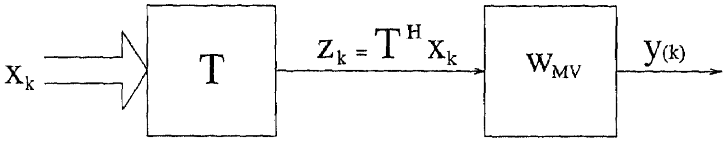

Figure 4.1 Reduced-rank MVB

$\mu = | \mathbf{w}^H \mathbf{s} |^2 / \mathbf{w}^H \mathbf{R} \mathbf{w}$. Inserting the expression for the RR-MVB weight vector, the output SINR is given by

$$\mu = \mathbf{s}^H \mathbf{T} \left(\mathbf{T}^H \mathbf{R} \mathbf{T} \right)^{-1} \mathbf{T}^H \mathbf{s}, \tag{4.3}$$

where for notational convenience it is assumed that the target power is unity, $\sigma_s^2 = 1$.

The reduced-rank GSC is shown in Figure 4.2. From the figure it is observed that the output can be expressed

$$y = y_c(k) - y_a(k) = \mathbf{w}_c^H \mathbf{x}_k - \mathbf{w}_a^H \mathbf{U}^H \mathbf{A} \mathbf{x}_k, \tag{4.4}$$

where $\mathbf{w}_c$, the weight vector of the nonadaptive portion, is just the steering vector $\mathbf{w}_c = \mathbf{s}$, $\mathbf{w}_a$ is the adaptive weight, the matrix $\mathbf{U}$ is a full column rank transformation, and $\mathbf{A}$ is a transformation that blocks the look direction, $\mathbf{A}\mathbf{s} = 0$. Assuming that $\mathbf{A}$ has full column rank, and that $\mathbf{s}$ is the only vector in the null space of $\mathbf{A}$, the dimensions of $\mathbf{A}$ are $(N-1) \times N$. Consequently, the rank reducing matrix $\mathbf{U}$ is $(N-1) \times r$. Multiple linear constraints can be incorporated in $\mathbf{A}$ resulting in a null space of dimension equal to the number of constraints. The equivalent GSC weight vector can be written as

$$\mathbf{w} = \mathbf{w}_c - \mathbf{A}^H \mathbf{U} \mathbf{w}_a. \tag{4.5}$$

The vector $\mathbf{w}_a$ is found as the solution to the unconstrained optimization problem

$$\min_{\mathbf{w}_a} \left(\mathbf{s} - \mathbf{A}^H \mathbf{U} \mathbf{w}_a \right)^H \mathbf{R} \left(\mathbf{s} - \mathbf{A}^H \mathbf{U} \mathbf{w}_a \right). \tag{4.6}$$

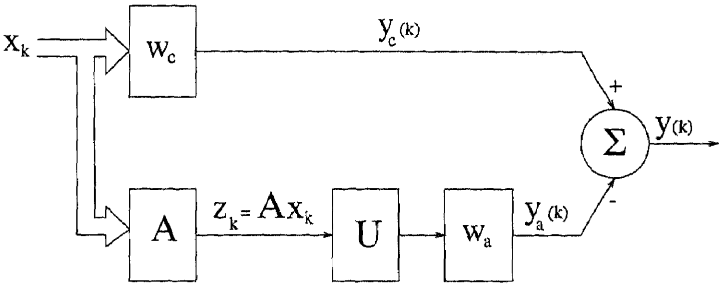

Figure 4.2 Reduced-rank GSC

This minimization results in

$$\mathbf{w}_a = \left(\mathbf{U}^H\mathbf{A}\mathbf{R}\mathbf{A}^H\mathbf{U}\right)^{-1}\mathbf{U}^H\mathbf{A}\mathbf{R}\mathbf{s}. \tag{4.7}$$

Using Equations 4.4 and 4.7, the overall GSC weight vector is then given by

$$\mathbf{w} = \left(\mathbf{I}_N - \mathbf{A}^H\mathbf{U}\left(\mathbf{U}^H\mathbf{A}\mathbf{R}\mathbf{A}^H\mathbf{U}\right)^{-1}\mathbf{U}^H\mathbf{A}\mathbf{R}\right)\mathbf{s}, \tag{4.8}$$

where $\mathbf{I}_N$ is the N-dimensional identity matrix. The output SINR (when target power $\sigma_s^2 = 1$) is given by [53]

$$\mu = \left(\mathbf{s}^H\mathbf{R}\mathbf{s} - \mathbf{s}^H\mathbf{R}\mathbf{A}^H\mathbf{U}\left(\mathbf{U}^H\mathbf{A}\mathbf{R}\mathbf{A}^H\mathbf{U}\right)^{-1}\mathbf{U}^H\mathbf{A}\mathbf{R}\mathbf{s}\right)^{-1} \tag{4.9}$$

Various choices of the rank reducing transformation $\mathbf{U}$ are now considered:

1. One such choice could be

$$\mathbf{A}^H\mathbf{U} = \mathbf{Q}_r, \tag{4.10}$$

where $\mathbf{Q}_r$ consists of the r largest eigenvectors of $\mathbf{R}$. Assuming that the $(N-1) \times N$ signal blocking matrix $\mathbf{A}$ has full column rank, the elements of $\mathbf{U}$ can be obtained from the solution of a least-squares problem. It is easy to show that with this choice of $\mathbf{U}$:

$$\begin{aligned}\mu &= \left(\mathbf{s}^H\mathbf{R}\mathbf{s} - \mathbf{s}^H\mathbf{Q}_r\Lambda_r\mathbf{Q}_r^H\mathbf{s}\right)^{-1} \\ &= (\mathbf{s}^H\mathbf{Q}_v\Lambda_v\mathbf{Q}_v^H\mathbf{s})^{-1}.\end{aligned} \tag{4.11}$$

2. To avoid the complication of a least-squares problem, let the matrix $\mathbf{U}$ be restricted to consist of r of the $(N-1)$ eigenvectors of $\mathbf{R}_a = \mathbf{ARA}$, where $\mathbf{R}_a = \overline{\mathbf{Q}}_r \overline{\Lambda}_r \overline{\mathbf{Q}}_r^H + \overline{\mathbf{Q}}_v \overline{\Lambda}_v \overline{\mathbf{Q}}_v^H$, and $rank\left(\overline{\mathbf{Q}}_r\right) = r$. A natural choice would be to let the rank reducing transformation consist of the r principal eigenvectors of $\mathbf{R}_a$, i.e., $\mathbf{U} = \overline{\mathbf{Q}}_r$.

3. For a known covariance matrix $\mathbf{R}$, an optimal approach that maximizes the output SINR for a given rank r, is suggested in [21, 22]: construct $\mathbf{U}$ from the r eigenvectors of $\mathbf{R}_a$ that maximize the quantity
$$\frac{\left|\overline{\mathbf{q}}_i^H \mathbf{ARs}\right|^2}{\overline{\lambda}_i}, \tag{4.12}$$
where $\overline{\mathbf{q}}_i$, $\overline{\lambda}_i$ are respectively eigenvectors and eigenvalues of $\mathbf{R}_a$. In the references, this method is referred as the *cross-spectral metric* (CSM) method.

4. Principal components decomposition, such as considered above, is data dependent. Fixed, reduced-rank transformations can be constructed by selecting the principal components of the discrete Fourier transform (DFT) or the discrete cosine transform (DCT). The cross spectral metric can also be used in conjunction with these fixed transforms [21, 22].

Next, rank-reducing transformations are evaluated in the MVB framework. Consider the SINR at the MVB output, as given by Equation 4.3. When the transformation $\mathbf{T}$ is unitary, it has no effect on the output SINR, and $\mu = \mathbf{s}^H\mathbf{R}^{-1}\mathbf{s} = \mu_{\max}$. For any $N \times r$ rank reducing transformation $\mathbf{T}$, $r < N$, $\mu = \mathbf{s}^H\mathbf{T}\left(\mathbf{T}^H\mathbf{RT}\right)^{-1}\mathbf{T}^H\mathbf{s} < \mu_{\max}$. Specific examples are considered below.

1. Consider how *Case 1* of the GSC translates to the MVB framework. By substituting Equation 4.10 in 4.8, we obtain the equivalent MVB weight vector
$$\mathbf{w} = \left(\mathbf{I}_N - \mathbf{Q}_r\mathbf{Q}_r^H\right)\mathbf{s}. \tag{4.13}$$

This relation establishes an equivalence between the reduced-rank GSC and the eigencanceler [17]. The eigencanceler is a method that produces the minimum norm weight vector meeting the set of linear constraints, and subject to the additional constraint of orthogonality to the interference subspace (formed by the principal eigenvectors of the space-time covariance matrix). Since $\mathbf{Q}_v\mathbf{Q}_v^H = \mathbf{I}_N - \mathbf{Q}_r\mathbf{Q}_r^H$, the eigencanceler is equivalent to the application of a rank reducing transformation $\mathbf{T} = \mathbf{Q}_v$, where the columns of $\mathbf{Q}_v$ span the noise subspace of the covariance $\mathbf{R}$. Indeed, Equation 4.13 is obtained by using $\mathbf{T} = \mathbf{Q}_v$ and substituting Equation 3.16 in Equation 4.2. The eigencanceler is useful when there is a sizable projection $\mathbf{Q}_v^H\mathbf{s}$. The output SINR is given by

$$\begin{aligned} \mu &= \mathbf{s}^H\mathbf{Q}_v\left(\mathbf{Q}_v^H\mathbf{R}\mathbf{Q}_v\right)^{-1}\mathbf{Q}_v^H\mathbf{s} \\ &= \mathbf{s}^H\mathbf{Q}_v\mathbf{\Lambda}_v^{-1}\mathbf{Q}_v^H\mathbf{s} \\ &< \mu_{\max}, \end{aligned} \tag{4.14}$$

where

$$\mu_{\max} = \mathbf{s}^H\mathbf{Q}_r\mathbf{\Lambda}_r^{-1}\mathbf{Q}_r^H\mathbf{s} + \mathbf{s}^H\mathbf{Q}_v\mathbf{\Lambda}_v^{-1}\mathbf{Q}_v^H\mathbf{s}. \tag{4.15}$$

2. The $N \times r$ matrix is given by $\mathbf{T} = \mathbf{Q}_r$, i.e., it consists of the r principal components of the signal-plus-interference subspace [18]. In this case $\mathbf{T}$ consists of the principal components of the Karhunen-Loeve transform. The output SINR is given by $\mu = \mathbf{s}^H\mathbf{Q}_r\mathbf{\Lambda}_r^{-1}\mathbf{Q}_r^H\mathbf{s}$. Note that if the look direction is in the noise subspace of the transform $\mathbf{T}$, i.e., $\mathbf{T}^H\mathbf{s} = 0$, there is no solution that directly solves Equation 4.2. This problem is circumvented in [50] by the augmentation of $\mathbf{T}$ with the vector $\mathbf{s}$, $[\mathbf{T}, \mathbf{s}] \rightarrow \mathbf{T}$.

3. The columns of $\mathbf{T}$ may be designed using the cross-spectral metric approach.

4. Similar to *Case 4* of the GSC, the rank reducing transformation $\mathbf{T}$ may be constructed from the principal components of a fixed transform such as the DFT or the DCT.

To reiterate, when the true covariance matrix $\mathbf{R}$ is known, reduced-rank processing is suboptimal. The strength of reduced-rank methods is revealed for unknown covariance. This case is considered in the next section.

4.2 Reduced-Rank Processing with Unknown Covariance

In practice, the space-time covariance matrix is not known and it needs to be estimated from the secondary data. This is an application for which reduced rank methods can take advantage of their improved statistical stability. Let the number of snapshots from the secondary dataset (sample support) be equal to K. Then the estimated covariance matrix is given by $\widehat{\mathbf{R}} = \frac{1}{K}\sum_{k=1}^{K} \mathbf{x}_k \mathbf{x}_k^H$. In this section, the performance of reduced-rank processors is analyzed as a function of the sample support K.

A widely accepted measure of performance for radar systems is the probability of detection. In adaptive radar, detection probability is a function of the weight vector. Likewise, the weight vector is derived from estimates of the covariance matrix of the secondary data, and as such, its elements are random variables. This makes the detection probability dependent on the outcome of the sample covariance matrix. Insight can be gained by expressing detection probability as a function of the *conditioned SNR* (CSNR). The CSNR is defined as the effective SINR obtained by the application of a particular method, normalized by the optimal SINR (known covariance matrix, full-rank case):

$$\rho = \frac{\mathrm{SINR}_{\mathrm{eff}}}{\mathrm{SINR}_{\mathrm{opt}}}. \tag{4.16}$$

The conditioned SNR is a random variable, always bounded $0 \leq \rho \leq 1$. For a target signal amplitude of a and an array weight vector of $\mathbf{w}$, the effective SINR at the output is given by $\mathrm{SINR}_{\mathrm{eff}} = |a|^2 \left|\mathbf{w}^H \mathbf{s}\right|^2 / \mathbf{w}^H \mathbf{R} \mathbf{w}$. The optimal SINR is given by $\mathrm{SINR}_{\mathrm{opt}} = |a|^2 \mathbf{s}^H \mathbf{R}^{-1} \mathbf{s}$. It follows that for a particular method, the CSNR can be computed from

$$\rho = \frac{\left|\mathbf{w}^H \mathbf{s}\right|^2}{\mathbf{w}^H \mathbf{R} \mathbf{w}} \frac{1}{\mathbf{s}^H \mathbf{R}^{-1} \mathbf{s}}. \tag{4.17}$$

Several specific methods are considered below. With SMI, the full-rank MVB weight vector is given by $\mathbf{w} = \widehat{\mathbf{R}}^{-1} \mathbf{s}$. The density of the CSNR for the SMI method with Gaussian data has been derived in [15], and is given by the beta distribution with parameters K and N,

$$f_\rho(\rho) = \frac{\Gamma(K+1)}{\Gamma(N-1)\,\Gamma(K+2-N)} (1-\rho)^{N-2} \rho^{K+1-N}, \tag{4.18}$$

where $\Gamma(K) = (K-1)!$ is the standard gamma function. When a rank r, $r \leq N$, transformation $\mathbf{T}$ is applied to the data, the CSNR can be written:

$$\rho = \frac{\left(\mathbf{t}^H \widehat{\mathbf{\Sigma}}^{-1} \mathbf{t}\right)^2}{\mathbf{t}^H \widehat{\mathbf{\Sigma}}^{-1} \mathbf{\Sigma} \widehat{\mathbf{\Sigma}}^{-1} \mathbf{t}} \frac{1}{\mathbf{s}^H \mathbf{R}^{-1} \mathbf{s}}, \tag{4.19}$$

where $\mathbf{t} = \mathbf{T}^H \mathbf{s}$ is an $r \times 1$ vector, and $\mathbf{\Sigma} = \mathbf{T}^H \mathbf{R} \mathbf{T}$, $\widehat{\mathbf{\Sigma}} = \mathbf{T}^H \widehat{\mathbf{R}} \mathbf{T}$ are $r \times r$ matrices. To allow for adaptation away from the interference subspace, the rank of the transformation $\mathbf{T}$ needs to be $r \geq p+1$, where p is the rank of the interference subspace.

The distribution of ρ for various reduced-rank methods will now be determined. Two classes of transformations are distinguished: (1) the class of fixed transformations, and (2) the class of data dependent transformations. The former applies when $\mathbf{T}$ is formed from data independent transformations such as the DFT or the DCT. To the latter class belong data dependent transformations $\mathbf{T}$ such as formed by the eigenvectors of the estimated covariance $\widehat{\mathbf{R}}$. The CSNR for each of these classes is subsequently analyzed.

4.2.1 Analysis of Fixed Transforms

For fixed $\mathbf{T}$, Equation 4.19 can be rewritten:

$$\rho = \rho_b \rho_r, \tag{4.20}$$

where ρ_r is the reduced-rank CSNR,

$$\rho_r = \frac{\left(\mathbf{t}^H \hat{\Sigma}^{-1} \mathbf{t}\right)^2}{\mathbf{t}^H \hat{\Sigma}^{-1} \Sigma \hat{\Sigma}^{-1} \mathbf{t}} \frac{1}{\mathbf{t}^H \Sigma^{-1} \mathbf{t}}, \tag{4.21}$$

and ρ_b is the bias in the optimal SINR introduced by the transformation $\mathbf{T}$,

$$\rho_b = \frac{\mathbf{t}^H \Sigma^{-1} \mathbf{t}}{\mathbf{s}^H \mathbf{R}^{-1} \mathbf{s}}. \tag{4.22}$$

Equations 4.20-4.22 clearly demonstrate the effect of reduced rank transformation on the SMI-MVB method. The linear transformation $\mathbf{T}$ preserves the Gaussian distribution of the data, hence the reduced-rank CSNR, ρ_r, has a beta distribution with parameters K and r (i.e., the density in Equation 4.18 with N replaced by r). Improved statistical stability is evident in the higher CSNR values associated with ρ_r. For example, for the full-rank SMI, $E[\rho] = 0.5$ for a number of snapshots $K = 2N - 3$ [15], while for the reduced-rank SMI, $E[\rho_r] = 0.5$ for $K = 2r - 3$, i.e., fewer samples are required for the same performance level. The higher CSNR values due to improved statistical stability, are somewhat offset by the bias term ρ_b, which is the loss in the optimal SINR due to the rank reduction for known covariance matrix. This loss is the quantity $\mu/\mu_{\max}$ analyzed in the previous section. The density of ρ is then given in terms of the density of ρ_r by the expression:

$$f_\rho(\rho) = \frac{1}{\rho_b} f_{\rho_r}\left(\frac{\rho}{\rho_b}\right), \qquad 0 \le \rho \le \rho_b. \tag{4.23}$$

It is interesting to note that the linearly constrained (Frost-type) SNR maximization problem also has a rank reduction property and the corresponding CSNR has the same distribution as Equation 4.18 with N replaced by $N - n + 1$, where n is the number of linear constraints on the weight vector [54].

The performance of the GSC processor with a fixed rank-reducing transformation is analyzed in [55].

4.2.2 Analysis of Data Dependent Transforms

The case when $\mathbf{T}$ is data dependent cannot be directly derived from the SMI distribution. In this case $\mathbf{T}$ is a random matrix and its effect on the CSNR needs to be evaluated statistically. The weight vector may be constrained to lie either in the noise subspace or the interference subspace.

The method resulting from the noise subspace constraint is referred to as inverse PCI in [16] and as eigencanceler in [17]. The weight vector is given by

$$\mathbf{w} = \left(\mathbf{I}_N - \widehat{\mathbf{Q}}_r \widehat{\mathbf{Q}}_r^H\right) \mathbf{s} \tag{4.24}$$

The CSNR density function for the eigencanceler was derived in [56]. The derivation is based on the asymptotic expansion of the distribution of the principal components of the covariance matrix. Therein it is shown that, unlike the SMI density in Equation 4.18, for the eigencanceler the density depends on the covariance matrix. It is noted in reference [56], the expression in Equation 4.25 below was developed under the assumption that the projection of the steering vector $\mathbf{s}$ on the true interference subspace is negligible compared to its projection on the true noise subspace, i.e., $\rho_b \simeq 1$. Retracing some of the steps in [56], it is not difficult to show that when this assumption is not imposed, the CSNR can be expressed in the form $\rho = \rho_b \rho_r$ (as in Equation 4.20), with $\rho_b = \mathbf{s}^H \mathbf{Q}_v \mathbf{Q}_v^H \mathbf{s}$, and the density of ρ_r given by

$$f_{\rho_r}\left(\rho_r\right) = K \rho_r^{-2} \sum_{i=1}^{p} \frac{\pi_i}{\overline{\nu}_i} \exp\left(\frac{-K\left(\frac{1}{\rho_r} - 1\right)}{\overline{\nu}_i}\right), \qquad 0 \leq \rho_r \leq \rho_b, \tag{4.25}$$

where $\pi_i = \prod_{j=1, j\neq i}^{r} \overline{\nu}_i / \left(\overline{\nu}_j - \overline{\nu}_i\right)$, and $\overline{\nu}_i = \lambda_i^2 \left(\lambda_i - \sigma^2\right)^{-2}$, $i = 1, \ldots, p$. For large INR this expression simplifies to

$$f_{\rho_r}\left(\rho_r\right) = \frac{K^p}{\Gamma\left(p\right)} e^{-K\left(1-\rho_r\right)} \left(1 - \rho_r\right)^{p-1}. \tag{4.26}$$

The density of the CSNR $f_\rho(\rho)$ can then be computed as in Equation 4.23. The density of PCI's CSNR is similar in form to that of the SMI method, with the difference that in Equation 4.18 the signal dimensionality N is replaced by the quantity $(r = p + 1)$, [57]:

$$f_{\rho_r}(\rho_r) = \frac{\Gamma(K+1)}{\Gamma(p)\Gamma(K+1-p)}(1-\rho_r)^{p-1}\rho_r^{K-p}. \tag{4.27}$$

The relation between Equations 4.26 and 4.27 is explored in Appendix C.

In the introduction it was mentioned that LSMI is essentially a reduced-rank technique. Indeed, a CSNR distribution similar to Equation 4.27 is found in [20].

To complete the analysis of data dependent transforms, we now consider the case of the weight vector constrained to the interference subspace. We will refer to this method as principal components SMI (PC-SMI). Ignoring a constant gain, the PC-SMI weight vector is given by

$$\mathbf{w} = \widehat{\mathbf{Q}}_r\widehat{\mathbf{\Lambda}}_r^{-1}\widehat{\mathbf{Q}}_r^H\mathbf{s}, \tag{4.28}$$

where $\widehat{\mathbf{\Lambda}}_r$ is a diagonal matrix of the r principal eigenvalues of $\widehat{\mathbf{R}}$, and the columns of $\widehat{\mathbf{Q}}_r$ are the associated eigenvectors. Consistent with the earlier discussion on the topic, r is chosen larger than the actual interference subspace rank p. Direct analysis of PC-SMI's performance is very difficult since the CSNR is a function of both random eigenvalues and random eigenvectors. However, an approximation can be obtained based on the following argument. Let $\widehat{\mathbf{Q}}_r = \left[\widehat{\mathbf{Q}}_p\ \widehat{\mathbf{q}}_r\right]$, and $\widehat{\mathbf{\Lambda}}_r = \operatorname{diag}\left(\widehat{\mathbf{\Lambda}}_p\ \widehat{\lambda}_r\right)$,where $\widehat{\mathbf{Q}}_p$ and $\widehat{\mathbf{\Lambda}}_p$ are respectively the eigenvectors and eigenvalues of the rank p interference, $r = p + 1$, and $\widehat{\mathbf{q}}_r$, $\widehat{\lambda}_r$ are the index r (in descending order) eigenvector and eigenvalue. Then the PC-SMI weight vector can be expressed

$$\mathbf{w} = \widehat{\mathbf{Q}}_p\widehat{\mathbf{\Lambda}}_p^{-1}\widehat{\mathbf{Q}}_p^H\mathbf{s}+\widehat{\lambda}_r^{-1}\widehat{\mathbf{q}}_r\widehat{\mathbf{q}}_r^H\mathbf{s} \tag{4.29}$$

For large interference eigenvalues, the elements of $\widehat{\Lambda}_p^{-1}$ are negligible, and Equation 4.29 can be approximated with

$$\mathbf{w} \simeq \widehat{\lambda}_r^{-1}\widehat{\mathbf{q}}_r\widehat{\mathbf{q}}_r^H\mathbf{s}. \tag{4.30}$$

Since the vector $\widehat{\mathbf{q}}_r$ is the noise subspace with respect to the rank p interference, this PC-SMI is equivalent to a noise subspace canceler. Thus under the assumption that the interference eigenvalues are very large, the density of ρ_r is given by Equation 4.26. The overall CSNR is $\rho = \rho_b\rho_r$. For PC-SMI, $\rho_b = \mathbf{s}^H\mathbf{q}_r\mathbf{q}_r^H\mathbf{s}$ is the projection of the steering vector $\mathbf{s}$ onto the eigenvector $\mathbf{q}_r$. For the eigencanceler $\rho_b = \mathbf{s}^H\mathbf{Q}_v\mathbf{Q}_v^H\mathbf{s}$, where $\mathbf{Q}_v = [\mathbf{q}_r, \mathbf{q}_{r+1}, \ldots, \mathbf{q}_{Nr}]$. Now, since $\mathbf{s}^H\mathbf{Q}_v\mathbf{Q}_v^H\mathbf{s} \geq \mathbf{s}^H\mathbf{q}_r\mathbf{q}_r^H\mathbf{s}$, and the ρ_r's are the same, it would seem that the eigencanceler would always be preferable. This conclusion however is based on the assumption that the elements of $\widehat{\Lambda}_p^{-1}$ are negligible. In general, PC-SMI is recommended when the steering vector lies mostly in the interference subspace, and conversely, when the steering vector is mainly in the noise subspace, the eigencanceler method should be applied.

CHAPTER 5

NUMERICAL RESULTS

Numerical results presented in this chapter were derived from computer simulations as well as from processing real data collected by the DARPA sponsored Mountain-Top program. Simulated data is used to compare the various techniques that have been presented in earlier chapters. The Mountain-Top data is used to demonstrate the performance of the various techniques on real-world data. Analysis of the Mountain-Top data reveals target cancellation due to mismatch between the true received signal vector and the steering vector used in weight calculation as well as the training area used for the calculation of the covariance matrix.

5.1 Simulated Data

The simulation model used an $\nu = 8$ element array with $\kappa = 4$ taps at each element. The clutter was located in the angular sector of 0 to 30 degrees. The input clutter-to-noise ratio (CNR) was 10 dB at each antenna. In Figures 5.1(a), 5.2(a), and 5.5(a), two jammers were located at 15 and 20 degrees with a jammer-to-noise ratio (JNR) of 10 dB at each antenna. The interference subspace rank is bound by $r \leq \nu + \kappa - 1 = 11$. The bound would be achieved for interference that covers the full space-Doppler domain. For the sample covariance matrix used in the simulation, the clutter does not cover the whole space-Doppler domain and the interference rank was found to be 6. The steering vector was set at 50 degrees, and at a normalized Doppler frequency of 0.4. The effect of the assumed rank p of the interference subspace on the average CSNR is shown in Figure 5.1(a). For each method, the CSNR was computed from Equation 4.17.

The eigencanceler's weight vector used in Equation 4.17 is given by Equation 4.24. For the DCT and DFT reduced-rank transformations, $\mathbf{T}$ was constructed from the steering vector $\mathbf{s}$, and the vectors corresponding to the p principal components of each transformation. The CSNR was computed from Equation 4.19. In case of the CSM method, the matrix $\mathbf{U}$ was constructed as in Equation 4.12 substituting estimated values for unknown quantities. The CSM weight vector was subsequently evaluated from Equation 4.8. The curves shown represent averages of 5000 runs. CSM provides slightly better performance when the rank is underestimated. The DCT-based method seems to be the least affected by overestimating the rank of the interference subspace.

The effect of the assumed rank p of the interference subspace on the average CSNR is shown in Figure 5.1. For each method, the CSNR was computed from Equation 4.17. In the case of the the particular scenario considered without jammers (Figure 5.1(a)), all methods peak near an interference subspace rank of $p = 4$, the true rank of the interference subspace. In the scenario considered with jammers (Figure 5.1(b)), the eigencanceler and CSM methods peak near an interference subspace rank of $p = 6$, the true rank of the interference subspace. The DCT method peaks near an interference subspace rank of $p = 8$ while the DFT method peaks near an interference subspace rank of $p = 7$. The different rank values required by each method for best performance, are indicative of different capabilities to concentrate the power in a few principal values.

Several other methods are compared in Figure 5.2(a): PC-SMI, reduced-rank GSC, DFT-based CSM, and DCT-based CSM [21, 22]. The PC-SMI weight vector was computed from Equation 4.28. The reduced-rank GSC weight vector was evaluated using Equation 4.8, where the matrix $\mathbf{U}$ consisted of the p principal eigenvectors of $\widehat{\mathbf{R}}_a = \mathbf{A}\widehat{\mathbf{R}}\mathbf{A}^H$. The CSM methods shown in the figure are not discussed in this work; details on those methods can be found in [21, 22]. At their respective optimal rank orders, the CSNR peak values for the eigencanceler, CSM, PC-SMI and reduced-rank GSC are in close agreement.

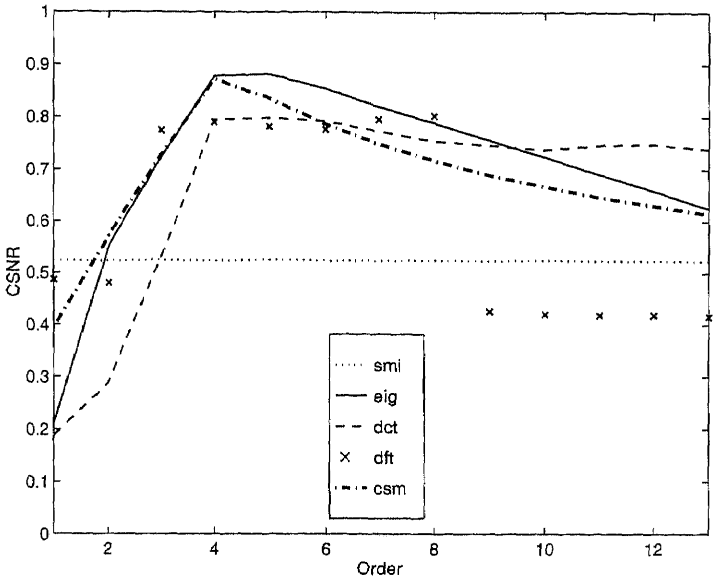

(a) CSNR vs Rank order - without jammers

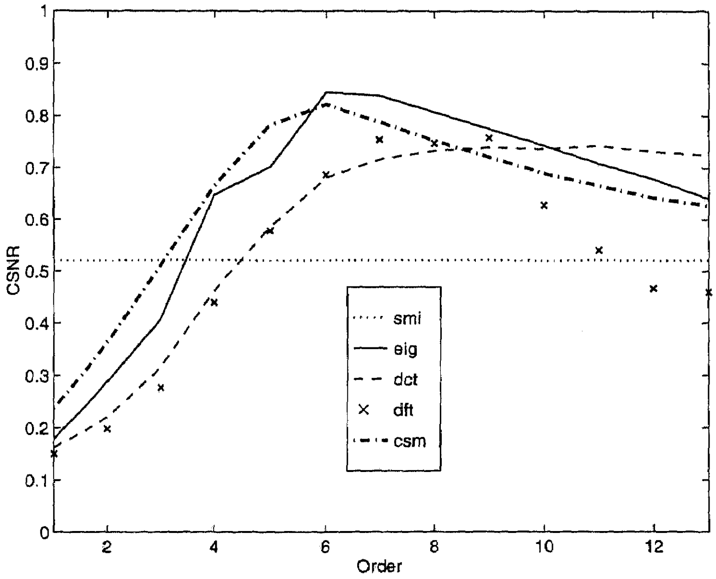

(b) CSNR vs Rank order - with jammers

Figure 5.1 CSNR vs Rank order

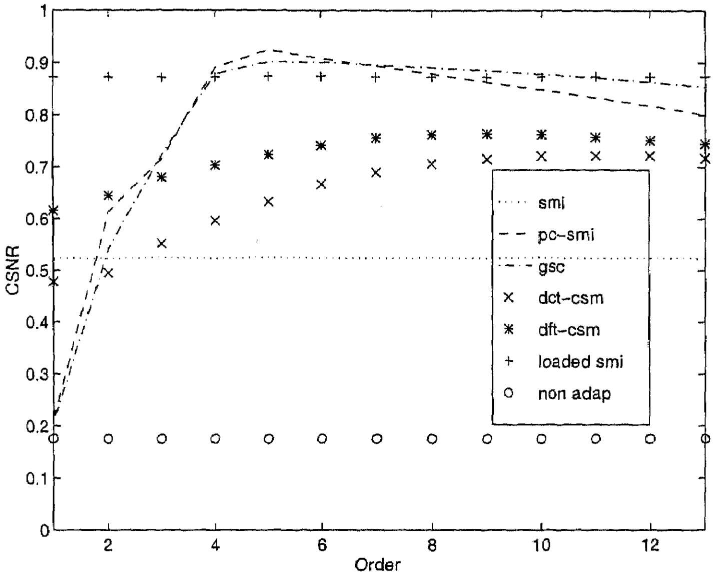

(a) CSNR vs Rank order for other techniques - without jammers

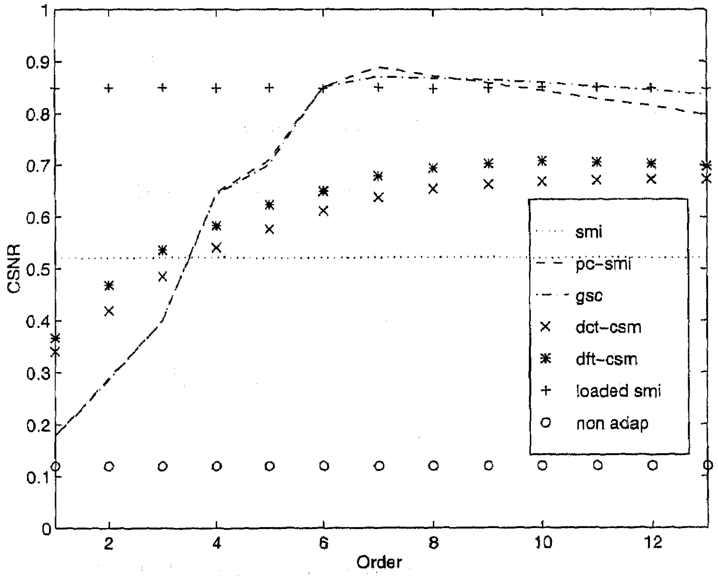

(b) CSNR vs Rank order for other techniques - with jammers

Figure 5.2 CSNR vs Rank order for other techniques

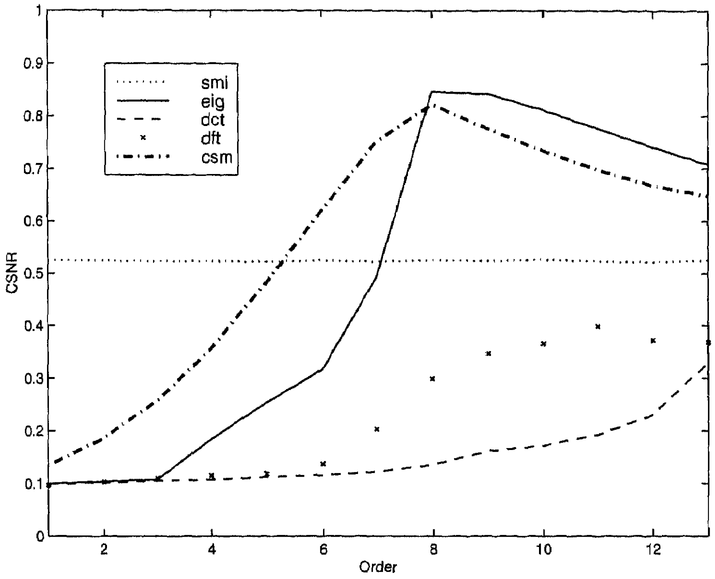

Figure 5.3 CSNR vs Rank order with large clutter field

In Figures 5.3 and 5.4 the clutter was located in the angular sector of 0 to 180 degrees. The CNR per channel was 10 dB. The construction of **T** and **U** for the various techniques was performed as in Figures 5.1(a) and 5.2(a). As shown in the figures, the peak for the eigencanceler, CSM, reduced-rank GSC, and PC-SMI occur at a rank of $p = 8$. As expected, the more extended clutter leads to a larger number of principal values. As in the other simulations, the eigencanceler, CSM, PC-SMI, and reduced-rank GSC are in close agreement. The DCT and DFT reduced-rank transformations do not perform as well in this scenario. This is due to the lower capability of these techniques to concentrate the clutter power in a limited number of principal values.

In Figure 5.5, the distribution of ρ based on 20,000 runs is shown for several reduced-rank methods, as well as for full-rank SMI. The reduced-rank methods were: eigencanceler, DCT, DFT, and CSM based on the eigen-decomposition and implemented as a GSC. In the case without the jammer, the number of principal components used to generate the results shown in Figure 5.5(a) was $p = 4$ for all

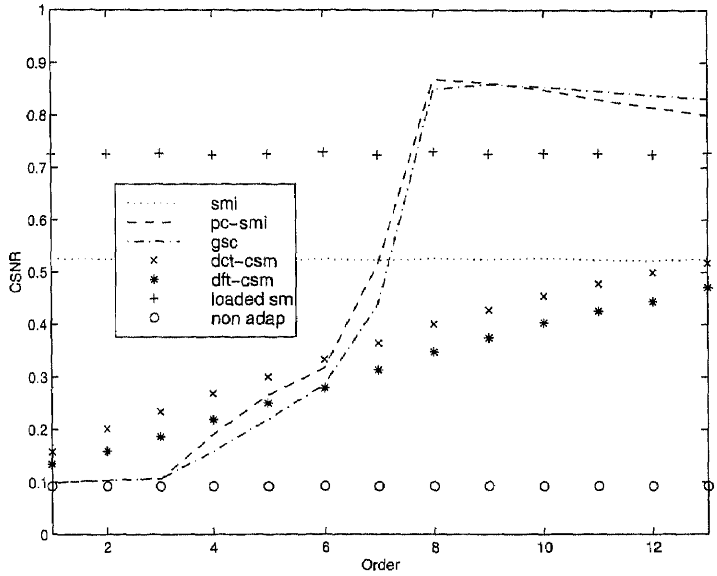

Figure 5.4 CSNR vs Rank order for other techniques with large clutter field

methods. With the jammers included, the number of principal components used to generate the results shown in Figure 5.5(b) was $p = 6$ for the eigencanceler and CSM, $p = 7$ for the DFT, and $p = 8$ for the DCT. In both cases, the highest CSNR's are exhibited by the CSM and eigencanceler methods, with reduced-rank MVB based on the DCT and DFT providing slightly lower performance. All reduced-rank methods clearly outperform the full-rank SMI.

As shown in section 4.2.1, the DCT and the DFT reduced-rank CSNR, ρ_r, have a beta distribution. The simulated CSNR of the DCT and the DFT reduced rank cases may be compared to the theoretical CSNR using Equation 4.20. In Figure 5.6, the simulated and theoretical CSNR results for both the DCT and DFT are shown. There is good agreement between the theoretical results and the simulations

Figure 5.7 shows the average probability of detection. To compute the probability of detection, we make the assumption that the target amplitude a in Equation 3.2 is a zero-mean, circularly symmetric complex Gaussian random variable with variance σ_s^2. The test statistic is given by $y(k) = \left|\mathbf{w}^H \mathbf{x}(k)\right|^2$. Under $\mathbf{H}_0$, $y(k)$ has an

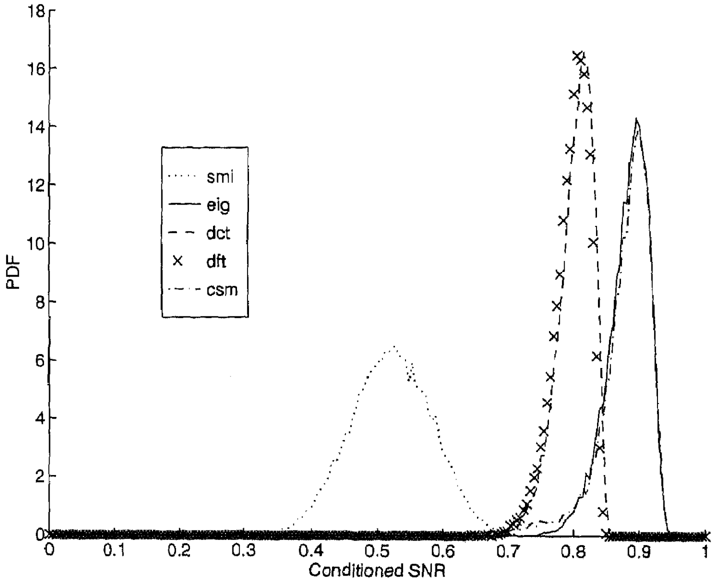

(a) Probability density of the CSNR - without jammers

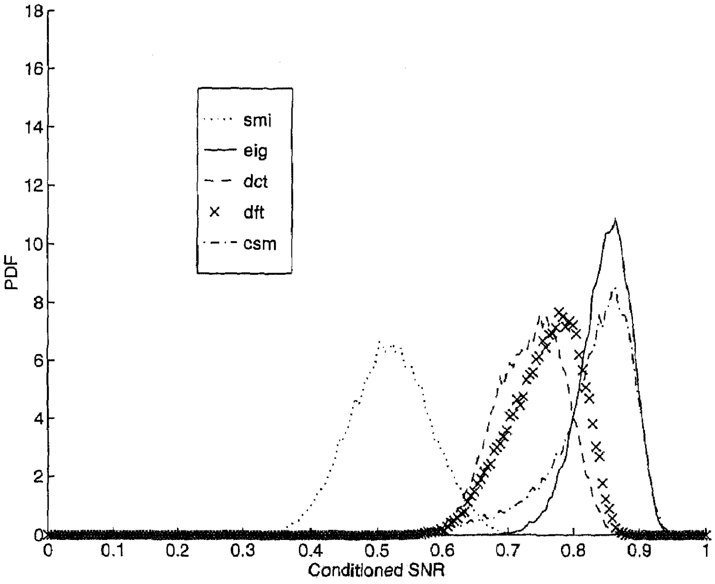

(b) Probability density of the CSNR - with jammers

Figure 5.5 Probability density of the CSNR

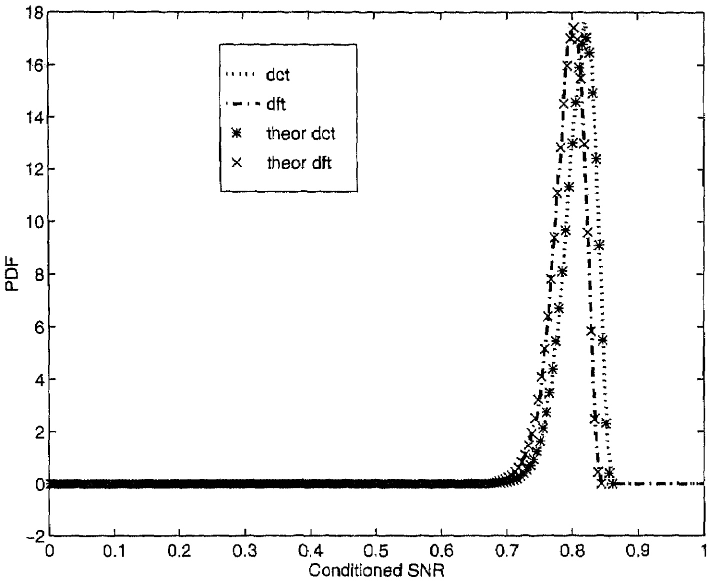

Figure 5.6 Theoretical and simulated CSNR for the DCT and DFT

exponential distribution with density $f_y(y) = (1/\bar{y})\, e^{-y/\bar{y}}$, where $\bar{y} = E[y] = \mathbf{w}^H\mathbf{R}\mathbf{w}$. Setting the weight vector gain in Equation 4.17 such that $\left|\mathbf{w}^H\mathbf{s}\right|^2 = 1$, we have $\bar{y} = 1/\rho\alpha$, where $\alpha = \mathbf{s}^H\mathbf{R}^{-1}\mathbf{s}$. The probability of false alarm conditioned on the CSNR ρ is given by

$$\begin{aligned} P_f(\rho) &= \int_{-\infty}^{y_T} f_y(y)\, dy \\ &= e^{-\rho\alpha y_T}, \end{aligned} \tag{5.1}$$

where y_T is the detection threshold. The average probability of false alarm is given by

$$P_f = \int_0^1 P_f(\rho)\, f_\rho(\rho)\, d\rho, \tag{5.2}$$

where $f_\rho(\rho)$ is the density of CSNR, which depends on the STAP method applied. Under $\mathbf{H}_1$, $y(k)$ has an exponential distribution with parameter $\bar{y} = E[y] = \sigma_s^2 + \mathbf{w}^H\mathbf{R}\mathbf{w} = \sigma_s^2 + 1/\rho\alpha$. It follows that the conditional probability of detection is given by

$$P_d(\rho) = \exp\frac{-\rho\alpha y_T}{1+\rho\alpha\sigma_s^2}. \tag{5.3}$$

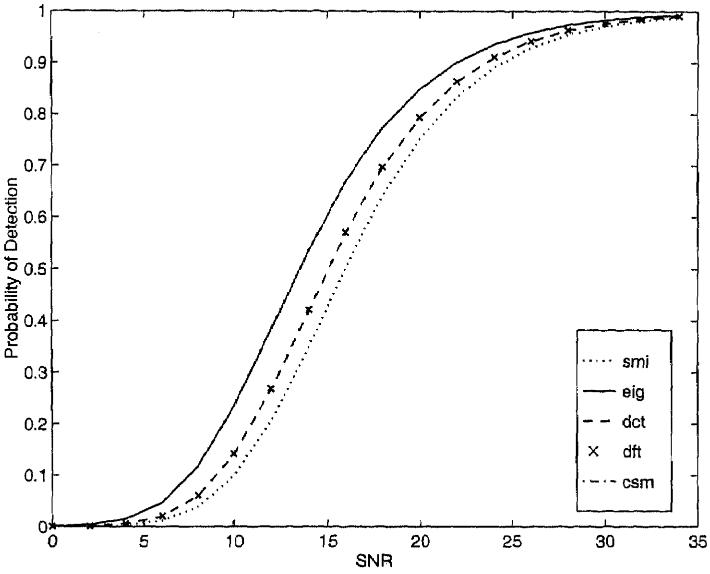

Figure 5.7 Probability of detection for reduced-rank methods

The average probability of detection is then expressed

$$P_d = \int_0^1 P_d(\rho)\, f_\rho(\rho)\, d\rho. \tag{5.4}$$

In the simulations, we found the threshold $y_T(\rho)$ such that $P_f(\rho) = 10^{-5}$ and averaged the thresholds over 200 runs to obtain an average threshold value. This value was then used to compute $P_d(\rho)$ as a function of the SNR. For each SNR and each method, 200 values of $P_d(\rho)$ are averaged to serve as a point on the curves in Figure 5.7. The figure illustrates the same trends as Figure 5.5(a); best detection performance is provided by the eigencanceler and CSM, followed by DCT and DFT (indistinguishable), and finally the full-rank SMI.

The effect of the CNR on performance is illustrated in Figure 5.8. The CSNR is plotted as a function of the input CNR. The CSNR is computed for a rank-reducing transformation with $r = 4$. As the CNR increases, the interference power spills over more than 3-4 principal values. Thus the rank reducing transformations are inadequate in capturing the interference power and performance is degraded.

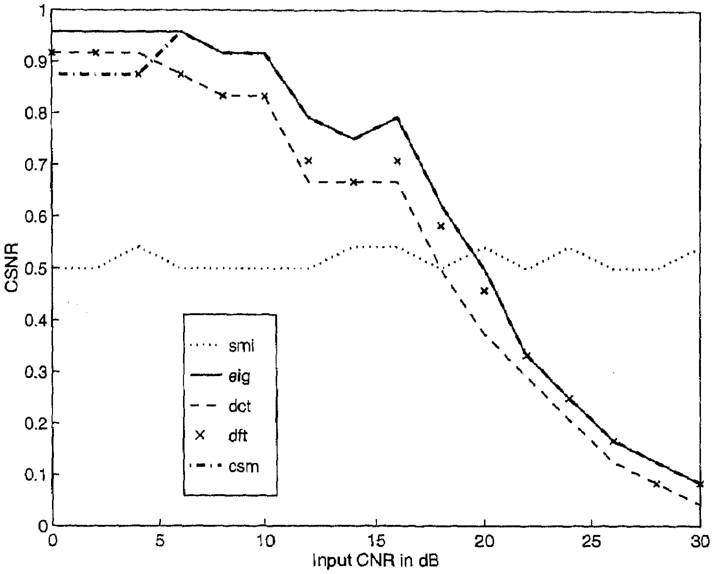

Figure 5.8 CSNR vs CNR

The signal cancellation effects on the various STAP techniques under investigation are shown in Figures 5.9 and 5.10. In these figures, the SNR axis is based on the quantity $(\sigma_d^2 + \sigma_i^2)/\sigma_n^2$. Figure 5.9 shows the effects of SNR and the pointing error on the array gain using Equation 3.34. There are no phase and amplitude errors so $c_i = \sqrt{1/N}$. The target is at bore sight ($\theta_d = 0^\circ$) and the interference angle is 15°. As shown in the figures, when the SNR is small the pointing errors have the least effect on the array gain. As the SNR increases, the performance degrades for a small pointing error as the SMI's mainlobe narrows. The eigencanceler's performance is acceptable up to an SNR of 15 *dB* but decreases as the SNR approaches the INR. This is due to the shift of the first eigenvector towards the desired signal as the SNR approaches the INR. The CSM performs better than the SMI at low SNR however it is not as acceptable as the eigencanceler. The input signal in this case was one signal and one interferer. The Eigencanceler and CSM perform well with one transform term. However, due to the way that the fixed transforms perform, their performance is unacceptable with one term. The DCT and DFT techniques were performed with $p = 5$. In this case, the DCT's performance is similar to the SMI. The DFT is also similar to the SMI with the exception of several spikes at low SNR as the pointing error is increased. These are due to the way that the DFT processes the input signal. Additional terms in the DFT processing will reduce these effects.

Figure 5.10 show the effects of the phase and pointing errors. There are no amplitude errors and the phase errors are modeled as a zero-mean Gaussian random variable. The phase errors were evaluated using 50 Monte Carlo runs. The SMI exhibits a larger degradation in the array gain than the eigencanceler in the case of both pointing and phase errors. The eigencanceler exhibits almost no loss of performance for phase errors up to 8° while the SMI gain is decreased to 1/2 for phase errors with a standard deviation of 5°. The CSM shows good performance for phase errors up to 6°. The DCT gain is decreased to 1/2 for phase errors with a standard deviation of 8°. The DFT's performance is similar to that of the SMI. As illustrated before, the eigencanceler's pointing error is less than that of the other techniques.

5.2 Mountain-Top Data

The performance of the various reduced-rank methods are compared to one another when applied to the Mountain-Top dataset . This data was collected from commanding sites (mountain tops) and radar motion is emulated using a technique developed at Lincoln Laboratories [58]. The sensor consists of 14 elements and the data is organized in coherent pulse intervals (CPI) of 16 pulses. For the dataset analyzed here, the clutter was located around 245 degrees azimuth and the target was at 275 degrees and at a Doppler frequency of 156 Hz. A synthetic target was introduced in the data at 275 degrees and 156 Hz. Note that the clutter and target have the same Doppler frequency, hence separation is possible only in

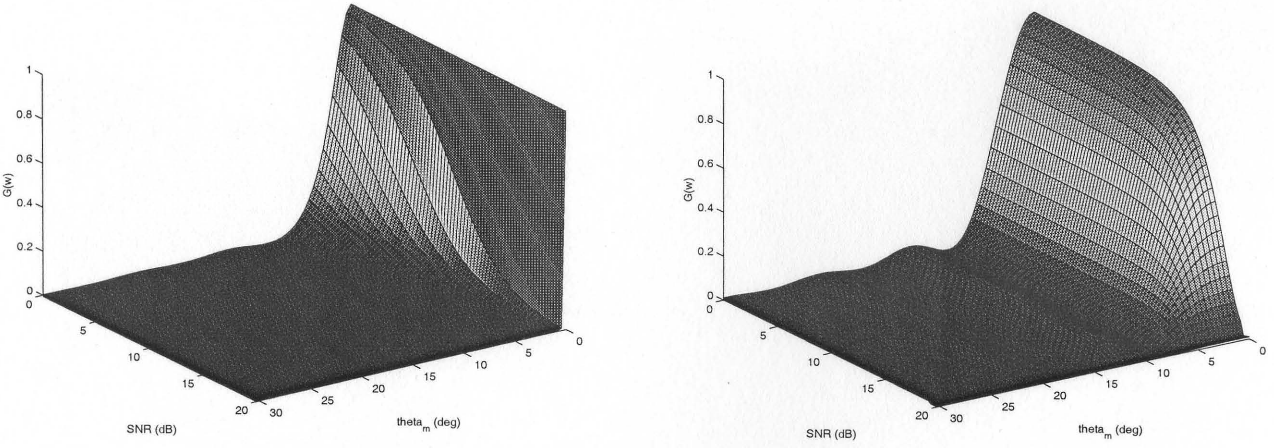

(a) Sample Matrix Inversion

(b) Eigencanceler

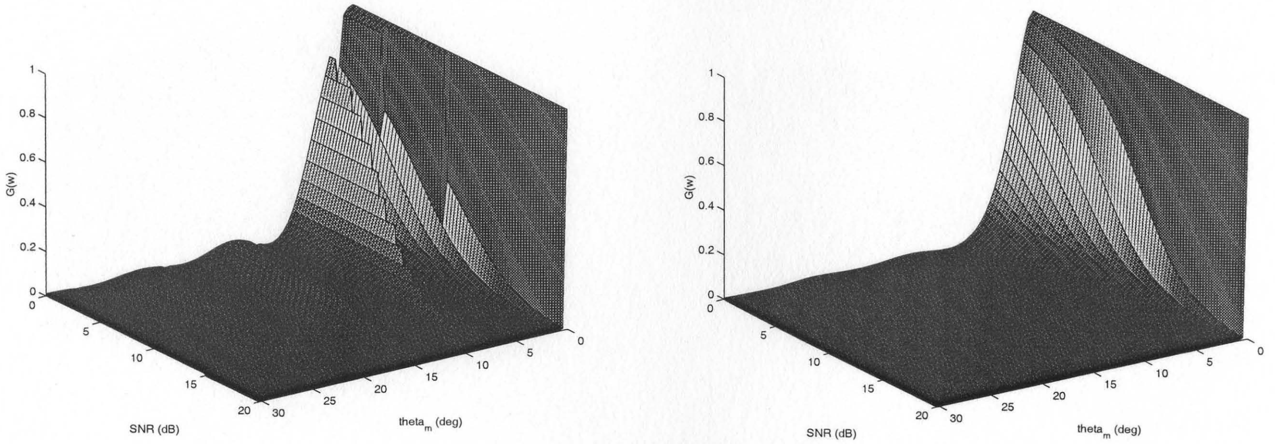

(c) CSM

(d) DCT

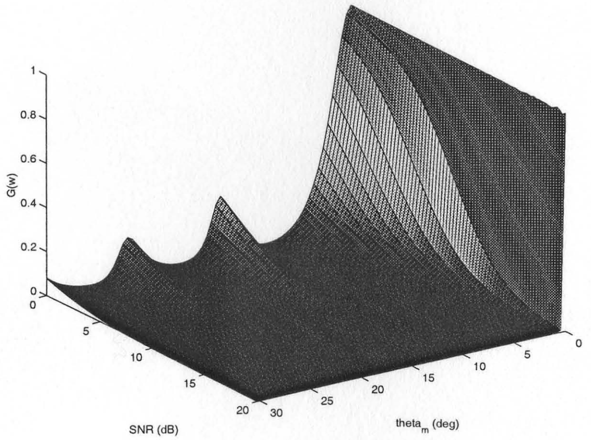

(e) DFT

Figure 5.9 Effects of SNR and Relative Pointing Error

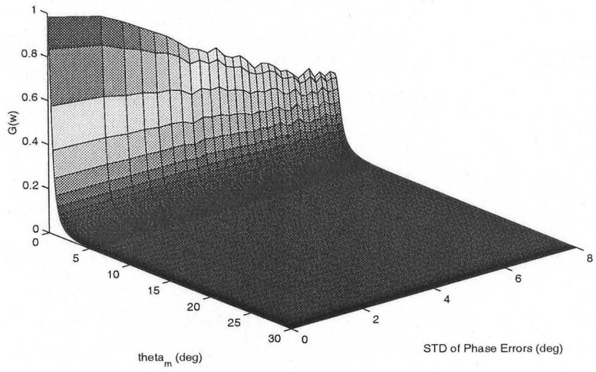

(a) Sample Matrix Inversion

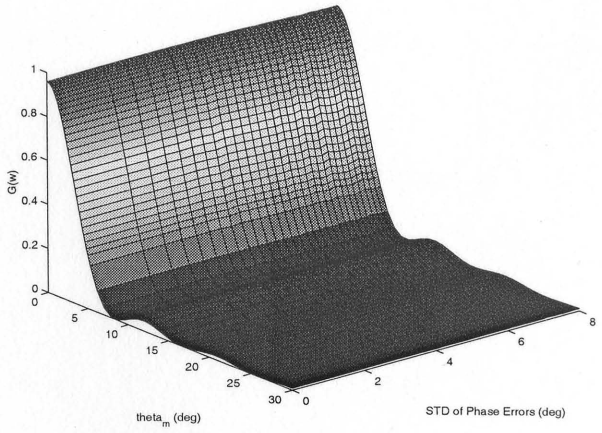

(b) Eigencanceler

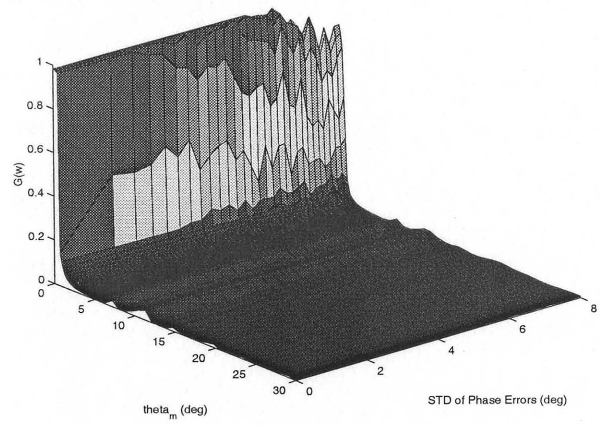

(c) CSM

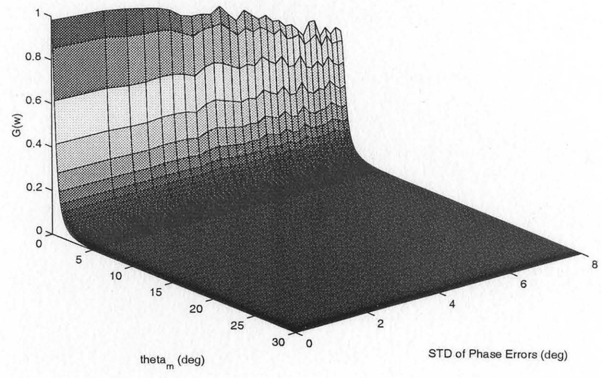

(d) DCT

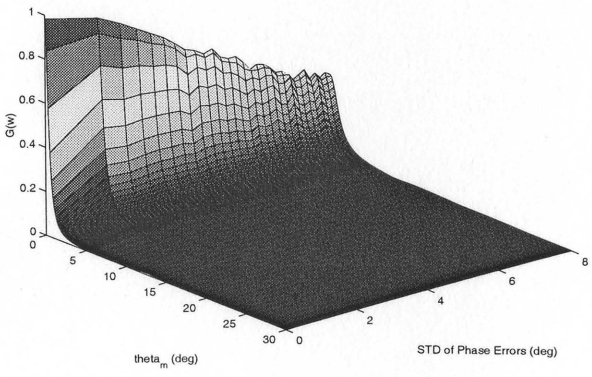

(e) DFT

the spatial domain. The target is not detectable without processing. The data analyzed was post-Doppler processing. A 16 × 14 matrix was formed for each range cell, where the temporal information is in the matrix columns, and the spatial information is contained in the rows. The received signals were processed using fixed Doppler filters. The filter containing the target and clutter was selected for follow-up processing and spatial processing was applied to 14 × 1 data vectors.

The spatial steering vector was formed using the known target angle. The data was plotted relative to sky noise. Weight vectors were computed from a 60 data point training set. In the first scenario, shown in Figure 5.11, the training range cells were from 145 km to 152 km (outside the target region). The SMI, eigencanceler, CSM, DCT, and DFT methods detect the target and suppress the clutter. Each method provides cancellation of the training region due to the covariance matrix being formed from data in this region. Each of the reduced-rank methods were evaluated utilizing four principal values (plus the steering vector in the case of the DCT and the DFT). For comparison purposes, the curve representing the unadapted data is also shown in Figure 5.12. The unadapted weight vector was taken equal to the steering vector ($w = s$). The target is clearly not detectable without adaptive processing.

Figure 5.13 shows the second scenario where the training is applied around the target region from 150 km to 158 km with the target region (5 range cells) omitted from the training set. The eigencanceler's performance is very similar to the first training area. The performance of the SMI is decreased by 4 dB due to the residual cancellation that the SMI is sensitive. While this scenario does give good results, omitting the target region is not a practical approach of training since the weight vector would need to be recalculated for each target under test. Each of the reduced-rank methods were evaluated utilizing four principal values (plus the steering vector in the case of the DCT and the DFT). The target is clearly indicated by all methods.

The third scenario, shown in Figure 5.14 includes all of the data vectors in the target region from 150 km to 158 km, including the target area, in the training. The presence of the target region causes an increase in the desired signal component in the estimated correlation matrix. This, put together with calibration errors, causes a deep signal cancellation by the SMI method. The eigencanceler, CSM, DCT, and DFT are only slightly affected by the presence of the signal in the training set.

Figure 5.15 displays the echo magnitude at the target range cell and for the beamforming at various angles. The figure was generated by scanning the steering angle over the angular sector indicated by the abscissa. The gain of each technique is measured with respect to the output when the beamformer points in the actual target direction (at 275 degrees). This plot emulates the radar's search mode. In the case presented, the eigencanceler and the CSM patterns are very similar to one another. Near the target angle, the DFT and the SMI are also at a maximum. The DCT pattern is at a maximum close to the target angle, but not directly on the steering angle. This is due to the number of DCT terms used and the training data utilized in the formation of the covariance matrix in this simulation.

Typically, the cell under test as well as cells in its vicinity are not included in the estimate of the covariance matrix. This implies a cumbersome procedure as different covariance matrices need to be associated with different range cells. Robust methods such that the same covariance matrix can be used for all range cells are of practical interest. The reason is that if the target signal is included in the covariance, target cancellation may occur to the extent that the presumed steering vector is different from the true target vector. Differences between the steering vector and the true target vector may occur due to either pointing or calibration errors. Here, assume that the steering vector $\mathbf{s}$ is precisely the target vector. Let the covariance matrix without the target contribution be $\mathbf{R}$, and with the target be $\mathbf{R}_1$. Then $\mathbf{R}_1 = P\mathbf{s}\mathbf{s}^H + \mathbf{R}$, where P is the power of the target. It is easy to show that the

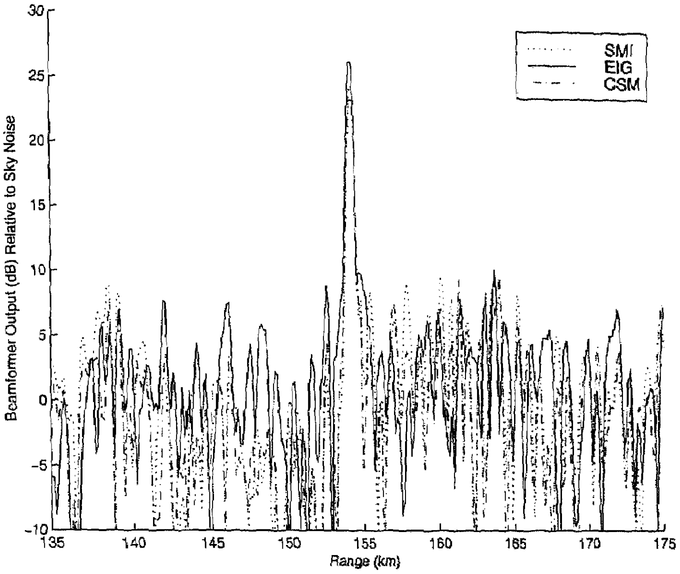

(a) Training outside the target region. SMI, EIG, and CSM techniques

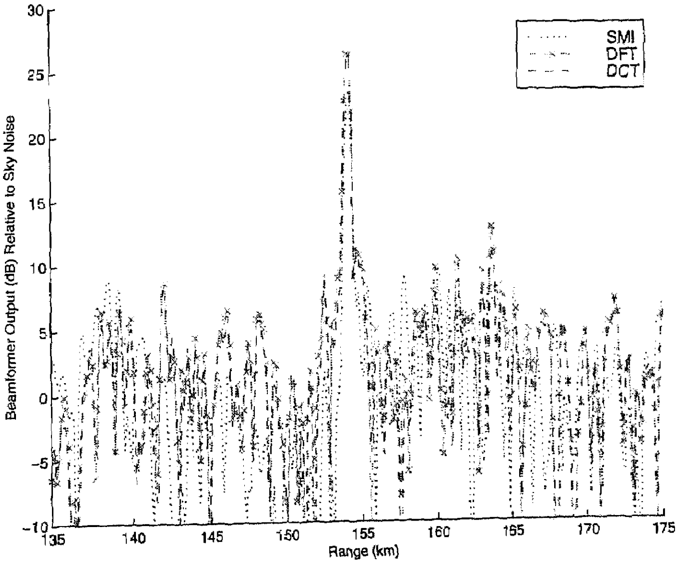

(b) Training outside the target region. SMI, DCT, and DFT techniques

Figure 5.11 Post-Doppler range plots using 60 training points with training outside the target region

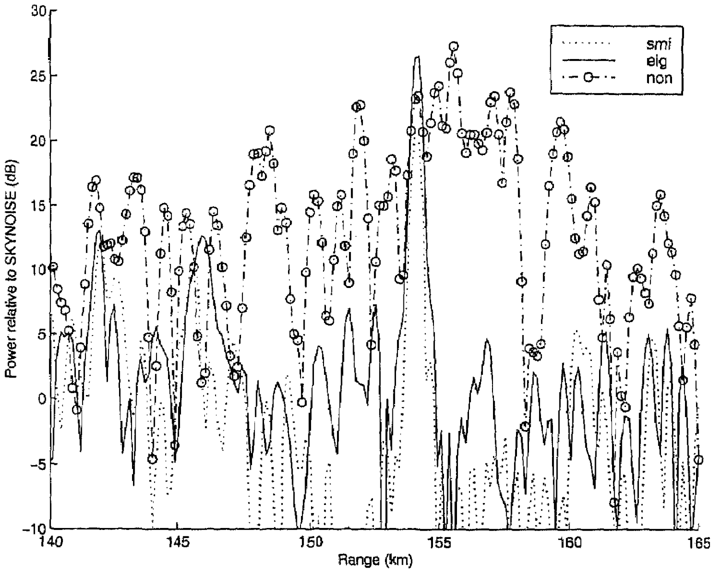

Figure 5.12 Post-Doppler range plots using 60 training points with training outside the target region. SMI, EIG, and non-adaptive techniques

SMI weight vector will remain unchanged (up to a gain factor). Hence, inclusion of the target in this case has no impact on the array performance. Conversely, when the steering and the target vectors differ, presence of the target will cause a shift in the weight vector. In this case, the target is interpreted as an interference and the array acts to reject it. Since in practice it is difficult to ensure that the target and steering vector are equal (no pointing error and perfect calibration), to preclude target cancellation, covariance matrix estimation is done without the range cells in the vicinity of the one tested. Reduced rank methods constrain the weight vector to the noise subspace. These methods tend to be less susceptible to the presence of the target in the training data, since a few target cells may cause no change in the interference/noise subspace partition [59]. Indeed, the covariance matrix may be expressed

$$\mathbf{R} = \frac{1}{K}\sum_{k=1}^{K} \mathbf{x}_k \mathbf{x}_k^H + \frac{1}{K}\sum_{m=1}^{M} \mid a_m \mid^2 \mathbf{s}\mathbf{s}^H, \tag{5.5}$$

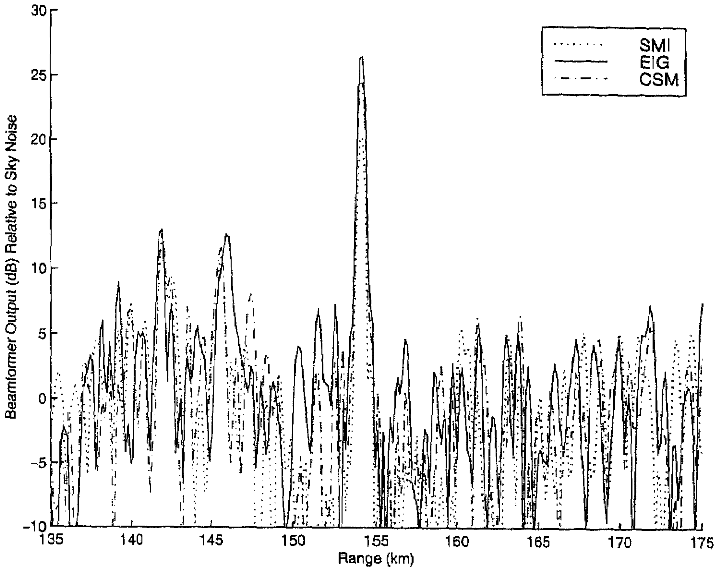

(a) Training around the target region, target not included. SMI, EIG, and CSM techniques

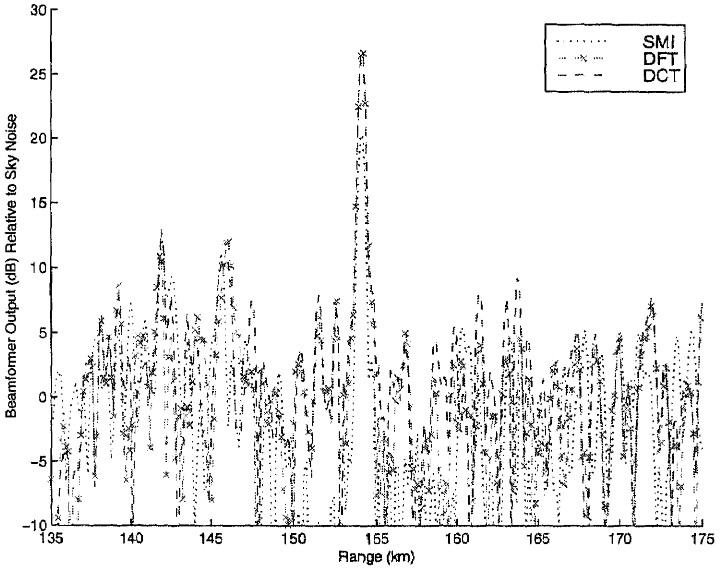

(b) Training around the target region, target not included. SMI, DCT, and DFT techniques

Figure 5.13 Post-Doppler range plots using 60 training points with training around the target region with the target not included

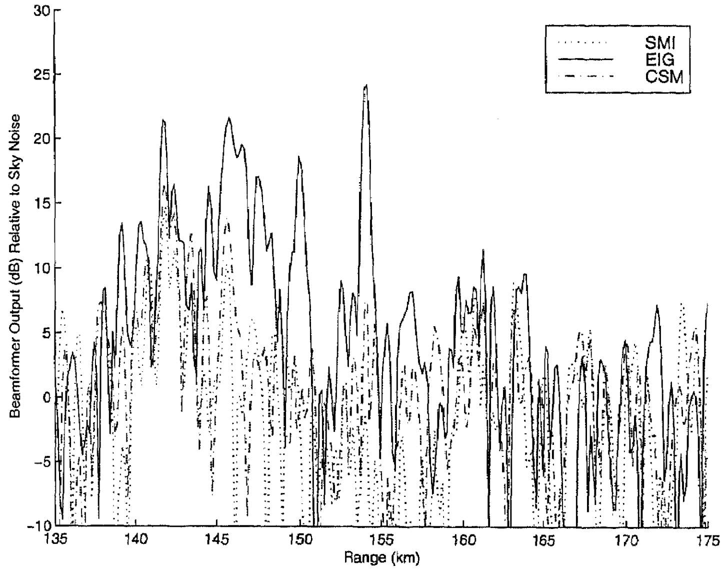

(a) Training around the target region, target included. SMI, EIG, and CSM techniques

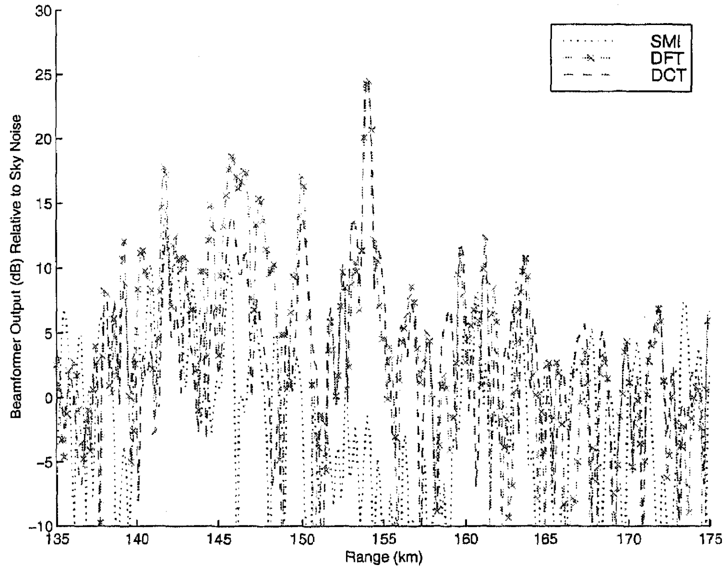

(b) Training around the target region, target included. SMI, DCT, and DFT techniques

Figure 5.14 Post-Doppler range plots using 60 training points with training around the target region with the target included

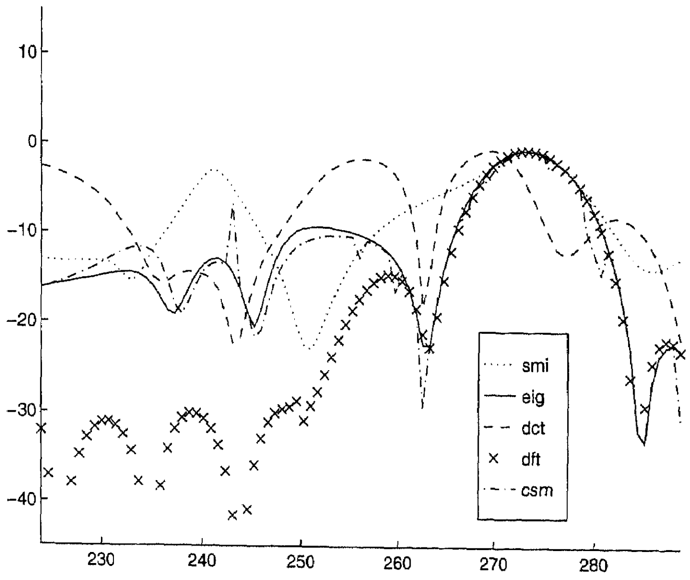

Figure 5.15 Angle scan with the target not included in the training

where M is the number of range cells for which there is a target return and a_m are the target complex amplitudes. As the size of the training region (i.e. K) is increased, and since the number of range cells containing the target is kept fixed, the signal power decreases with respect to the interference. Thus at large K, the effect of the target presence in the training data should be negligible. A measure of target cancellation at the array output is provided by the ratio r of the target power at the array output when training is done over a subset of cells including the target cell to the target power when training is done over all of the range cells. The quantity $1-r$ measures the target cancellation relative to training over the full range interval. This quantity was computed from the Mountain-Top data, and is plotted in Figure 5.16 . The eigencanceler, DCT, and DFT methods exhibit lower signal cancellation than the SMI and CSM.

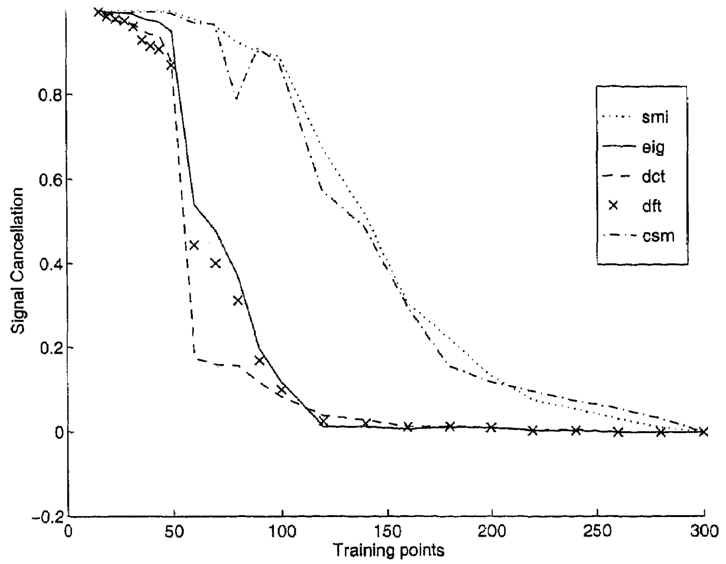

Figure 5.16 Signal cancellation based on the number of training points

CHAPTER 6

CONCLUSIONS

This work has brought together various methods used to study synthetic aperture radar (SAR) and space-time adaptive processing (STAP) radar systems. As stated previously, radar systems may be processed with various space, time and frequency techniques. Advanced radar systems are required to detect targets in the presence of jamming and clutter and this interference is seen by the radar systems in various ways. To perform interference cancellation, multidimensional filtering over the spatial and temporal domains is required. Uncertain knowledge of the clutter and jamming environment requires systems that perform data-adaptive processing.

For SAR, a technique for extracting the target motion parameters from the data was introduced. The technique was based on processing the signal with various time-frequency distributions. The parameters may then be subsequently used in a SAR system to adjust the processing to focus on the moving object within the field. The signal received from a target moving over a stationary background can be modeled as samples of a chirp signal embedded in noise.

STAP radar performance was studied with the focus on the problem that, in STAP, the dimension of the adaptive weight vector can become large. As this dimension becomes larger, the required sample support for STAP detection also needs to increase. Publications have shown the advantages of various forms of reduced-rank processing over the full-rank SMI. Given a rank reducing transformation, adaptation can take place in the subspace spanned by the principal components of the transform (interference subspace methods) or in the complementary subspace (noise subspace methods). The transforms are either fixed (such as discrete Fourier transform - DFT, or discrete cosine transform - DCT) or data dependent such as the eigencanceler or the cross-spectral metric (CSM). Reduced-rank methods are important for STAP radar, where a large number of degrees of freedom may be available. For a uniform array and for fixed PRF, the space-time clutter covariance matrix is essentially low-rank due to the inherent oversampling nature of the STAP architecture. As has been demonstrated, the space-time radar problem is well suited to the application of techniques that take advantage of the low-rank property.

An overview of the various time-frequency techniques studied were given in Chapter 2. The response of each technique used was shown when analyzing a sine wave and a multicomponent signal. Basic properties associated with each technique were also introduced. The time-frequency techniques were used to estimate SAR target parameters. This work was based on the concept that a signal received in a SAR system from a target moving over a stationary background may be modeled as samples of a chirp signal embedded in noise and the problem of estimating the motion parameters of this moving target is equivalent to the estimation of a chirp signal in a noisy environment. The application of four specific TF analysis techniques: the short-time Fourier transform, the Gabor expansion the Continuous Wavelet transform and the Wigner-Ville distribution, to the estimation of the relative along-track velocity between the SAR platform and a moving target were presented. It was shown that various TF analysis techniques may be used to analyze the track of a moving target with SAR. Each of the TF analysis techniques examined display a sharp threshold effect when used to obtain the instantaneous frequency of a signal. The optimality of the WVD for the determination of the IF was verified and compared to the results obtained for the cases of the STFT the Gabor expansion and the CWT. In the simulations performed, the STFT was closer to the Cramér-Rao bound than the Gabor expansion and the CWT. In all cases, the relative velocity mismatch introduced by the boat motion was less than 6% of the SAR platform velocity.

Chapter 3 introduced the space-time adaptive processing signal environment. The definitions and mathematical model of the signals used for the STAP work was also presented. The Sample Matrix Inversion (SMI), Generalized sidelobe canceler (GSC), Eigencanceler, and fixed transforms techniques are all introduced. Target cancellation and closed form expressions for the SMI and eigencanceler are presented. An expression for fixed transforms is also shown.

Reduced-rank methods for STAP based on the signal model were presented in Chapter 4. Reduced-rank methods with known and unknown covariance matrices were analyzed. The analysis is carried out in the framework of the minimum variance beamformer and the generalized sidelobe canceller. A method was developed to evaluate the theoretical performance of reduced-rank techniques when the rank-reduction is carried out by a fixed transform. The PC-SMI technique was recommended when the steering vector lies mostly in the interference subspace, and conversely, when the steering vector is mainly in the noise subspace, the eigencanceler method should be applied.

The application of several reduced-rank methods to the STAP problem was studied by analysis, simulations, and analysis of real data (in Chapter 5). The motivation for the application of reduced-rank methods is that the STAP problem is inherently low-rank. Restriction of the number of degrees of freedom through the application of reduced-rank methods has the advantage of providing robust covariance matrix estimates resulting in improved performance over SMI. A taxonomy of reduced-rank methods was presented and specific methods were analyzed. The CSNR was defined as a figure of merit for the array performance when the interference covariance matrix is estimated from a training set. Various adaptive methods are compared according to their CSNR performance. A general expression for the CSNR density function was developed for reduced-rank methods utilizing fixed transforms. When compared to the CSNR of SMI, reduced-rank methods exhibit fewer degrees of freedom and a bias term. While best performance is obtained using transforms based on the eigendecomposition (data dependent), the loss incurred by the application of fixed transforms (such as the discrete cosine transform) is relatively small. The main advantage of fixed transforms is the availability of efficient computational procedures for their implementation. The effects of calibration errors and covariance training ranges were also presented. It was illustrated that adaptive radar is susceptible to signal cancellation when the target it included in the training data. It was shown that signal cancellation with the SMI, CSM, DCT and DFT is sensitive to the SNR and magnitude of the pointing errors. The eigencanceler is much more robust than the SMI with respect to signal cancellation.

APPENDIX A

DISCRETE COSINE TRANSFORM

In discrete Wiener filtering, the filter is represented by G, an $M \times M$ matrix. The estimate of the data vector $\mathbf{x}$ is

$$\hat{\mathbf{x}} = \mathbf{Gz} \qquad (A.1)$$

where $\mathbf{z} = \mathbf{x} + \mathbf{N}$ and $\mathbf{N}$ is the noise vector. The use of orthogonal transforms yield a $\mathbf{G}$ that contains a large number of elements that can be set to zero as they are relatively small in magnitude.

The Karhunen-Loeve transform (KLT) is optimal in respect to variance distribution [60] and estimation using the mean-square error [61]. There is no general algorithm that enables the fast computation of the KLT [60]. The KLT is a performance basis to which many orthogonal transforms are compared, including the Walsh-Hadamard transform (WHT), discrete Fourier transform (DFT), and the Haar transform (HT). The discrete cosine transform (DCT) is an orthogonal transform that closely compares to the KLT [62].

The DCT of a data sequence x_m, $m = 0, 1, \cdots, (M-1)$ is defined as

$$\begin{aligned} G_x(0) &= \frac{\sqrt{2}}{M} \sum_{m=0}^{M-1} x_m \\ G_x(k) &= \frac{2}{M} \sum_{m=0}^{M-1} x_m cos \frac{(2m+1)k\pi}{2M}, k = 1, 2, \cdots, (M-1) \end{aligned} \qquad (A.2)$$

where $G_x k$ is the kth DCT coefficient.

The inverse discrete cosine transform (IDCT) is defined as

$$x_m = \frac{1}{\sqrt{2}} G_x(0) + \sum_{k=1}^{M-1} G_x(k) cos \frac{(2m+1)k\pi}{2M}, m = 0, 1, \cdots, (M-1). \qquad (A.3)$$

APPENDIX B

COLUMN STACKED FIXED TRANSFORMS

As introduced in section 3.1, processing in the STAP model is carried out in the N dimensional signal space resulting from stacking the snapshot column-wise. When a fixed transform is used, a matrix form for the transform would be beneficial for processing the signal.

A one-dimensional discrete N point Fourier transform may be written as

$$F_1 = \begin{bmatrix} 1 & 1 & \cdots & 1 \\ 1 & e^{-j\frac{2\pi}{N}} & \cdots & e^{-j\frac{2\pi(N-1)}{N}} \\ 1 & e^{-j\frac{2\pi 2}{N}} & \cdots & e^{-j\frac{2\pi 2(N-1)}{N}} \\ \vdots & \vdots & \vdots & \vdots \\ 1 & e^{-j\frac{2\pi(N-1)}{N}} & \cdots & e^{-j\frac{2\pi(N-1)^2}{N}} \end{bmatrix} \qquad (B.1)$$

A two-dimensional DFT that results from stacking the transform as done when creating the vector for STAP processing, is created using the form,

$$X(k_1,k_2) = \sum_{n=0}^{N-1}\sum_{m=0}^{M-1} x(n,m)e^{-j(\frac{2\pi}{N})k_1 n}e^{-j(\frac{2\pi}{M})k_2 m}. \qquad (B.2)$$

This may be represented in matrix form as

$$F_2 = \left.\overbrace{\begin{bmatrix} F_1 & F_1 & \cdots & F_1 \\ F_1 & e^{-j\frac{2\pi}{M}}F_1 & \cdots & e^{-j\frac{2\pi(M-1)}{M}}F_1 \\ \vdots & \vdots & \vdots & \vdots \\ F_1 & e^{-j\frac{2\pi(M-1)}{M}}F_1 & \cdots & e^{-j\frac{2\pi(M-1)^2}{M}}F_1 \end{bmatrix}}^{NM}\right\} NM \qquad (B.3)$$

This matrix is formed using the following relationships:

$$F_2 = \begin{array}{cc|c|c|c|c|}
 & & m=0 & m=1 & \cdots & m=M-1 \\
 & & n=0,1,\cdots N-1 & n=0,1,\cdots N-1 & & n=0,1,\cdots N-1 \\
\hline
 & k_1=0 & & & & \\
k_2=0 & \vdots & & & & \\
 & k_1=N-1 & & & & \\
\hline
 & k_1=0 & & & & \\
k_2=1 & \vdots & & & & \\
 & k_1=N-1 & & & & \\
\hline
\vdots & & & & & \\
\hline
 & k_1=0 & & & & \\
k_2=M-1 & \vdots & & & & \\
 & k_1=N-1 & & & & \\
\hline
\end{array} \qquad (B.4)$$

In the case of the discrete cosine transform, the base equation is

$$U(m) = k_m \sum_{n=0}^{N-1} u(n) cos \frac{(2n+1)m\pi}{2N}, \qquad (B.5)$$

where $k_m = \frac{1}{\sqrt{2}}$ if $m = 0$ else $k_m = 1$ and the tranform matrix is formed as was done in the case of the DFT.

APPENDIX C

ρ COMPARISON

In this appendix are considered Equation 4.26 and 4.27 derived respectively in [56] and [57]. While there are no similarities in the derivations, it will be shown here that Equation 4.26 can be obtained as an approximation of Equation 4.27. To that end first apply the approximation [63, p.33 (11)]

$$\frac{\Gamma(K+1)}{\Gamma(K+1-p)} \cong K^p. \tag{C.1}$$

The CSNR values considered are smaller than, but close to, 1. Let $\rho = 1 - h$. Then, for $h \to 0$ and $K \to \infty$:

$$\rho^{K-p} = 1 - (K-p)\,h + o\left(h^2\right) \cong 1 - Kh, \tag{C.2}$$

as well as

$$e^{-K(1-\rho)} = 1 - Kh + o\left(h^2\right). \tag{C.3}$$

Applying Equations C.1 and C.2 in Equation 4.27, and Equation C.3 in Equation 4.26, we get the two expressions to be equal.

REFERENCES

1. Leon Cohen. Time-frequency distributions- a review. *Proceedings of the IEEE*, 77(7):941–981, July 1989.

2. Theo A. C. M. Classen and Wolfgang F. G. Mecklenbrauker. The wigner distribution - a tool for time-frequency signal analysis Part I: Continuous-time signals. *Philips Journal of Research*, 35(3):217–251, 1980.

3. Boualem Boashash, Peter O'Shea, and Morgan J. Arnold. Algorithms for instantaneous frequency estimation: A comparative study. In Franklin T. Luk, editor, *Advanced Signal-Processing Algorithms, Architectures, and Implementations (1990) Vol 1348*, pages 126–148. SPIE - The International Society for Optical Engineering, July 1990.

4. Langford B. White. Estimation of the instantaneous frequency of a noisy signal. In Boualem Boashash, editor, *Time-Frequency Signal Analysis*, chapter 10, pages 233–249. Longman Cheshire, Melbourne, 1992.

5. Brian C. Lovell and Robert C. Williamson. The statistical performance of some instantaneous frequency estimators. *IEEE Transactions on Signal Processing*, 40(7):1708–1723, July 1992.

6. Boualem Boashash. Estimating and interpreting the instantaneous frequency of a signal-part 1: Fundamentals. *Proceedings of the IEEE*, 80(4):520–538, April 1992.

7. Fred J. Harris and Hana Abu Salem. Performance comparison of Wigner-Ville based techniques to standard fm-discriminators for estimating instantaneous frequency of a rapidly slewing fm sinusoid in the presence of noise. In *SPIE Vol 975 Advanced Algorithms and Architectures for Signal Processing III (1988)*, pages 232–244. SPIE– the International Society for Optical Engineering, August 1988.

8. Sergio Barbarossa and Alfonso Farina. A novel procedure for detecting and focusing moving objects with SAR based on the Wigner-Ville distribution. In *IEEE International Radar Conference*, pages 44–50. IEEE, 1990.

9. Pierfrancesco Lombardo. Estimation of target motion parameters from dual-channel sar echos via time-frequency analysis. In *Proceedings of the 1997 IEEE National Radar Conference*, pages 13–18. NATRAD-97, IEEE, 1997.

10. Zhao Zhiqin, Zheng Weiqiang, Dai Shengli, and Huang Shunji. A new approach of wigner-ville distribution in moving targets parameters estimation of sar. In *CIE International Conference of Radar*, pages 470–474. CICR-96, IEEE, 1996.

11. Louis Auslander, C. Buffalano, R. Orr, and R. Tolimieri. A comparison of the Gabor and short-time Fourier transforms for signal detection and feature extraction in noisy environments. In Franklin T. Luk, editor, *Advanced Signal-Processing Algorithms, Architectures, and Implementations (1990) Vol 1348*, pages 230–247. SPIE - The International Society for Optical Engineering, July 1990.

12. Ingrid Daubechies. The wavelet transform, time-frequency localization and signal analysis. *IEEE Transactions on Information Theory*, IT-36(5):961–1005, September 1990.

13. J. Morlet, G Arens, E. Fourgeau, and D. Giard. Wave propagation and sampling theory. *Geophysics*, 47(2):203–236, 1982.

14. Joseph G. Teti Jr. and H. N. Kritikos. Sar ocean image representation using wavelets. *IEEE Transactions on Geoscience and Remote Sensing*, 30(5):1089–1094, September 1992.

15. I. S. Reed, J. D. Mallett, and L. E. Brennan. Rapid convergence rate in adaptive arrays. *IEEE Transactions on Aerospace and Electronic Systems*, 10(6):853–863, November 1974.

16. I. P. Kirsteins and D. W. Tufts. Adaptive detection using low rank approximation to a data matrix. *IEEE Transactions on Aerospace and Electronic Systems*, 30:55–67, January 1994.

17. A. M. Haimovich. The eigencanceler: adaptive radar by eigenanalysis methods. *IEEE Transactions on Aerospace and Electronic Systems*, pages 532–542, April 1996.

18. Lena Chang and Chien-Chung Yeh. Performance of DMI and eigenspace-based beamformers. *IEEE Transactions on Antennas and Propagation*, 40(11):1336–1347, November 1992.

19. Y. I. Abramovich. Controlled method for adaptive optimization of filters using the criterion of maximum signal to noise ratio. *Journal of Communications Technology and Electronics*, 26:87–95, 1981. translated from Russian.

20. O. P. Cheremisin. Efficiency of an adaptive algorithm with regularization of the sampled correlation matrix. *Journal of Communications Technology and Electronics*, 27:69–77, 1982. translated from Russian.

21. J. Scott Goldstein and Irving S. Reed. Reduced-rank adaptive filtering. *IEEE Transactions on Signal Processing*, 45(2):492–496, February 1997.

22. J. Scott Goldstein and Irving S. Reed. Subspace selection for partially adaptive sensor array processing. *IEEE Transactions on Aerospace and Electronic Systems*, 33(2):539–543, April 1997.

23. Franz Hlawatsch and G. Faye Boudreaux-Bartels. Linear and quadratic time-frequency signal representations. *IEEE Signal Processing*, pages 21–67, April 1992.

24. Boualem Boashash. *Time-Frequency Signal Analysis*, volume 1 - Signal Processing of *Advances in Spectrum Analysis and Array Processing*, chapter 9, pages 418–517. Prentice-Hall, Englewood Cliffs, NJ, 1991.

25. W.M. Brown and L.J. Procello. An introduction to synthetic aperture theory. *IEEE Spectrum*, pages 52–62, September 1969.

26. Jr. J.C Kirk. A discussion of digital processing in synthetic aperture radar. *IEEE Transactions on Aerospace and Electronic Systems*, 11(3), 1975.

27. Jr. David C. Munson and Robert L. Visentin. A signal processing view of strip-mapping synthetic aperture radar. *IEEE Transactions on Acoustics, Speech, and Signal Processing*, 37(12):2131–2147, 1989.

28. Donald R. Wehner. *High Resolution Radar*, chapter 6, pages 185–271. Artech House, 685 Canton Street Norwood, MA 02062, 1987. ISBN: 0-89006-194-7.

29. B. Boashash and G. Jones. Instantaneous frequency and time-frequeny distributions. In B. Boashash, editor, *Time-Frequency Signal Analysis*, pages 43–73. Longman Cheshire, Melbourne, 1992.

30. S. Hamid Nawab and Thomas F. Quatieri. *Advanced topics in Signal Processing*, chapter Short-Time Fourier Transform, pages 289–337. Prentice Hall signal processing series. Prentice Hall, Englewood Cliffs, NJ, 1988.

31. Jont B. Allen and Lawrence R. Rabiner. A unified approach to short-time Fourier analysis and synthesis. *Proceedings of the IEEE*, 65(11):1558–1564, November 1977.

32. R.A. Altes. Detection, estimation, and classification with spectograms. *Journal of the Acoustical Society of America*, 67(4):1232–1246, 1980.

33. D. Gabor. Theory of communications. *Journal of the IEE*, 93(III):429–457, November 1946.

34. Boualem Boashash. *Time-Frequency Signal Analysis.* Longman Cheshire, Melbourne, 1992.

35. Martin J. Bastiaans. Gabor's expansion of a signal into Gaussian elementary signals. *Proceedings of the IEEE*, 68(4):538–539, April 1980.

36. Martin J. Bastiaans. A sampling theorem for the complex spectrogram, and Gabor's expansion of a signal in Gaussian elementary signals. *Optical Engineering*, 20(4):594–598, July/August 1981.

37. A Grossmann and J. Morlet. Decomposition of hardy functions into square integrable wavelets of constant shape. *SAIM J. Math. Anal.*, 15:723–736, July 1984.

38. P.J. Burt and E.H. Adelson. The laplacian pyramid as a compact image code. *IEEE Transactions on Communications*, 31(4):532–540, April 1983.

39. R.E. Crochiere, S.A. Weber, and J.L. Flanagan. Digital coding of speech in subbands. *Bell System Technical Journal*, 55:1069–1085, October 1976.

40. A. J. E. M. Janssen. Weighted wigner distributions vanishing on lattices. *J. Math. Anal. Appl.*, 80:156–167, 1981.

41. L. Cohen. Generalized phase-space distribution functions. *Journal of Math. Phys.*, 7(5):781–786, 1966.

42. Olivier Rioul and Patrick Flandrin. Time-scale enegery distributions: A general class extending wavelet transforms. *IEEE Transactions on Signal Processing*, 40(7):1746–1757, July 1992.

43. Theo A. C. M. Classen and Wolfgang F. G. Mecklenbrauker. The wigner distribution - a tool for time-frequency signal analysis Part III: Relations with other time-frequency signal transformations. *Philips Journal of Research*, 35(6):372–389, 1980.

44. Shubha Kadambe and G. Faye Boudreaux-Bartels. A comparison of the existence of "cross terms" in the Wigner distribution and the squared magnitude of the Wavelet transform and the short time Fourier transform. *IEEE Transactions on Signal Processing*, 40(10):2498–2517, October 1992.

45. David C. Rife and Robert R. Boorstyn. Single-tone parameter estimation from discrete-time observations. *IEEE Transactions on Information Theory*, IT-20(5):591–598, September 1974.

46. L. E. Brennan and I.S. Reed. Theory of adaptive radar. *IEEE Transactions on Aerospace and Electronic Systems*, 10(2):237–252, March 1973.

47. L. E. Brennan, J.D. Mallett, and I.S. Reed. Adaptive arrays in airborne MTI radar. *IEEE Transactions on Antennas and Propagation*, 24:607–615, September 1976.

48. Lloyd J. Griffiths and Charles W. Jim. An alternative approach to linearly constrained adaptive beamforming. *IEEE Transactions on Antennas and Propagation*, 30(1):27–34, January 1982.

49. Neil K. Jablon. Steady state analysis of the generalized sidelobe canceller by adaptive noise cancelling techniques. *IEEE Transactions on Antennas and Propagation*, 34(3):330–337, March 1986.

50. Daniel F. Marshall. A two step adaptive interference nulling algorithm for use with airborne sensor arrays. In *Proceedings of the Seventh Signal Processing Workshop on Statistical and Array Processing*, pages 301–304, Quebec City, Canada, April 1994.

51. Murat O. Berin. Analysis on calibration, robustness, detection of space-time adaptive radar using experimental data. Master's thesis, New Jersey Institute of Technology, Department of Electrical and Computer Engineering, Newark, NJ, January 1996.

52. Murat O. Berin and A. M. Haimovich. Signal cancellation effects in adaptive radar mountaintop data-set. In *IEEE International Conference on Acoustics, Speech, and Signal Processing 1996*, pages 2614–2617. ACASSP-96, IEEE, 1996.

53. B. D. VanVeen and R. A. Roberts. Partially adaptive beamformer design via output power minimization. *IEEE Transactions on Acoustics, Speech and Signal Processing*, 35:1524–1532, November 1987.

54. Y.I. Abramovich. Analysis of direct adaptive tuning method for interference compensation systems with auxiliary linear constraints. *Journal of Communications Technology and Electronics*, 35:30–39, 1990. translated from Russian.

55. J. Scott Goldstein and Irving S. Reed. Theory of partially adaptive radar. *IEEE Transactions on Aerospace and Electronic Systems*, in press.

56. A. M. Haimovich. Asymptotic distribution of the conditional signal-to-noise ratio in an eigenanalysis-based adaptive array. *IEEE Transactions on Aerospace and Electronic Systems*, 33(3):988–997, July 1997.

57. I. P. Kirsteins and D. W. Tufts. Rapidly adaptive nulling of interference. In M. Bouvet and G. Bienvenu, editors, *High Resolution Methods in Underwater Acoustics*, chapter 6, pages 220–249. Springer-Verlag, New York, 1991.

58. G. W. Titi. An overview of the arpa mountaintop program. In *1994 Adaptive Antenna Systems Symposium*, pages 53–59, Melville, NY, November 1994.

59. A.M. Haimovich and M. Berin. Eigenanalysis-based space-time adaptive radar: Performance analysis. *IEEE Transactions on Aerospace and Electronic Systems*, 33:1170–1179, October 1997.

60. H.C. Andrews. Multidimensional rotations in feature selection. *IEEE Transactions on Computers*, 20:1045–1051, September 1971.

61. W.K. Pratt. Generalized wiener filtering computation techniques. *IEEE Transactions on Computers*, 21:636–641, July 1972.

62. N. Ahmed, T. Natarajan, and K.R. Rao. Discrete cosine transform. *IEEE Transactions on Computers*, 23:90–93, January 1974.

63. Y. Luke. *The Special Functions and Their Approximations*, volume 1. Academic Press, New York, 1969.

INDEX